STOCHASTIC MODELING OF NONISOTHERMAL ANTISOLVENT CRYSTALLIZATION PROCESSES

UNIVERSITÀ DEGLI STUDI DI CAGLIARI

GIUSEPPE COGONI

UNIVERSITÀ DEGLI STUDI DI CAGLIARI
DOTTORATO DI RICERCA IN INGEGNERIA INDUSTRIALE
XXV CICLO

STOCHASTIC MODELING OF NONISOTHERMAL ANTISOLVENT CRYSTALLIZATION PROCESSES

UNIVERSITÀ DEGLI STUDI DI CAGLIARI

GIUSEPPE COGONI

SUPERVISORS:
PROF. ROBERTO BARATTI
PROF. JOSÉ A. ROMAGNOLI

UNIVERSITÁ DEGLI STUDI DI CAGLIARI
DOTTORATO DI RICERCA IN INGEGNERIA INDUSTRIALE
XXV CICLO

Contents

Abstract

In this Thesis a stochastic approach to model antisolvent crystallization processes is addressed. The motivations to choice a stochastic approach instead of a population balance modeling has been developed to find a simple and an alternative way to describe the evolution of the Crystal Size Distribution (CSD), without consider complex thermodynamic and kinetic aspects of the process. An important parameter to consider in crystallization process is the shape of the CSD (in terms of variance) and the mean size of crystals in order to optimize the filtering of the final product and then increase the production. The crystallization processes considered in this Thesis are the antisolvent crystallization processes used in particular when the solute is weakly temperature-sensitive and then a second solvent, properly called antisolvent, is added in the solution favoring the crystallization of the solute. In antisolvent crystallization processes it is important the consumption of the second solvent added, in particular, optimizing the feed-rate and coupling the process in synergy with cooling crystallization in order to improve the production and the quality of the desired product.

The stochastic approach used in this Thesis is based on the Fokker Plank Equation (FPE), which has allowed finding an analytical solution of the model, with some assumptions, and obtaining an analytical model able to describe the evolution of the mean size of crystals and the variance of the CSD. This analytical solution has leaded to develop an analytical relationship between the evolution in time of the first two stochastic moments of the FPE, such as mean and variance, and the manipulated variables, such as antisolvent feed-rate and temperature, obtaining as a result a map showing the asymptotic moments obtainable within a certain range of operating conditions.

This Thesis also analyzes the physical-chemical aspects of the antisolvent crystallization processes, including the temperature effects, finding a strong influence onto the nucleation and growth

rate of crystals due by the hydrogen bond strength between solvent-antisolvent molecules despite of the molecular interaction in a solvated system.

The physical-chemical consideration concerning the antisolvent crystallization processes allowed to better understand the influence of the second solvent added, consequently optimizing the choice for the proper antisolvent to use with a proper feed-rate and temperature profile, minimizing the energy consumptions, in order to obtain the desired product.

The stochastic model and the physical-chemical considerations have been validated with experimental data performed in a laboratory scale crystallizer. The experimental samples have been analyzed using an optical microscope and then the images taken have been manually processed in order to obtain the experimental CSDs.

Chapter 1

Introduction

This introductory Chapter starts with the illustration of the motivations which lead us to the development of this Thesis. After that, a summary of the Thesis is given, by showing how it is structured in different Chapters. Finally, a list of publications in journals and conference in papers and other activities derived from the present work is presented.

1.1 Motivations

Crystallization is a widely used technology for solid-liquid separation in the process industry. It is extensively used in the production of pharmaceuticals, fertilizers and many more chemical and petrochemical fine products to separate the drug from the solvent mixture as well as to ensure that the drug crystal product conforms to size and morphology specifications. This process represents a multi-million dollar industry where any method to improve the production of these products would be highly valued. The crystal size distribution in crystallization processes is one of the most important variables since it influences factors such as filtration rate, de-watering rate, dissolution rate and bioavailability, among others. Thus, the main objective of this process is to target model-

based optimal strategies for the crystallization operations. The driving force in crystal formation is supersaturation.

The trend of supersaturation generation during the process has a direct and substantial role on crystal characteristics such as size, morphology and purity. There is a number of ways to control supersaturation and these include temperature and evaporation. In the last decade the salting-out method has drawn more attention. In this method, which is also known as solventing-out, drowning-out or quenching, a substance known as antisolvent or precipitant is added to the solution with the goal to reduce the solubility of the solute in the original solvent and consequently generating supersaturation. The antisolvent crystallization is also combined with the cooling crystallization in order to obtain an optimal supersaturation trajectory and to optimize the cost of production and the energy consumption.

The development of effective mathematical models describing the crystal growth dynamics is a crucial issue towards finding the optimal process performance and to control the crystal size and distribution. The main approach, so far exploited, is by developing population balance models [Ramkrishna, 2000] taking into account the evolution of crystal particles across temporal and size domains. This method implies first principle assumptions requiring a detailed knowledge of the physics and thermodynamics associated with the solute and solvent properties to be adequately incorporated in the population balances, which sometimes come from empirical formulations such as the solute solubility. In addition, population balances modeling results in large and complex dynamic models, which cannot be easily employed, for instance, in model-based process control design or in real-time implementation.

Recently, direct design, model-free approaches were proposed as an alternative efficient way of controlling crystallization processes for anti-solvent, cooling and combined processes [Woo et al, 2009; Abu Bakar et al, 2009] including the case of polymorphic control [Kee et al, 2009]. Along this way, a new approach to model crystallization systems characterized by Crystal Size Distribution (CSD) is the Fokker-Planck Equation is developed (FPE) [Galan et al, 2010;

Grosso et al, 2010; Grosso et al, 2011; Cogoni et al, 2011]. In this approach, the time evolution of each element of the population, the crystal, is regarded as a possible outcome of a random variable driven by a deterministic term. Indeed, each crystal does not grow in the same manner and some dispersion, in size, of the population is always observed. This random variable will be thus characterized uniquely by its Probability Density Function (PDF) whose evolution in time can be described in terms of a the FPE. Within this context, the FPE could be considered as an alternative way to develop a population balance, taking into account the natural fluctuations present in the crystallization process, and allowing describing, in a compact form, the Crystal Size Distribution (CSD) in time. The deterministic contribution driving the crystal growth is modeled by a proper model, allowing to describe the mean size behavior in time. However, in the FPE formulation, the model behavior is affected by both the deterministic and stochastic contribution. Indeed, the specific form of the stochastic model may lead to different shapes for the predicted probability density function, even being equal the nature of the deterministic part.
In this Thesis, the attention is focused on the proper modeling of the stochastic term, and, to this end, the performance of the FPE based on different expressions for such stochastic model has been formulated and assessed comparatively including also a direct comparison with the population balance approach. Later, the modeling approach is focused on simplified model able to describe the process considered, without losing information about the CSD description, but allowing a linear FPE formulation with linear coefficients, where an analytical solution is then obtained. From a control, optimization and monitoring point of view the availability of the analytical solution of the model describing the time evolution of the CSD may be valuable for the design of proper off-line and/or on-line model based control strategies.

In order to use the model over the whole operational range proper relationships between the parameters of the model and the two process variables, namely antisolvent feedrate and temperature, has to be developed. This is also extremely important when using the model in a model-based control configuration. Consequently, as an

additional novelty, the obtained global models are used to define an operating map of the crystallization process, where asymptotic iso-mean and iso-variance curves are reported in an antisolvent feedrate – temperature plane.

The effect of temperature in antisolvent crystallization operation, even for system where the solubility is weakly dependent on temperature, was shown numerically and experimentally, still there is no clear explanation of these effects. One reason about this enhancement, caused by the temperature and also by the amount of antisolvent used, can be explained by the interaction between solvent and the antisolvent. The antisolvent interacts strongly with the solvent, mostly because of hydrogen bonding, that is because the intrinsic polarity nature of the solvents used, and increasing its strength the system is forced to crystallize [Oostorhof et al, 2001; Mirmeharabi et al, 2005; Czeslik & Jonas, 1999]. The number of hydrogen bonds is also proportional to the antisolvent feedrate and, its strength is dependent of the temperature.
In order to investigate the interaction solvent-antisolvent, solvents-solute, and thus the influence of hydrogen bonding on the supersaturation of the solution, in this thesis have been considered different antisolvents, all of them in aqueous solution with a volume concentration of 95%, and using different operating conditions.

1.2 Summary

This Thesis is structured in six main chapters subdivided in paragraphs for each topic, in order to allow the reader to better follow the development of the model, from the physical description of the process and the mathematical formulation of the model to the comments and conclusions of the results obtained, including a detailed description of the experimental procedure and devices used.

A summary of this Thesis is shown in the following list, where a brief description of each chapter is given.

Chapter 2. A general overview of the crystallization processes with the physical aspects is explained. This chapter introduces the reader from the basics of crystallization and all its methods until the particular crystallization process used to develop the research for this Thesis. *The main contribution in this chapter is the hypothesis and the formulation about the influence of the hydrogen bonding on the supersaturation of the system, influencing the crystal growth and the nucleation rates. This hypothesis has been verified using different antisolvents with different polarity index and considering the effects of temperature and antisolvent feedrate*.

Chapter 3. *This chapter is focused on the stochastic model development, in which the main contribution is the formulation of the Fokker-Planck Equation, FPE, obtaining as a linear PDE with non-linear coefficients, suitable for a qualitative design of the Crystal Size Distribution, CSD. The FPE is also compared with the more common Population Balances, PBM, in which the process is based on thermodynamic a kinetic consideration, hence from a solid knowledge of the physics, resulting as a more complex equation. This Chapter concludes with the formulation of a linear FPE model with linear coefficients where an analytical solution is obtained after some mathematical assumptions, allowing a better suitability for optimizations and control purposes.*

Chapter 4. Here, all the procedure to obtain the experimental data used to study and validate all the models is explained as well as all the devices used and developed. This chapter also summarizes all the experimental runs performed for all the models developed.

Chapter 5. This Chapter shows all the experimental results and further developments of the process modeling obtained a posteriori. *The main contributions start from the rigorous model development, passing to a simplified model, where an analytical solution has been founded, the operating map, describing the asymptotic behavior of mean size and variance as a function of temperature and antisolvent feedrate, and finally concluding with an investigation about the influence of the antisolvent-solvent interaction, considering their polarity nature and the hydrogen bond behavior.*

Chapter 6. Conclusions and recommendations for future research are given.

1.3 Publications in Journal and Conference Papers

Some of the topics present in this Thesis have been published in international journal paper, and national and international congress/conferences.

International Journal Papers:

Grosso M.; Cogoni G.; Baratti R.; Romagnoli J. A. *Stochastic Approach for the Prediction of PSD in Crystallization Processes: Formulation and Comparative Assessment of Different Stochastic Models,* Ind. & Eng. Chem. Res., 2011, 50, 2133-2143.

Cogoni G.; Grosso M.; Baratti R.; Romagnoli J. A. *Time evolution of the PSD in crystallization operations: An analytical solution based on Ornstein-Uhlenbeck process,* AIChE Journal, 2012, doi:10.1002/aic.13760.

Not yet published International Journal Papers:

Cogoni G.; Tronci S.; Mistretta G.; Baratti R.; Romagnoli J. A.; *Stochastic Approach for the Prediction of PSD in Nonisothermal Antisolvent Crystallization Processes,* AIChE Journal. [Already Submitted]

Cogoni G.; Baratti R.; Romagnoli J. A.; *On the influence of hydrogen bond interactions in isothermal and non-isothermal antisolvent crystallization processes,* Ind. & Eng. Chem. Res. [Already Submitted]

Cogoni G.; Widenski D.; Grosso M.; Baratti R.; Romagnoli J. A.; *Comparison between population balances and stochastic models for crystallization processes,* Comp. & Chem. Eng. [To be Submitted]

National and International Congresses and Conferences:

Cogoni G.; Grosso M.; Baratti R.; Romagnoli J. A. *Dynamic evolution of PSD modelled using an Ornstein-Uhlenbeck process approach*, 18th World Congress IFAC 2011, Milan - Italy.

Baratti R.; Cogoni G.; Grosso M.; Mistretta G.; Romagnoli J. A.; Tronci S. *Modellazione Stocastica di Cristallizzatori*, GRICU 2012, Montesilvano - Italy.

Chapter 2

Crystallization

This Chapter introduces the main concepts concerning the crystallization processes from a physical point of view and the different techniques used in industry in order to obtain the separation of the solute from the liquid solution. This Chapter ends with a hypothesized mechanism concerning the precipitation of the solute, caused by the influence of the hydrogen bond interactions. This last part of this Chapter has been developed in detail in Chapter 4 and 5 with some ad hoc experiments, and with proper validation runs, in order to verify and confirm the hydrogen bond influence on the behavior of the process.

2.1 Phase Equilibrium

Solubility

The solubility of a substance in a solvent is the maximum concentration that can exist at equilibrium at a given set of conditions and often increases (which sometimes but rarely decreases) with the temperature of the solution. The equilibrium phase diagram of solubility or solubility-supersolubility plot [Miers and Isaac, 1907] shown in Figure 2.1, provides an useful starting point for considering why crystallization occurs and what type of process might be more suitable for production of a particular substance. It can be divided into three zones (Ostwald, 1897).

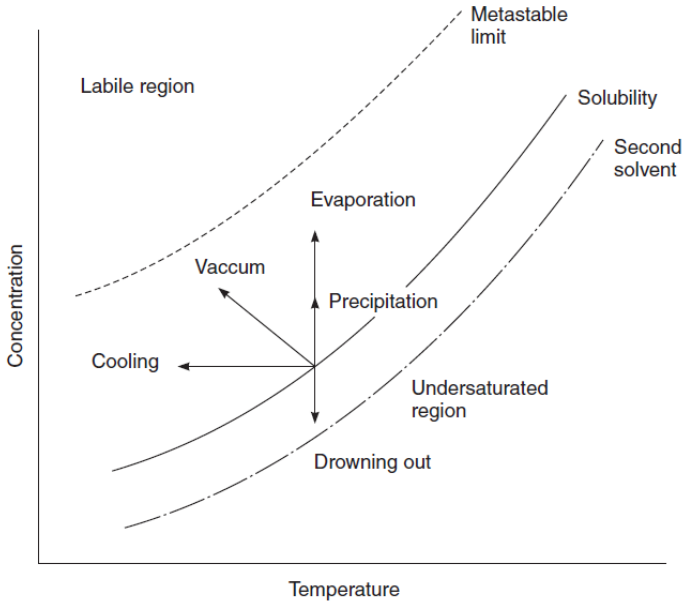

Figure 2.1: Solubility-Supersolubility curve.

1) *Undersaturated:* Crystals present will dissolve;
2) *Metastable:* A supersaturated region in which crystals will grow;
3) *Labile:* A region in which a solution will nucleate spontaneously.

The solubility thus denotes the extent to which different substances, in whatever state of aggregation, are miscible in each other. The constituent of the resulting solution present in large excess is known as the solvent, the other constituent being the solute.

For a substance to dissolve in a liquid, it must be capable of disrupting the solvent structure and permit the bonding of solvent molecules to the solute or its component ions. The forces binding the ions, atom or molecules in the lattice oppose the tendency of a crystalline solid to enter solution. The solubility of a solid is thus determined by the resultant of these opposing effects. The solubility of a solute in a given solvent is defined as the concentration of that

solute in its saturated solution. A saturated solution is one that is in equilibrium with excess solute present.

Supersaturation

The fundamental, thermodynamic, driving force for crystallization is given by the change in chemical potential between standing and equilibrium states. This applies whether the particles formed are organic or inorganic, biochemical or petrochemical. Chemical potential is a quantity that is not easy to measure, however, and the driving force is more conveniently expressed in terms of solution concentration by the following approximation:

$$\Delta\mu = \ln\left(\frac{C}{C^*}\right) \cong \frac{C}{C^*} - 1 = \frac{\Delta C}{C^*} = S - 1 = \sigma \tag{2.1}$$

where $\Delta\mu$ is the change in chemical potential, C is the standing concentration and C^* the equilibrium saturation concentration, S is the supersaturation ratio and σ is the relative or absolute supersaturation. It is worth noting that, although commonly used, strictly equation 2.1 is valid only for $C \approx C^*$, but many precipitations employ $C >> C^*$. Supersaturation can be thought of as the concentration of solute in excess of solubility. For practical use, however, supersaturation is generally expressed in terms of concentration:

$$\Delta C = C - C^* \tag{2.2}$$

where C is the concentration of solution, C^* is the saturation concentration and ΔC is sometimes called the “concentration driving force”.

2.2 Nucleation and Growth

Nucleation is the formation of a new solid phase. There are two types, primary and secondary as depicted in Figure 2.2. The two types will be described in turn.

Primary nucleation

Primary nucleation occurs exclusively due to supersaturation. The mechanism for primary nucleation is generally believed to be due to a series of bimolecular collisions:

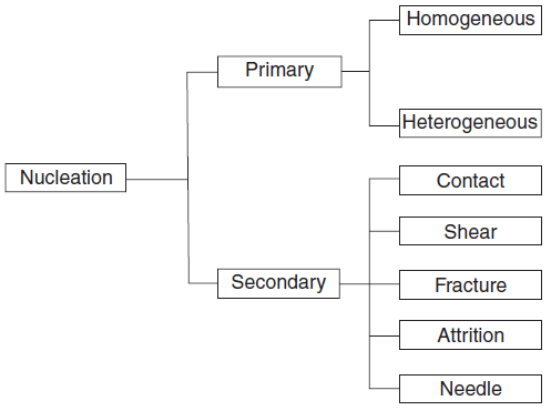

Figure 2.2: Classification of types of nucleation.

When the size of an aggregate becomes large enough, then thermodynamics predicts that it should become stable and grow. This size is called the critical nucleus size. This type of nucleation requires rather high supersaturations and is generally only applicable in precipitation processes.

The two different types of primary nucleation are homogeneous and heterogeneous. In homogeneous nucleation no foreign substances, such as dust, are present in solution. In heterogeneous primary nucleation some foreign substance is present which provides a nucleation site. Generally homogeneous nucleation conditions are difficult to achieve and maintain.

Secondary nucleation

Secondary nucleation requires the presence of growing crystals in solution. It differs greatly from primary nucleation in that it occurs at much lower supersaturations. In general most industrial crystallization processes operate under conditions which favor secondary over primary nucleation. The most important types of secondary nucleation are:

1) *Contact*

   It happens when some disturbance occurs at the surface of a growing crystal resulting from contact with the crystallizer, impeller, or another crystal.

2) *Shear*

   It occurs when liquid travels across a crystal at a high speed, sweeping away nuclei that would otherwise be incorporated into a crystal, causing the swept-away nuclei to become new crystals.

3) *Fracture*

   It is due to particle impact.

4) *Attrition*

   It is due by the synergy of particle impact and fluid flow.

5) *Needle*

   It happens when dendrites are formed on the surface of a crystal, growing at high supersaturation, and these dendrites are removed forming nuclei.

Over the various mechanisms which are involved in secondary nucleation, the most important, from an industrial point of view, is contact nucleation. [Jones, 2002].

Growth

During the crystallization the solute molecules or ions reach the surface of the growing crystals by diffusion through the liquid phase. After they reach the interface they must reorganize they structure into a lattice space in order to be adsorbed. Both processes diffusion and interfacial step, can only happen if the solution is supersaturated. Crystal growth is the increase in size of crystals as solute is deposited from solution. These often competing mechanisms ultimately determine the final crystal size distribution. The relationship between supersaturation and nucleation and growth is defined by the following (somewhat simplified) equations [Mullin, 2001]:

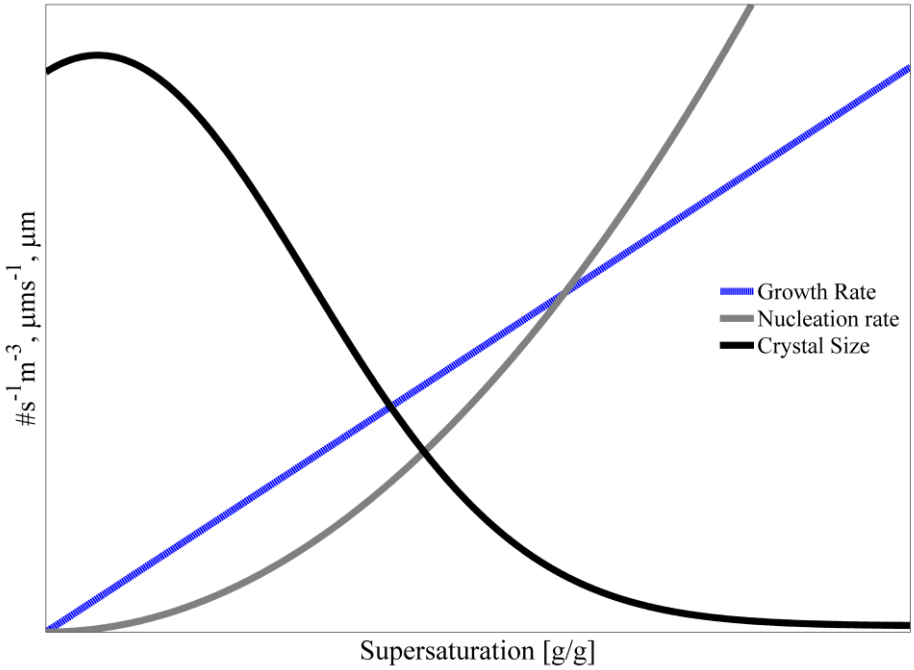

Figure 2.3: Solvation of sodium chloride (NaCl) in water (H_2O), in which the separation of electrostatic charges has been highlighted.

$$G = k_g \Delta C^g \tag{2.3}$$

$$B = k_b \Delta C^b \tag{2.4}$$

where G is the growth rate, k_g is the growth constant, g is the growth order, B the nucleation rate, k_b is the nucleation constant, b is the nucleation order and finally ΔC is the supersaturation expressed in terms of concentration (2.2).

For organic crystallization systems, the value of the growth order is typically between 1 and 2 and the value of the nucleation order is typically between 5 and 10 [Mullin, 2001]. When we plot what this looks like in theory it becomes clear why controlling supersaturation is so important. At low supersaturation, crystals can grow faster than they nucleate resulting in a larger crystal size distribution. However, at higher supersaturation, crystal nucleation dominates crystal growth, ultimately resulting in smaller crystals. This diagram, relating supersaturation to nucleation, growth and crystal size clearly illustrates how controlling supersaturation is vitally important when it comes to creating crystals of the desired size and specification.

2.3 Crystallization Techniques

There are several different crystallization techniques currently used to generate supersaturation necessary for crystallization. The most common techniques are cooling, evaporation, and antisolvent addition. All of these techniques cause crystallization due to changes in equilibrium solubility. The appropriate technique to use depends on the solubility behavior of the compound to be crystallized.

Cooling Crystallization. The cooling crystallization can be applied when the solubility gradient of the solution increases steeply decreasing the temperature or when a vaporization of the solvent has to be avoided. The operating temperature is usually obtained by applying a vacuum to the hot concentrated feed solution, or by indirect heat exchange with a cold source (water or thermal fluid).

Evaporative Crystallization. This process is suitable for products having a solubility which does not vary appreciably with temperature. Another application concerns the recovery, or elimination, of products from liquid effluents, often very dilute. In most cases, the actual crystallization unit is combined with a pre-concentration stage.

Antisolvent Crystallization. In the last decade the salting-out method has drawn more attention. In this method which is also known as solventing-out, drowning-out and quenching, a substance known as antisolvent or precipitant is added to the solution which reduces the solubility of the solute in the original solvent and consequently generating supersaturation. This technique is regarded as an energy-saving alternative to evaporative crystallization, provided that antisolvent can be separated at low (energy) costs. Also in cases where solute is highly soluble or its solubility does not change much with temperature, antisolvent crystallization is an advantageous method.

All of these techniques can be combined in order to obtain an optimal supersaturation trajectory and in order to optimize the costs of production and the energy consumptions.

2.4 Molecular Interactions

In crystallizing systems, especially where solubility is weakly dependent on temperature, the effect of temperature is not straightforward. Recently it was also shown [Widenski et al., 2012] that for these kind of systems temperature also influences the supersaturation, which is enhanced at low temperatures and becomes weaker as the temperature increases. The overall effect is that supersaturation is directly proportional to the antisolvent feedrate and concentration of the antisolvent and, inversely proportional to the temperature.

Although the effects of temperature on antisolvent crystallization operation were shown numerically and experimentally, even for a system where the solubility is weakly dependent on temperature, there is still no clear explanation of for these effects. One reason for this enhancement, caused by the temperature and also by the amount of antisolvent used, can be explained through the interactions between the solvent and the antisolvent. The antisolvent interacts strongly with the solvent, mostly through hydrogen bonding caused by the intrinsic polarity nature of the solvents used, increasing its strength so that the system is forced to crystallize [Oosterhof et al., 2001]. The number of hydrogen bonds is also proportional to the antisolvent feedrate where its strength is dependent on temperature.

In this section a hypothesis about the influence of solvation and hydrogen bond interactions on the supersaturation of the system will be explained. In order to formulate this hypothesis, a briefly introduction concerning the solvation, hydrogen bonding and supersaturation will be presented in the below paragraph.

Solvation, also called dissolution, is the process of attraction and association of solvent molecules with molecules or ions of a solute. As ions dissolve in a solvent, they spread out and become surrounded by solvent molecules, see Figure 2.4. This is a typical ion-dipole interaction, which involves charged ions and polar molecules, e.g., water. For a substance to dissolve in a liquid, it must be capable of disrupting the solvent structure and permit the bonding of solvent molecules to the solute or its component ions. The forces binding the ions, atoms or molecules in the lattice oppose the tendency of a crystalline solid to enter solution. The solubility of a solid is thus determined by the resultant of these opposing effects [Jones, 2002]. The magnitude of the interaction energy is between 40 and 600 KJ/mole and depends upon the ions charge, the dipole moment of the molecule and the square of the distance between the center of the ion and the midpoint of the dipole.

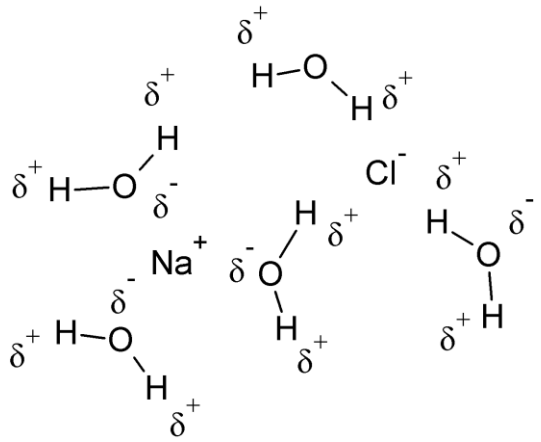

Figure 2.4: Solvation of sodium chloride (NaCl) in water (H_2O), in which the separation of electrostatic charges has been highlighted.

Hydrophilic solvents such as water, ethanol and other solvents with hydroxyl groups can establish hydrogen bonds within their molecules or other similar hydrophilic molecules. The hydrophilic nature of a solvent is proportional to the polarity index [Di Martino et al., 2007] and represents how much the separation of charges is strong in a molecular structure, leading to the hydroxyl groups interact with other similar molecules with hydrogen bonds, consequently as the polarity index is higher as the hydrogen bonds are stronger. Diminishing the hydrophilic nature of the solvent, the probability that these polar groups can establish hydrogen bonds with the solvent diminishes. The strength of the hydrogen bonds is also influenced by temperature, pressure and concentration, in particular, increases at low temperature, at high pressure and at high concentrations [Czeslik, et al 1999; Dougherty, 1998]. Hydrogen bonds are directional and relatively weak, with energy between 10 and 40 kJ/mol, but strong enough to define the structure and properties of water, proteins, and many other materials. The competition of these two interactions, ion-dipole and hydrogen bonds, affects the supersaturation of the antisolvent crystallization processes and consequently influences the shape of the Crystal Size Distribution (CSD), the growth and nucleation rate, and the morphology of crystals [Di Martino et al., 2007].

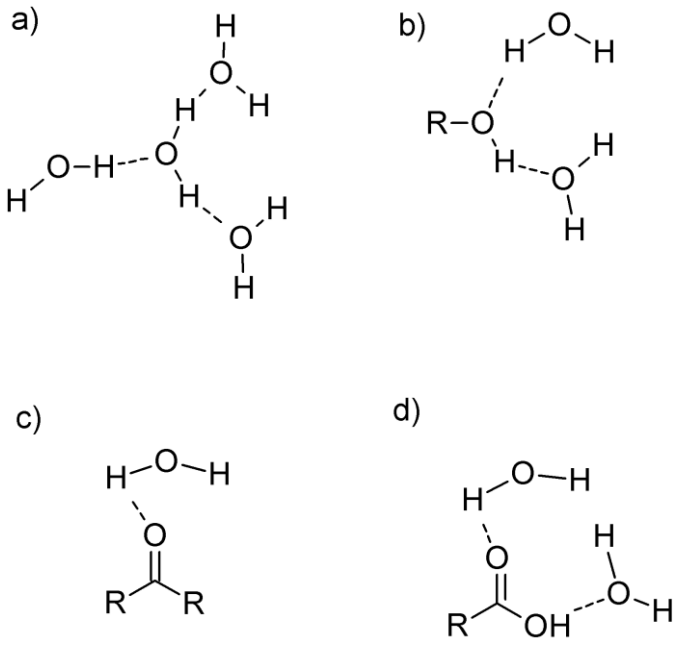

Figure 2.5: Hydrogen bonds between water (H_2O) and different organic polar molecules, respectively: a) within water; b) alcohols; c) aldehydes and d) carboxylic acids.

Supersaturation, as has been expressed on the previous paragraph, is represented as the rate between the concentration of the system and the equilibrium concentration of the solute in the liquid phase. The equilibrium concentration depends onto thermodynamic aspects, in which the most important is the activity coefficient that is influenced by the polarity nature of the compounds considered; consequently hydrogen bonds have an important role on the solubility of the system, therefore influence the supersaturation. The growth and nucleation rate are both directly proportional to the supersaturation, respectively when supersaturation rises up nucleation and growth rate rise up as well. For high values of supersaturation, nucleation dominates the growth rate, obtaining as a consequence crystals with a smaller mean size.

Considering the antisolvent crystallization processes, the influence of the antisolvent feedrate and temperature have been studied in previous works [Park & Yeo, 2012; Widenski et al., 2012, Grosso et

al., 2010; Grosso et al., 2011; Cogoni et al, 2012] showing that a high antisolvent feedrate increase the supersaturation of the system as well as decreasing the temperature, favoring the nucleation than the growth rate as a result and inducing a large number of nuclei in the initial stage of the nucleation process and consequently obtaining a narrower CSD. From a physical point of view, increasing the antisolvent feedrate and/or decreasing the temperature, we are statistically increasing the number of hydrogen bonds in the solution and the strength of them, favoring the nucleation of new crystals, also considering the dispersion of the CSD, we can obtain a narrower distribution as the temperature increase, because we have the dissolution phenomena of the smaller particles, leading the big ones to keep growing. In antisolvent crystallization, a similar effect could be obtained by changing the secondary solvent, in particular using one with a higher polarity index or changing the antisolvent concentration.

In this Thesis is hypothesized, applied on antisolvent crystallization processes, that higher hydrogen bond strength generates higher supersaturation caused by their statistical dominance on ion-dipole interactions, consequently influencing the nucleation and the growth rates.
Increasing the nucleation and growth rates induce a fast precipitation of the solute and consequently a faster growing, resulting as a wider CSD with a smaller mean size caused by the high nucleation of new crystals.
The effect of the temperature generates a high supersaturation as it decreases, caused by strengthen of the hydrogen bonds and therefore obtaining the same effects keeping a constant antisolvent concentration and feedrate. All of these effects can be gathered with the polarity nature of the solvents used. If this aspect is correct the polarity index of the solvent used increases the supersaturation increases as well, keeping constant the temperature, the concentration and the feedrate of the antisolvent.
The effects of supersaturation on the mean size of crystals, nucleation and growth rates are qualitatively summarized on Figure 2.3 [Celikbilek et al, 1999]. From Figure 2.3 one can observe that the behavior of the crystal size has a maximum and, after that, starts

to decrease as the supersaturation increases, this happens when the nucleation rate dominates the growth rate. It should be remarked that the functionality of nucleation and growth rates are always monotonic growing functions, but the behavior can be different than the one showed on Figure 2.3.
A qualitative summary of the hypothesized effects of hydrogen bonding is also shown in Table 2.1, considering the physical aspects discussed so far about the effects of temperature, antisolvent feedrate and polarity index, on the asymptotic behavior of the mean size of crystals, the dispersion of the CSDs and the growth velocity based on the physical considerations concerning the hydrogen bond strength.

Increasing	Asymptotic mean size	Dispersion	Growth velocity
Antisolvent feedrate	↓	↑	↑
Temperature	↑	↓	↓
Polarity Index	↓	↑	↑

Table 2.1: Qualitative effects of increasing the antisolvent feedrate, temperature and using and antisolvent polarity index on the asymptotic mean size, dispersion and growth velocity.

In order to verify and quantify these effects, a set of experimental runs selected ad hoc, have been conducted and discussed in Chapter 4 and 5, where the FPE equation has been used to fit the data. The experiments are performed considering different polarity indexes, with a constant temperature and antisolvent feedrate and concentrations.

Chapter 3

Model Development

The development of effective mathematical model describing the crystal growth dynamics is a crucial issue toward finding the optimal process performance and to control the crystal size and distribution. The main approach so far exploited is by developing population balance models [Ramkrishna, 2000] taking into account the evolution of crystal particles across temporal and size domains. This method implies first principle assumptions requiring a detailed knowledge of the physics and thermodynamics of the process. Some examples of antisolvent crystallization modeling are paracetamol [Zhou et al, 2006; Trifkovic et al, 2008] and sodium chloride [Nowee et al, 2008a; Nowee et al, 2008b]. Recently, cooling has been combined with anti-solvent crystallization and the joint process has been modeled for lovastatin [Nagy et al, 2008], and for acetylsalicylic acid [Lindenberg et al, 2009]. However, they demand a great deal of knowledge on the complex thermodynamic associated with the solute and solvent properties to be adequately incorporated in the population balances and sometimes these properties are correlated with empiric relationships. In addition, population balances modeling results in large and complex dynamic models, which cannot be easily employed, for instance, in model-based process control design or in real-time implementation [Nagy et al, 2009]. Recently, direct design, model-free approaches were proposed as an alternative efficient way of controlling crystallization processes for anti-solvent, cooling and combined processes [Woo et

al, 2009; Abu Bakar et al, 2009] including the case of polymorphic control [Kee et al, 2009].

Along this way, a new approach to model crystallization systems characterized by PSD is the Fokker-Planck Equation (FPE) [Galan et al, 2010; Grosso et al, 2010]. In this approach, the time evolution of each element of the population, the crystal, is regarded as a possible outcome of a random variable driven by a deterministic term. Indeed, each crystal does not grow in the same manner and some dispersion, in size, of the population is always observed. This random variable will be thus characterized uniquely by its Probability Density Function (PDF) whose evolution in time can be described in terms of a the FPE. Within this context, the FPE could be considered as an alternative way to develop a population balance, taking into account the natural fluctuations present in the crystallization process, and allowing describing, in a compact form, the PSD in time. The deterministic contribution driving the crystal growth is modeled by a growth equation.

However, in the FPE formulation, the model behavior is affected by both the deterministic and stochastic contribution. Indeed, the specific form of the stochastic model may lead to different shapes for the predicted probability density function, even being equal the nature of the deterministic part.

In this Thesis the mathematical models description starts with a brief definition of a generic population balance and then the stochastic models will be discussed. This Thesis is mainly focused on the modeling of nonisothermal antisolvent crystallization processes through a stochastic modeling, in particular using the Fokker-Planck Equation FPE in order to describe the time evolution of the CSD. The main contribution of this chapter is the formulation of the FPE for an accurate description of the CSD evolution, considering a logistic model to describe the time evolution of the mean size of crystals and a Geometric Brownian Motion (GBM) to model the noise intensity of the stochastic model. A simplified model is then formulated, in order to allow the system to be more suitable for a control and an optimization point of view. The simplified model leads to an analytical solution able to describe separately the mean

and the variance evolution of the CSD, allowing the formulation of operating maps, describing the asymptotic condition of the process in terms of mean and variance as a function of antisolvent feedrate and temperature.

3.1 Population Balances

A population balance allows for the tracking of a distribution of particles as they grow in solution. Traditionally, a complete population balance crystallization model is comprised of a population balance with corresponding crystallization kinetics, mass balance, and solubility model [Mullin, 2001]. Here, the crystal growth is assumed as size independent and with negligible attrition and agglomeration. As a further assumption, the only internal coordinate, which uniquely identifies the crystal, is its size L. Within these assumptions the PBE has the following form:

$$\frac{\partial n(L,t)}{\partial t} + \frac{n(L,t)}{V}\frac{dV}{dt} + G\frac{\partial n(L,t)}{\partial L} - B = 0 \tag{3.1}$$

where $n(L,t)$ is the crystal density (# of particles/m^4), V is the reaction volume (m^3), G is the growth rate (m/s), and B is the nucleation rate (# of particles/m^4/s).

It should be remarked that $n(L,t)\Delta L$ is the number of particles in a unit volume having size between L and $L+\Delta L$, thus the zero order moment of the distribution $\mu_0(t)$ (# of particles/m^3) corresponds to the number of crystals in a unit volume.

$$\mu_0(t) = \int_0^\infty n(L,t)dL \tag{3.2}$$

The nucleation and growth rates used in the population balance were modeled using Equations 3.3 and 3.4:

$$B = b_0 (T - 273) exp\left(- b_1 \frac{log^3 \left(\frac{\rho_C}{C\rho_S} \right)}{log^2 (S)} \right) \tag{3.3}$$

$$G = g_0 \left[1 - g_1 (1 + w)^{g_2} \right] \exp\left(\frac{-g_3}{RT} \right) \left(T - 273 \right)^{g_4} \Delta C^{g_5 w + g6} \tag{3.4}$$

where b_0 and b_1 are nucleation parameters, and $g_0, g_1, g_2, g_3, g_4, g_5$ and g_6 are growth parameters. ρ_C is the crystal density of sodium chloride (kg/m^3), C^* is the equilibrium concentration (kg NaCl/kg solvents), $\Delta C = C - C^*$ is the absolute supersaturation (kg/m^3), and $S = C / C^*$ is the relative supersaturation. ρ_S is the solution density (kg/m^3), w is the solute free mass percent of antisolvent (ethanol) in the solution, R is the ideal gas constant, and T is temperature (K). For the nucleation kinetics, b_0 is the temperature dependent term, and there is no explicit antisolvent composition dependence. The growth kinetic is explicitly dependent on both temperature and solvent composition. The parameter g_0 represents the default growth rate, and parameters g_1 and g_2 represent the reduction in growth rate due to antisolvent addition. Parameters g_3 and g_4 represent the growth rate temperature dependence, and g_5 is the supersaturation growth rate exponent. Thus, it is hypothesized that crystal growth approaches zero at a certain critical ethanol composition for the similar NaCl compound.

In order to evaluate the absolute and relative supersaturation used in the kinetic equations, a solubility model is needed to calculate the corresponding equilibrium concentration.

$$C^* = \begin{cases} c_1 w^2 + c_2 w + c_3 & w \le 0.849 \\ 0 & w > 0.849 \end{cases} \quad (3.5)$$

Where, $c_1 = 20.678$, $c_2 = -59.294$, and $c_3 = 20.678$ over solute free ethanol mass fractions less than 0.849. On the other hand, solute free ethanol mass fractions greater than 0.849 were set to an equilibrium solubility of zero. Dependence of the sodium chloride solubility on the temperature is assumed to be negligible over the range of temperatures used in our experiments. The percent change in solubility for NaCl in water of a twenty degree temperature change from 30 °C to 10 °C is 1.1% [Mullin, 2001].

The mass balance of the solute in solution for fed-batch antisolvent crystallization is:

$$\frac{d(Cm_S)}{dt} = -3\rho_C k_v V \int_0^{+\infty} GL^2 n(L,t) dL \quad (3.6)$$

where C is the solute concentration (kg solute/kg solvents), k_v is the volumetric shape factor of the crystal, ρ_C is the solid density of the crystal, and m_s is the mass of the solvent. For sodium chloride: k_v, and ρ_C are 1, and 2165 kg/m^3 respectively [Feldman, 2005]. No energy balance was explicitly specified in the crystallization model: it is assumed that the control system maintains the reactor temperature at the set-point specified.

Numerical Methods

The population balance was solved using the method of lines discretization technique. This technique converts the partial differential equation into a system of ordinary differential equations with corresponding boundary and initial conditions shown in Equation Set 3.7.

$$\begin{aligned}
&\frac{dn_1}{dt} = B - G\frac{n_1}{2\delta_1} - \frac{n_1}{V}\frac{dV}{dt} \\
&\frac{dn_i}{dt} = G\left(\frac{n_{i-1}}{2\delta_{i-1}} - \frac{n_i}{2\delta_i}\right) - \frac{n_i}{V}\frac{dV}{dt} \qquad i = 2...\zeta \\
&L_1(t) = 0.1\ \mu m \\
&L_\zeta(t) = 10000\ \mu m \\
&n(L_i, t=0) = 0 \qquad i = 1...\zeta \\
&n(L_1, t) = 0 \\
&n(L_\zeta, t) = 0
\end{aligned} \tag{3.7}$$

where ζ is the number of discretization intervals, and δ is the length of each discretization interval given by:

$$\delta_i = L_i - L_{i-1} \qquad i = 1,...,\zeta \tag{3.8}$$

The individual discretization lengths are chosen using a geometric series:

$$\begin{aligned}
&L_i = L_0 b^i \qquad i = 0,...,\zeta \\
&b = \left(\frac{L_{max}}{L_0}\right)^{\frac{1}{\zeta}}
\end{aligned} \tag{3.9}$$

where L_0 is the nucleate size and $L_{\max}$ is the maximum crystal size used in the discretization.

3.2 Langevin Equation

Here, it is introduced a simple unstructured population model, where the crystals are classified by their size, L. The growth of each individual crystal is supposed to be independent by the other crystals and is governed by the same deterministic model. In order to take into account the growth fluctuations and the unknown dynamics not captured by the deterministic term, a random component can be introduced [Risken, 1984]. The stochastic model can thus be written as a Langevin equation of the following type:

$$\frac{dL}{dt} = Lf(L,t;\theta) + g(L)\eta(t) \tag{3.10}$$

where L is the size of the single crystal, t is the time, $f(L,t;\theta)$ is the expected rate of growth of L, θ is the vector parameter defined in the model, $\eta(t)$ is the Langevin force and $g(L)$ is the diffusion coefficient, assumed to depend also on L. It is further assumed that:

$$\begin{aligned} &E[\eta(t)] = 0 \\ &E[\eta(t)\eta(t')] = g(L)\delta(t-t') \end{aligned} \tag{3.11}$$

Equation 3.10 implies that the crystal size L behaves as a random variable, characterized by a certain Probability Density Function (PDF) $\psi(L,t)$ depending on the state variables of the system, i.e.: the size L and time t. Incidentally, it should be noted that one can regard the probability density $\psi(L,t)$ as the relative ratio of crystals having a given dimension L in the limit of infinite observations. Thus, from a practical point of view, it coincides with the normalized Particle Size Distribution experimentally observed.

The diffusion term $g(L)$ determines the random motion of the variable L that takes into account the fluctuation in the particle growth process. We focus on formulating $g(L)$ as function of the FPE diffusivity coefficient D as well as the crystal size L as follows:

$$g(L) = 2\sqrt{D}L^{\alpha} \tag{3.12}$$

where α is a parameter which allows to introduce some degree of flexibility in incorporating the functionality between $g(L)$ and the particle size L. The specific form of $g(L)$ may lead to different shapes for the probability density function.

Substituting this definition on the Langevin equation (Equation 3.10) we have:

$$\frac{dL}{dt} = Lf(L,t;\theta) + 2\sqrt{D}L^{\alpha}\eta(t) \tag{3.13}$$

Equation 3.13 can be manipulated to obtain the Langevin equation for the new random variable $y = \ln(L)$:

$$\frac{1}{L}\frac{dL}{dt} = f(L,t;\theta) + 2\sqrt{D}L^{\alpha-1}\eta(t) \tag{3.14}$$

that is

$$\frac{dy}{dt} = h(y,t;\theta) + 2\sqrt{D}e^{y^{\alpha-1}}\eta(t) \tag{3.15}$$

where $h(y,t;\theta)$ is the expected growth rate of the crystal in the new coordinate y.

3.3 The Fokker-Planck Equation (FPE)

In order to integrate the solution of the Equation 3.10 and find the time evolution of the PDF $\psi(L,t)$, that from now we will call Crystal Size Distribution CSD, the Fokker-Planck Equation in Stratanovich form has been used.

The time evolution of the CSD $\psi(L,t)$, at any instant of time t, follows the linear Fokker-Planck Equation that, in Stratanovich form, is given by [Risken, 1984]:

$$\frac{\partial \psi(L,t)}{\partial t} = \frac{\partial}{\partial L}\left[g(L)\frac{\partial}{\partial L}\left(g(L)\psi(L,t)\right)\right] - \frac{\partial}{\partial L}\psi(L,t)Lf(L,t,\theta) \quad (3.16)$$

along the boundary conditions:

$$g(0)\frac{\partial}{\partial L}g(0)\psi(0,t) = 0 \quad (3.17a)$$

$$\frac{\partial}{\partial L}\psi(\infty,t) = 0 \quad (3.17b)$$

The reflecting boundary conditions in Equation 3.17a ensures that the elements of the population will never assume negative values, whereas Equation 3.17b ensures the decay condition on $\psi(L,t)$ as L goes to infinity, for any time.

Changing the random variable as $y = \ln(L)$, the FPE for the new random variable y can be thus rewritten as a function of α as:

$$\frac{\partial \psi(y,t)}{\partial t} = D \cdot \frac{\partial}{\partial y}\left[e^{y(\alpha-1)}\frac{\partial}{\partial y}\left(e^{y(\alpha-1)}\psi(y,t)\right)\right] - \frac{\partial}{\partial y}\psi(y,t)h(y,t;\theta) \quad (3.18)$$

or

$$\frac{\partial \psi(y,t)}{\partial t} = e^{-2y+2\alpha y}\left[\frac{\partial^2 \psi}{\partial y^2} + 3(-1+\alpha)\frac{\partial \psi}{\partial y} + 2(-1+\alpha)^2\psi(y,t)\right] - \frac{\partial}{\partial y}\psi(y,t)h(y,t;\theta) \quad (3.19)$$

In the new variable y, the boundary conditions become:

$$\frac{\partial}{\partial y}\psi(-\infty,t) = 0 \quad (3.20a)$$

$$\frac{\partial}{\partial y}\psi(+\infty,t)=0 \tag{3.20b}$$

The initial condition used for the FPE in logarithmic scale is Gaussian distribution, based on the initial mean size of crystals and the initial variance, defined as $N(\mu_{y0},\sigma_{y0}^2)$, where μ_{y0} represents the initial mean size of crystals, based on the experimental data, and σ_{y0}^2 is the initial variance of the experimental CSD, both evaluated at $t=t_0$.

It should be pointed out that this variable transformation allows a more easy and efficient integration of the FPE.

We can have a number of alternative formulations depending on the value of parameter α. For a purely random process (deterministic drift term equal to zero i.e.: $f(L,t;\theta)=h(L,t;\theta)=0$) the behavior of the PDF shapes, $\psi(L,t)$, as a function of α, can be readily analyzed. In this case, the problem may be represented by Equation 3.21:

$$\frac{\partial\psi}{\partial t}=\frac{\partial}{\partial L}\left(\sqrt{D}L^{\alpha}\frac{\partial\left(\sqrt{D}L^{\alpha}\psi\right)}{\partial L}\right),\qquad \psi(0)=\delta(L-L_0) \tag{3.21}$$

which has an analytical solution for the probability distribution given by:

Linear Scale:

$$\psi(L,t)=\frac{1}{\sqrt{2\pi Dt}L^{\alpha}}\exp\left(-\frac{1}{2}\frac{\left(L^{1-\alpha}-L_0^{1-\alpha}\right)^2}{(1-\alpha)^2Dt}\right) \tag{3.22a}$$

with $(L>0,\alpha\neq 1)$

$$\psi(L,t)=\frac{1}{\sqrt{2\pi Dt}L}\exp\left(-\frac{1}{2}\frac{(\ln L-\ln L_0)^2}{Dt}\right) \tag{3.22b}$$

with $(L>0,\alpha=1)$

Logarithmic scale:

$$\psi(y,t)=\frac{1}{\sqrt{2\pi Dt}}\exp\left((1-\alpha)y-\frac{1}{2}\frac{\left(\exp(y(1-\alpha))-\exp(y_0(1-\alpha))\right)^2}{(1-\alpha)^2 Dt}\right) \quad (3.23a)$$

with $(\alpha\neq 1)$

$$\psi(y,t)=\frac{1}{\sqrt{2\pi Dt}}\exp\left(-\frac{1}{2}\frac{(y-y_0)^2}{Dt}\right) \quad (3.23b)$$

with $(\alpha=1)$

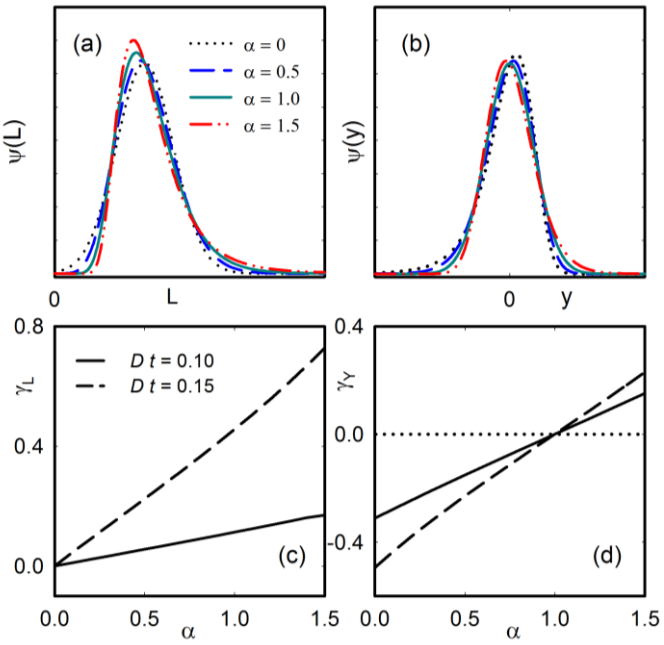

Figure 3.1: PDF for a purely random process ($Dt=0.1$) in the (a) logarithmic scale and (b) linear scale, for $\alpha=0$ (dotted line), $\alpha=0.5$ (blue dashed line), $\alpha=1$ (green solid line), $\alpha=1.5$ red (dashed-dotted

line). The skewness of the PDF with respect to α is also reported for the logarithmic scale (panel c) and the linear scale (panel d) for $Dt = 0.1$ (solid line) and $Dt = 0.15$ (dashed line).

One should notice that, for a purely stochastic equation, the solution depends only on the dimensionless parameter group Dt and the initial condition (L_0 or y_0). Furthermore the distribution tends to indefinitely widen as time increases.

Figure 3.1 illustrates some properties of the solutions of Equations 3.22 (left panels: a and c) and 3.23 (right panels b and d). In more detail the first row reports some PDF for a range of values of α and for a fixed $Dt = 0.1$. In particular, we look at values of $\alpha = 0$ (diffusion term independent of particle size, hereafter referred as Linear Brownian Motion, LBM); $\alpha = 1$ (diffusion term linearly dependent of the particle size, hereafter referred as Geometric Brownian Motion, GBM), $\alpha = 0.5$ and $\alpha = 1.5$ (nonlinear diffusive term). The second rows reports the skewness γ of the PDF in Equation 3.22 (panel c) and Equation 3.23 (panel d) as a function of the α parameter for two different values of Dt ($Dt = 0.1$ and $Dt = 0.15$). One should remind that the skewness is a measure of the asymmetry for a given PDF of a generic random variable z and is usually defined as:

$$\gamma_Z = \frac{\int_\Omega (z - \mu_Z)^3 \psi_Z(z) dz}{\left(\int_\Omega (z - \mu_Z)^2 \psi_Z(z) dz \right)^{\frac{3}{2}}} \tag{3.24}$$

where Ω is the z domain. In the following we refer to γ_L when the skewness is evaluated in the linear scale ($z = L$), whereas we refer to γ_y for the skewness evaluated in the logarithmic scale ($z = y = \log L$). In Equation 3.24, μ_Z is the expected value of the random variable z:

$$\mu_Z = \int_{\Omega} z\psi_Z(z)dz \tag{3.25}$$

As illustrated in Figure 3.1, the selection of α has a strong implication on the shape of the PDF: for $\alpha = 0$ the typical Wiener process can be recovered and the probability distribution obtained using the FPE results in a Gaussian asymptotic shape when regarded in the L domain. This is evident in Figure 3.1.c where it is shown that $\gamma_L = 0$ at $\alpha = 0$, for any Dt parameter value. Conversely, for positive values of α Log-normal ($\alpha = 1$, Geometric Brownian Motion, GBM) and stretched Gaussian ($\alpha = 0.5$ or $\alpha = 1.5$) PDF shapes are obtained [Fa, 2005]. The case $\alpha = 1$ is again a special instance: indeed the lognormal distribution corresponds to a Gaussian distribution when regarded in the logarithmic scale, thus the solution should appear as Gaussian when evaluated in the $y = \log L$ domain. These features are confirmed in Figure 3.1.d where $\gamma_y = 0$ when $\alpha = 1$ for any Dt parameter value. Consequently, we will formulate and assess the performance of the FPE model to describe the crystal growth process for a range of values of α covering a number of cases ranging from Gaussian and Stretched Gaussian asymptotic behaviors.

It is worth pointing out that in the presence of a drift term different from zero ($f(L,t;\theta) \neq 0$ or $h(L,t;\theta) \neq 0$), some distortion of the PDF from the pure stochastic situation could be expected.

In Table 3.1 a brief overview of the Langevin and Fokker-Planck equations, corresponding to the cases $\alpha = 0$, $\alpha = 0.5$, $\alpha = 1$ and $\alpha = 1.5$, is reported.

α	Equation	
0	LE $\frac{dy}{dt} = h(y,t;\theta) + 2\sqrt{D}e^{-y}\eta(t)$	(3.26)
	FPE $\frac{\partial\psi(y,t)}{\partial t} = D\cdot e^{-2y}\left(\frac{\partial^2\psi}{\partial y^2} - 3\frac{\partial\psi}{\partial y} + 2\psi\right) - \frac{\partial}{\partial y}\psi(y,t)h(y,t;\theta)$	(3.27)

0.5	LE	$\frac{dy}{dt} = h(y,t;\theta) + 2\sqrt{De}^{-\frac{y}{2}}\eta(t)$	(3.28)
	FPE	$\frac{\partial\psi(y,t)}{\partial t} = De^{-y}\left(\frac{\partial^2\psi}{\partial y^2} - \frac{3}{2}\frac{\partial\psi}{\partial y} + \frac{1}{2}\psi\right) - \frac{\partial}{\partial y}\psi(y,t)h(y,t;\theta)$	(3.29)
1	LE	$\frac{dy}{dt} = h(y,t;\theta) + 2\sqrt{D}\eta(t)$	(3.30)
	FPE	$\frac{\partial\psi(y,t)}{\partial t} = D\frac{\partial^2\psi}{\partial y^2} - \frac{\partial}{\partial y}\psi(y,t)h(y,t;\theta)$	(3.31)
1.5	LE	$\frac{dy}{dt} = h(y,t;\theta) + 2\sqrt{De}^{\frac{y}{2}}\eta(t)$	(3.32)
	FPE	$\frac{\partial\psi(y,t)}{\partial t} = De^{y}\left(\frac{\partial^2\psi}{\partial y^2} + \frac{3}{2}\frac{\partial\psi}{\partial y} + \frac{1}{2}\psi\right) - \frac{\partial}{\partial y}\psi(y,t)h(y,t;\theta)$	(3.33)

Table 3.1: Langevin and FP equations for different α values.

3.4 Logistic Model

Regarding the deterministic part of the Langevin Equation, and then the FPE model, the purpose is to choose a model as simple as possible. To this end, the Logistic equation [Tsoulauris and Wallace, 2002], is possibly the best-known simple sigmoidal asymptotic function used to describe the time dependence of growth processes in an unstructured fashion:

$$h(y) = ry\left(1 - \frac{y}{K}\right) \tag{3.34}$$

This choice is mainly motivated to the requirement for a simple model with a parsimonious number of adjustable parameters, i.e., the growth rate, r, and the asymptotic equilibrium value K. The present growth model can be regarded as one of the simplest model taking into account mild nonlinearities. In spite of its simplicity, this model provides the main qualitative features of a typical growth

process: the growth follows a linear law at low crystal size values and saturates at a higher equilibrium value as shown in Figure 3.2.

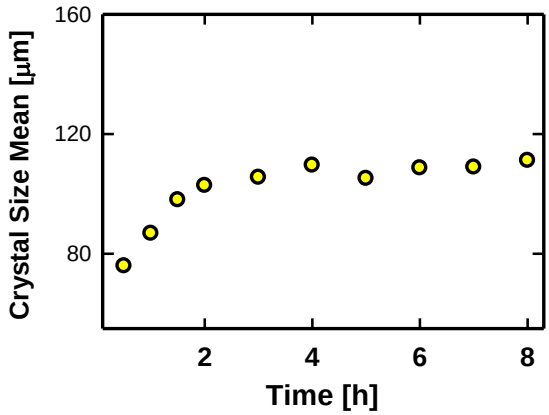

Figure 3.2: Experimental trajectory of the mean size of crystals.

Substituting the Equation 3.34 on the Equation 3.18 and considering a value of the parameter α equal to one, obtained from the parameters estimation on experimental CSDs and explained in Chapter 5, the FPE can be rewritten as:

$$\frac{\partial \psi(y,t)}{\partial t} = D\frac{\partial^2 \psi(y,t)}{\partial y^2} - ry\left(1-\frac{y}{K}\right)\frac{\partial \psi(y,t)}{\partial y} - r\left(1-\frac{2y}{K}\right)\psi(y,t) \quad (3.35)$$

Finally the evolution in time of the probability density is described in terms of a linear, partial differential equation depending on the parameters r (linear Malthusian growth rate), K (asymptotic crystal size) and D (diffusivity), that are assumed to depend on the feeding conditions.

It should be remarked that the Equation 3.35 is a linear PDE but with non-linear coefficients, consequently hard to find an analytical solution. For this equation in the next chapter will be used a numerical integration for the parameter estimation and for the model validation.

3.5 Ornstein Uhlenbeck Process

On previous paragraph Equation 3.35 being a linear PDE with non-linear coefficient, it is not easy to find an analytical solution. As it regards the deterministic term $f(L,t;\theta)$, here a Gompertz model (GM) for the crystal growth [Sahoo et al, 2010] is assumed, in consideration to the logarithmic scale used for the CSD data:

$$\frac{dL}{dt} = -\alpha L \ln\frac{L}{L_0} \tag{3.36}$$

One should remark that, in absence of noise the model tends towards a stable stationary solution at $L = L_0$ like the logistic model 3.34. Gompertz Equation 3.38 can be further manipulated:

$$\frac{1}{L}\frac{dL}{dt} = \frac{dlnL}{dt} = -\alpha\left(lnL - lnL_0\right) + \eta(t) \tag{3.37}$$

Introducing again the new variable $y = \ln L$, one can end up with a new stochastic equation for the random variable y:

$$\frac{dy}{dt} = r'\left(1 - \frac{y}{K'}\right) + \eta(t) \tag{3.38}$$

with $K' = \ln L_0$ and $r' = \alpha \ln L_0$.
The corresponding FPE equation becomes:

$$\frac{\partial\psi(y,t)}{\partial t} = D'\frac{\partial^2\psi(y,t)}{\partial y^2} - \frac{\partial}{\partial y}h(y,t;\theta)\psi(y,t) \tag{3.39}$$

Introducing a linear variable transformation $z = -\left(1 - y/K'\right)$, an Ornstein-Uhlenbeck Process (OUP) can be obtained, which can be

described by the following Fokker-Planck Equation with a Gompertz law growth term (FPE-GM):

$$\frac{\partial \psi(z,t)}{\partial t} = D'' \frac{\partial^2 \psi(z,t)}{\partial z^2} + r'' \frac{\partial}{\partial z} z \psi(z,t) \tag{3.40}$$

where $D'' = D' / K'^2$ and $r'' = r' / K'$.

Equation 3.42 is defined for $t \in]t_0, +\infty[$ and $z \in]-\infty, +\infty[$. The initial condition for $t = t_0$ is defined as a normal distribution:

$$\psi(z,t_0) = \frac{1}{\sigma_{z0}\sqrt{2\pi}} exp\left[-\frac{(z-\mu_{z0})^2}{2\sigma_{z0}^2} \right] \tag{3.41}$$

where $\mu_{z0} = \frac{\mu_{y0}}{K'} - 1$ and $\sigma_{z0}^2 = \frac{\sigma_{y0}^2}{K'^2}$.

3.6 Analytical Solution of the FPE

Analogy with the Kalman Filter

It can be demonstrated that, when dealing a FPE based on an Ornstein-Uhlenbeck Process, Equation 3.42, and the initial conditions are assumed to be Gaussian, Equation 3.44, the form of the PDF will stay Gaussian at any time [Risken, 1996; Jazwinsky, 1970]. Thus the first two moments of the distribution: mean, $\mu_y(t)$, and variance, $\sigma_y^2(t)$ uniquely identify the probability density function $\psi(y,t)$.

$$\psi(y,t) = N\left(\mu_y(t), \sigma_y^2(t)\right) \tag{3.42}$$

where:

$$\begin{aligned}\mu_y(t) &= \int_{-\infty}^{+\infty} y\psi(y,t)dy \\ \sigma_y^2(t) &= \int_{-\infty}^{+\infty} \left(y-\mu_y(t)\right)^2 \psi(y,t)dy\end{aligned} \tag{3.43}$$

The first moment follow the deterministic Gompertz equation (in logarithmic scale), and, therefore, the analytical solution is given by the following equation:

$$\mu_y(t) = K^{'}\left[1-\left(1-\frac{\mu_{y0}}{K^{'}}\right)\exp\left(-\frac{r^{'}(t-t_0)}{K^{'}}\right)\right] \tag{3.44}$$

where $K^{'}$ is the average asymptotic size of the crystals dimension, r is the growth rate, t_0 is the starting time of the run and μ_{0y} is the initial mean size of crystals at $t = t_0$.

The second moment can be described by considering the analogy between the FPE and the Kalman filter [Jazwinsky, 1970] for a linear process, and then the Riccati's equation will describe the variance changes in time. Writing the Riccati's equation for a Kalman filter for one single state without measurement, we have:

$$\frac{d\sigma_y^2(t)}{dt} = \Gamma^2 + 2A\sigma_y^2(t) \tag{3.45}$$

where $\sigma_y^2(t)$ is the variance, $\Gamma^2 = 2D^{'}$ is the noise intensity, and $A = -r^{'}/K^{'}$ is the coefficient of the state variable of the system. Thus, the analytical solution of the variance $\sigma_y^2(t)$ with respect to the time is given by:

$$\sigma_y^2(t) = \sigma_{y0}^2\exp\left(-\frac{2r^{'}(t-t_0)}{K^{'}}\right) + \frac{D^{'}K^{'}}{r^{'}}\left[1-\exp\left(-\frac{2r^{'}(t-t_0)}{K^{'}}\right)\right] \tag{3.46}$$

Thus, the analytical solution of the Equation 3.41 is eventually:

$$\psi(y,t) = \frac{1}{\sigma_y(t)\sqrt{2\pi}} exp\left[-\frac{\left(y - \mu_y(t)\right)^2}{2\sigma_y^2(t)} \right] \tag{3.47}$$

where the time evolution of $\mu_y(t)$ and $\sigma_y^2(t)$ are given in the Equations 3.46 and 3.48, respectively.

Furthermore, it can be noticed that the analytical solution is a log-normal distribution when rewritten in the linear scale L:

$$\psi(L,t) = \frac{1}{\sigma_y(t)L\sqrt{2\pi}} exp\left[-\frac{\left(lnL - \mu_y(t)\right)^2}{2\sigma_y^2(t)} \right] \tag{3.48}$$

$L \geq 0$

The first two moments of the distribution $\psi(L,t)$ in the linear scale can then be evaluated as:

$$\mu_L(t) = \int_{-\infty}^{+\infty} L\,\psi(L,t)dL = \exp\left(\mu_y(t) + \frac{\sigma_y^2(t)}{2} \right) \tag{3.49}$$

$$\sigma_L^2(t) = \int_{-\infty}^{+\infty} \left(L - \mu_L(t)\right)^2 \psi(L,t)dL = \exp\left(2\mu_y(t) + \sigma_y^2(t)\right)\left(e^{\sigma_y^2(t)} - 1\right) \tag{3.50}$$

Equations 3.46, 3.48 and 3.49 (or conversely Equations 3.50, 3.51 and 3.52) provide a time evolution of the PSD as function of the model parameters in terms of the first two stochastic moments (mean size of crystals and variance of the PSD) available in an analytical form, which can be a valuable information for the design of proper offline and/or online model based control strategies.

Rigorous Solution

It is also possible to obtain the analytical solution of the FPE-GM using a rigorous mathematical approach, based on the Fourier transform properties.

Considering the FPE-GM and its initial condition, already linear-transformed along the variable z, it is possible to apply the Fourier transform, which is defined as:

$$\tilde{\Psi}(k,t) = \frac{1}{\sqrt{2\pi}} \int_{-\infty}^{+\infty} \psi(z,t) \exp(-ikz) dz \tag{3.51}$$

where k is the projection of z on the Fourier domain.
The resulting Equations 3.40 and 3.41 on the Fourier domain applying the 3.51 are:

$$\frac{\partial \tilde{\Psi}(k,t)}{\partial t} = -r^{"} k \frac{\partial \tilde{\Psi}(k,t)}{\partial k} - D^{"} k^2 \tilde{\Psi}(k,t) \tag{3.52}$$

$$\tilde{\Psi}(k,t_0) = \frac{1}{\sqrt{2\pi}} \exp\left(-\frac{\sigma_{z0}^2 k^2}{2} - ik\mu_{z0} \right) \tag{3.53}$$

Now applying the Method of Characteristics (MOC), it is possible to transform the equations 3.52 and 3.53 in a system of ODE. In order to apply the MOC we need to define the new dependent variable as follows:

$$\tilde{\Psi}(k,t) = \tilde{\Psi}(k(s),t(s)) \tag{3.54}$$

where performing the differential of the 3.54 and dividing both members by ds, we have:

$$\frac{d\tilde{\Psi}}{ds} = \frac{\partial \tilde{\Psi}}{\partial k}\frac{dk}{ds} + \frac{\partial \tilde{\Psi}}{\partial t}\frac{dt}{ds} \tag{3.55}$$

From the analogy with the 3.52 we can write the following ODE system:

$$\begin{cases} \dfrac{dt}{ds} = 1 \\ \dfrac{dk}{ds} = r^{"}k \\ \dfrac{d\tilde{\Psi}(k,t)}{ds} = -D^{"}k^{2}\tilde{\Psi}(k,t) \\ \tilde{\Psi}(k,t_{0}) = \dfrac{1}{\sqrt{2\pi}} exp\left(-\dfrac{\sigma_{z0}^{2}k^{2}}{2} - ik\mu_{z0} \right) \end{cases} \tag{3.56}$$

Solving the system 3.56, applying the initial condition given by the last equation on the system, we obtain the following solution, in the Fourier domain:

$$\tilde{\Psi}(k,t) = \frac{1}{\sqrt{2\pi}} \exp\left\{ -ik\mu_{z0} e^{-r^{"}(t-t_0)} - \frac{k^{2}\sigma_{zo}^{2}}{2} e^{-2\nu(t-t_0)} - \frac{D^{"}k^{2}}{2r^{"}} \left[1 - e^{-2r^{"}(t-t_0)} \right] \right\} \tag{3.57}$$

Applying the Fourier antitransform defined as follows:

$$\tilde{\Psi}(k,t) = \frac{1}{\sqrt{2\pi}} \int_{-\infty}^{+\infty} \Psi(z,t) \exp(ikz) dz \tag{3.58}$$

Substituting again the definition of the variable *z* used for the linear transformation of the FPE-GZ, it is possible to obtain the same solution obtained in Equations 3.48, 3.49 and 3.50.

Chapter 4

Experimental Setup

In this Chapter will show all the experimental procedure, considering the equipment used and all the different runs performed, in order to realize this Thesis. All the experiments used for this Thesis were carried out in a bench scale crystallizer. Only purified water, reagent grade sodium chloride (99.5%), and 95% in volume for antisolvents were used. In this Chapter will be also illustrated the methodology to analyze the experimental data, from the experimental samples, until the Crystal Size Distribution, CSD, both offline and online. The Chapter concludes with the last part of this Thesis, concerning the influence of the hydrogen bonding on the supersaturation of the system, illustrating all the experiments to validate the hypothesized mechanism.

4.1 The Crystallizer

The experimental rig is made up of one liter glass, jacketed cylindrical crystallizer, connected to a heating/cooling bath controller. The temperature in the crystallizer is measured using an RTD probe which is wired up to a slave temperature control system capable of heating and cooling.

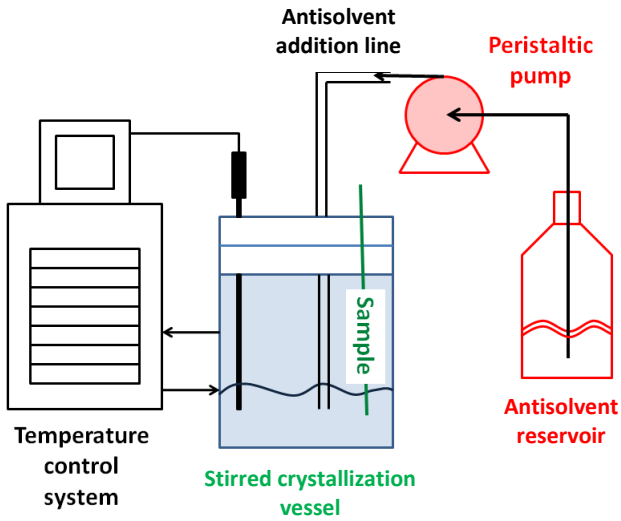

Figure 4.1: Crystallizer setup.

Figure 4.2: Crystallizer.

In similar fashion, the antisolvent addition is carried out by a slave peristaltic pump. The master control is performed by a computer control system which is wired up to the slave temperature and flow-rate controllers respectively. The desired set-points are set by the master controller. All relevant process variables are recorded.

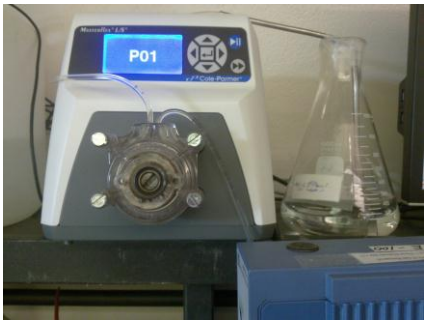

Figure 4.3: Peristaltic pump with the antisolvent reservoir.

Figure 4.4: Thermostatic bath. →

4.2 Offline Sampling

During the experimental runs, about 8 ml samples were taken in an infrequent fashion using a syringe pump connected by a hose inside the crystallizer. Samples were then vacuum-filtered over a filter paper and then dried into an oven overnight with a constant temperature of 50 °C for further visual inspection (Grosso et. al., 2010).

Figure 4.5: Manual vacuum pump connected to a filter flask.

In order to analyze the previously taken and dried out overnight samples, part of the crystals on the filter paper for each sample have been analyzed with a light microscopy. In order to analyze the samples of crystals, they have been wetted using pure ethanol, in order to spread out the crystals onto the microscope slide. For each sample have been prepared three slides and for each slide have been taken at least four images in order to obtain an independent and an identically distributed CSD. All the images have been taken in tiff format in high resolution using stereo light microscope (Wild-Heerbrugg, Switzerland) which connected to a digital camera (Amscope Model MD500, United States). All the images have been analyzed later using the AmScope software (iScope, United States), the software allows for the measurement of the length or area of particular crystals in units of pixels. Using a supplied calibration slide, these lengths and areas can be converted from pixels to a micron length scale. The number of crystals measured varied for each sample and was fixed by a stabilization criterion of ±2.5% of the mean.

4.3 Online Sampling

During the experimental runs an online sampling device has been developed and tested out. The device is a flow cell made in polycarbonate, slide-like shaped, in which a flow of solution is continuously recirculated from the crystallizer using a peristaltic pump. The cell has a path, properly studied to allow the crystals to flow in a certain section for a better analysis using the optical microscope. Using the optical microscope, all the images have been taken using a jpeg format and proper resolution in order to allow the image storing to take a clear image without any blurry effect or any kind of distortion. The flow rate has been also slowed down in order to allow the crystals to gradually distribute into the cell in order to take images with a high number or particles. Those images have been taken in an infrequent fashion during the experimental run, with a number of images varying considering the density of crystals in each image. The image processing has been obtained using the same method described on the previous paragraph, for the offline sampling.

Figure 4.6: Online sampling device with the optical microscope and the peristaltic pump.

This method will be used for future research in order to develop a soft sensor for the online CSD measurement, based on the image processing using a wavelet approach, and furthermore used to develop a real time crystal size controller.

4.4 Image Analysis and CSD Definition

In order to define the crystal size distribution, or in general the Particle Size Distribution (PSD), the first step to do is the image analysis in which the particles are manually measured with a software called AmScope®, that allows to select the contours of the particles or any shape present in the photos. This operation is done for all the samples, using the photos taken from the slides until the number of crystals is sufficient to obtain a stabilization criterion of ±2.5% of the mean. The mean size, obtained considering the diagonal of a squared face shaped crystal, is concerted from pixels to micron scale using a proper calibration slide. The final result is a histogram representation of the CSDs.

The crystal size sample is further processed in order to estimate the related probability density function. To this end, a non-parametric method was used and the experimental probability density distribution was eventually estimated as a linear combination of kernel basis functions:

$$\psi(L) = \frac{1}{nh}\sum_{i=1}^{n}\frac{1}{\sqrt{2\pi}}\exp\left(-\frac{(L-L_i)^2}{2h^2}\right) \tag{4.1}$$

where n is the crystal sample dimension, L_i is the i-th observation and the bandwidth parameter h is given by [Silverman, 1986]:

$$h = 1.06\sqrt{s_L^2}\,n^{-0.2} \tag{4.2}$$

In Equation (4.2), s_L^2 is the sample variance. An example of the distribution estimation obtained with the crystal sample is reported in Figure 4.7:

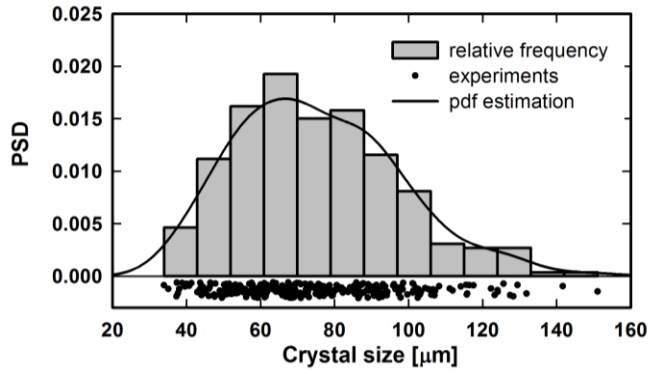

Figure 4.7: Relative frequency density of the crystal sample at feed rate q = 1.5 ml/min and t = 0.5 h (bars), compared with the kernel approximation (solid line). The n observations of the sample are also reported at the bottom of the figure (black dots).

Figures 4.8 and 4.9 illustrate the experimental PSD evolution (obtained using the kernel density estimation) with time for the intermediate feed rate, (MFR, 1.5 ml/min) both in the linear and logarithmic scale.

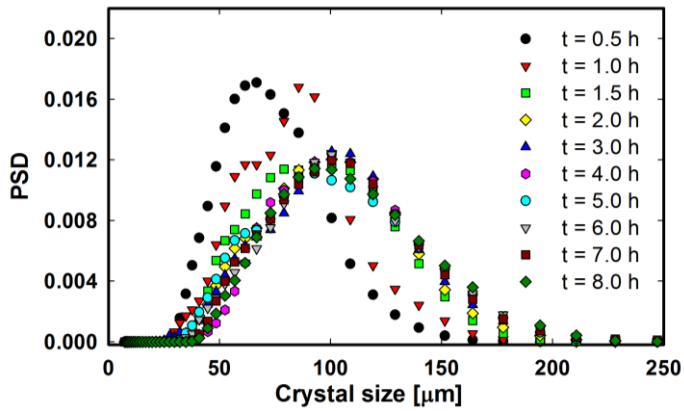

Figure 4.8: Obtained PSD from experimental data for MFR at different sampling times during the batch (linear scale).

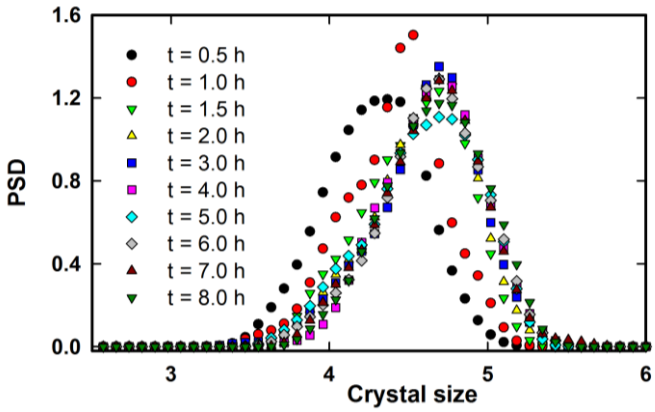

Figure 4.6: Obtained PSD from experimental data for MFR at different sampling times during the batch (logarithmic scale).

The calibration of the proposed models is carried out separately for every run. The set of parameters $\theta = [\log_{10}(D), r, K]$ is inferred using two different procedures, i.e., Least Square Method (LS) on the Kernel based density function estimation and Maximum Likelihood Estimation Method (ML). It should be noted that $\log_{10}(D)$is used instead of D in order to reduce the statistic correlation between the parameters [Risken, 1996; Grosso et al, 2011].

In the Least Squares (LS) approach, the parameters in the model are estimated searching the minimum of the objective function given by the distance between the theoretical PSD $\Psi(y,t;\theta)$ carried out from numerical integration of the model (equations 3.10 and 3.40) where $\theta = [\log_{10}(D), r, K]$ and the experimental PSD $\Psi^*(y)$ estimated through kernel density based estimation [Silverman, 1986]:

$$\Psi^*(y) = \frac{1}{N\lambda} \sum_{i=0}^{N} \frac{1}{\sqrt{2\pi}} exp\left[-\frac{(y-\mu_i)^2}{2\lambda^2} \right] \tag{4.3}$$

In Equation 4.3 μ_i is the i-th crystal size value observed through visual inspection of the images, N is the crystals sample data dimension and λ is the bandwidth parameter, to be optimized for a satisfactory

description of the distribution [Silverman, 1986]. The distance between the distributions is evaluated at n different spatial location and m different time values for every operating condition:

$$\Phi(\theta) = \sum_{i=1}^{m} \sum_{j=1}^{n} \left[\Psi(y_i, t_i; \theta) - \Psi^*(y_j, t_i) \right] \tag{4.4}$$

Conversely, the Maximum Likelihood (ML) estimation approach, aims to determine the θ values that maximize the probability (likelihood) of the sample data. Thus, the parameters are inferred by searching the maximum of the log-likelihood function:

$$logL(y_i, t_j; \theta) = \sum_{j=1}^{m} \sum_{i=1}^{n_j} log\left(\Psi(y_i, t_j; \theta)\right) \tag{4.5}$$

ML estimation through equation (4.5) is possible only if the crystal observations can be assumed to be independent, that seems a reasonable hypothesis. The ML has been already used to infer the parameters related to the process steady state [Tronci et al, 2011; Cogoni et al, 2012] and it is demonstrated to give more efficient parameter estimation, that is, a minor number of experimental data are required to carry out an effective evaluation of the parameters, at least compared with the LS method. Indeed, since it achieves the Cramér-Rao lower bound, no asymptotically unbiased estimator has lower asymptotic mean squared error than the ML [Papoulis, 1991]. In addition, the introduction of possible errors in the evaluation of the experimental distribution (based on Equation 4.3) is in this way circumvented. Thus, the onerous step in the experimental activity represented by the data acquisition through visual inspection can be eventually reduced.

4.5 Antisolvents used and operating conditions

In order to perform all the experimental runs, different temperatures and different antisolvents, with different feedrates have been used in order to study their influence on the operating conditions. The different antisolvents have been chosen by their Polarity Index (PI), in order to study the influence of the hydrogen bond strength on the supersaturation of the solution and, since the PI involves hydrogen bonds within the antisolvent molecules or within antisolvent/solvent molecule, different temperatures and different antisolvent feedrates have been used in order to enhance this effect.

Below will be reported all the experimental runs conducted for this Thesis, for all the different phenomena considered.

Model Development: These proposed experimental runs have been used to develop the FPE model from the rigorous way until obtain the simplified linear model. This set of experiments also includes a validation run in isothermal conditions, described in Figure 4.9.

Running Time [h]	Antisolvent (PI)	Feedrate [ml/min]	Temperature [°C]
8	Ethanol (4.3)	0.7	20
8	Ethanol (4.3)	1.5	20
5	Ethanol (4.3)	3.0	20

Table 4.1: Qualitative effects of increasing the antisolvent feedrate, temperature and using and antisolvent polarity index on the asymptotic mean size, dispersion and growth velocity.

Temperature Effects, global model and Population Balance Comparison: This second set of experiments has been used to study the temperature effect, to compare the FPE with the population balances and to validate a global model.

Running Time [h]	Antisolvent (PI)	Feedrate [ml/min]	Temperature [°C]
8	Ethanol (4.3)	0.7	10
8		1.5	10
5		3.0	10
8		0.7	20
8		1.5	20
5		3.0	20
8		0.7	30
8		1.5	30
5		3.0	30

Table 4.2: Qualitative effects of increasing the antisolvent feedrate, temperature and using and antisolvent polarity index on the asymptotic mean size, dispersion and growth velocity.

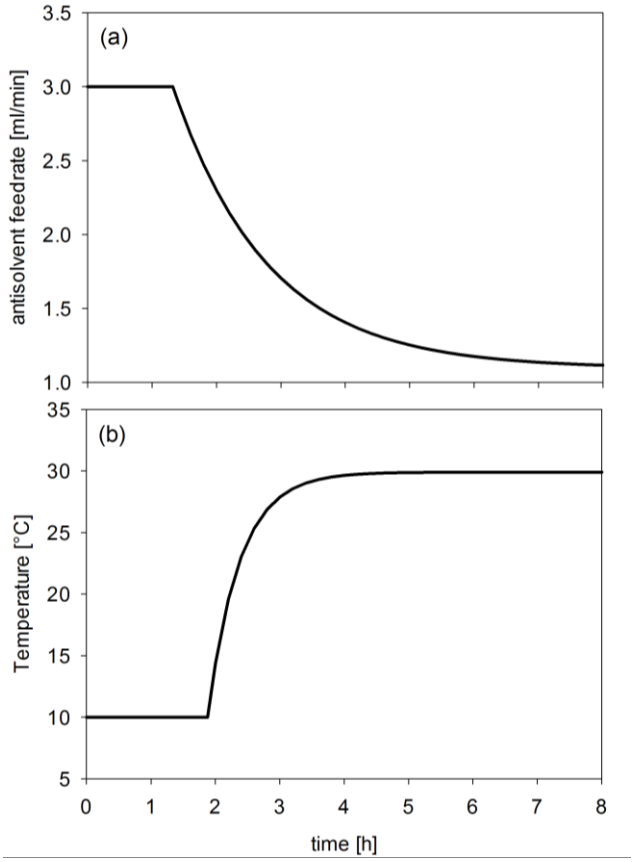

Figure 4.10: Qualitative effects of increasing the antisolvent feedrate, temperature and using and antisolvent polarity index on the asymptotic mean size, dispersion and growth velocity.

In order to investigate the multiplicity of the asymptotic conditions, with different operating condition, an experimental run obtained from the global map has been calculated in which the mean and the variance are the same of the ones using an antisolvent feedrate equal to 3.0 and a constant temperature of 30 °C.

Global model and operability map: In order to identify the multiplicity of the steady state condition, obtained from the operability map, an experimental run with the same asymptotic mean size and variance

obtained at 3.0 ml/min and 30 °C has been conducted in the following conditions, below in the Table 4.3.

Running Time [h]	Antisolvent (PI)	Feedrate [ml/min]	Temperature [°C]
6	Ethanol (4.3)	2.25	20

Table 4.3: Qualitative effects of increasing the antisolvent feedrate, temperature and using and antisolvent polarity index on the asymptotic mean size, dispersion and growth velocity.

Polarity Influence: The polarity influence has been investigated performing two set of experimental runs, one using constant operating conditions, such as temperature and antisolvent feedrate, using different antisolvents with different polarities (Table 4.4). Then a second set of experimental runs has been conducted to proof the hypothesis made about the hydrogen bond influence, in which the experiments have been performed in order to obtain the highest supersaturation and the lowest supersaturation, using the most and the least polar antisolvent in both extreme operability conditions. Both conditions have been compared with the results obtained in the same conditions, using and middle-polar antisolvent (Table 4.5).

Running Time [h]	Antisolvent (PI)	Feedrate [ml/min]	Temperature [°C]
8	Acetic Acid (4.8)	1.5	20
8	Ethanol (4.3)	1.5	20
8	Isopropanol (3.9)	1.5	20

Table 4.4: Qualitative effects of increasing the antisolvent feedrate, temperature and using and antisolvent polarity index on the asymptotic mean size, dispersion and growth velocity.

Running Time [h]	Antisolvent (PI)	Feedrate [ml/min]	Temperature [°C]
4	Acetic Acid (4.8)	3.0	10
5	Ethanol (4.3)	3.0	10
8	Isopropanol (3.9)	0.7	30
8	Ethanol (4.3)	0.7	30

Table 4.5: Qualitative effects of increasing the antisolvent feedrate, temperature and using and antisolvent polarity index on the asymptotic mean size, dispersion and growth velocity.

Chapter 5

Results and discussions

This chapter will show all the results obtained for all the mathematical models studied, and then validated with the experiments conducted ad hoc. There will be also some a posteriori modeling obtained observing the experimental behavior, leading to obtain a mathematical correlation between Fokker-Planck Equation, FPE, and parameters, considering the operating conditions, allowing then to generate an asymptotic map of all the possible mean sizes and variances of the CSD allowable within the operating conditions window considered. The FPE has been also compared with the most known Population Balances PBM, showing an excellent performance, both concerning the qualitative description of the CSD and quantitative, obtaining a more suitable model for control and optimization purposed, despite of the more complex PBMs. The Chapter ends with an hypothesized mechanism concerning a close relationship between the hydrogen bond strength and the supersaturation of the system. The hypothesized mechanism has been confirmed with proper experimental runs.

The experimental results are schematically focused on:

- The modeling of the FPE with the proper noise intensity, allowing an accurate description of the Crystal Size Distribution, CSD, evolution;

- A simplified FPE model that leads to an analytical solution with a separate description of the time evolution of the mean size of CSD and its variance;
- A global model that allows to model the CSD evolution considering the temperature and the antisolvent federate, with and explicit depency of the FPE parameters;
- A comparison between the FPE and a Population Balance Model, PBM, in nonisothermal conditions;
- An asymptotic representation of the operating conditions as a function of the manipulated variables;
- An hypothesized mechanism concerning influence of the hydrogen bond on the nonisothermal antisolvent crystallization processes, considering different solvents with different polarity indexes.

5.1 The Fokker-Planck Equation

The general linear FPE modeled in Chapter 3 (3.16), is represented with two important terms: a deterministic term, able to dynamically follow the mean of the resulting Probabilistic Density Function, CSD, and a diffusivity term that allows the CSD to change dynamically its width and shape, accordingly to the noise intensity chosen. The first logical step is to find out the proper noise intensity to fit the CSDs. In Chapter 3 has been shown the noise intensity as a function of a parameter α (3.12), where in the particular case, for a pure random process, an analytical solution can be performed, obtaining as a result a set of CSD in which, comparing with shape of the experimental CSDs (Figure 4.8), the best set of parameters to analyze are for α equal to 0, 0.5, 1.0 and 1.5, all of them allow to obtain a long-tailed CSD, as reported again in Figure 5.1, in stationary state.

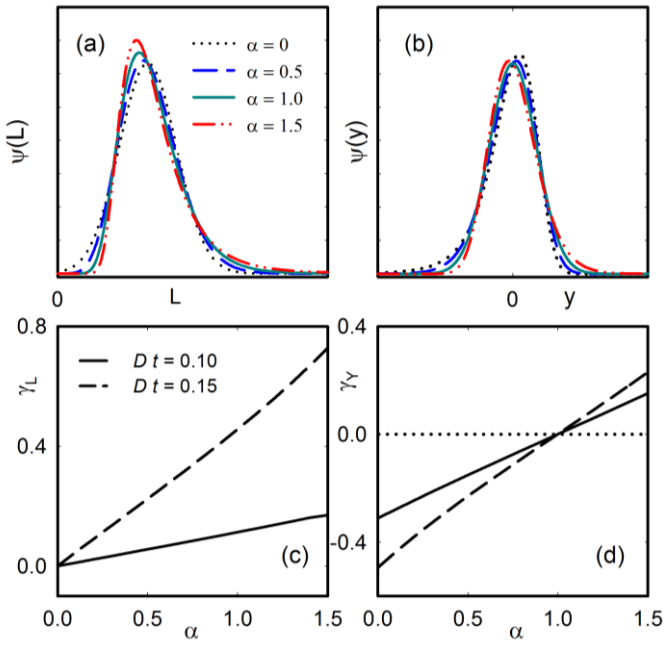

Figure 5.1: CSD for a purely random process ($Dt = 0.1$) in the (a) logarithmic scale and (b) linear scale, for $\alpha = 0$ (dotted line), $\alpha = 0.5$ (blue dashed line), $\alpha = 1$ (green solid line), $\alpha = 1.5$ red (dashed-dotted line). The skewness of the CSD with respect to α is also reported for the logarithmic scale (panel c) and the linear scale (panel d) for $Dt = 0.1$ (solid line) and $Dt = 0.15$ (dashed line).

The second step was the choice of a proper deterministic model, a simple model, able to describe the evolution in time of the mean size of crystals, with an asymptotic plateau (Figure 3.2). Considering the experimental behavior, the choice ended up with a simple logistic model expressed by the Equation 3.34.
The FPE model is then represented by three parameters and in order to fit the experimental data, and thus find the best FPE model, all the four values of α has been considered.

Parameter Estimation: Model calibration for the estimation of parameters is carried out separately for every run. The experimental CSD ψ_{exp} is numerically evaluated through Equation 5.1 at N = 50

different spatial locations y_k (when $k = 1, \ldots, N$) at each sampling time t_j ($j = 1, \ldots M$). The parameters to be estimated are: $\theta = [\log_{10}(D), r, K]$ (log (D) is used instead of D in order to reduce the statistic correlation between the parameters). Parameter inference is accomplished by using the least square criterion, thus searching the minimum of the objective function:

$$\Phi(\theta) = \Phi(r,K,D) = \sum_{j=1}^{M}\sum_{k=1}^{N}\left(\psi_{\mathrm{mod}}(y_k,t_j;\theta) - \psi_{\exp}(y_k,t_j)\right)^2 \qquad (5.1)$$

In Equation 5.1, $\psi_{mod}(y_k,t_j)$ is the probability density function evaluated through numerical integration of Equations 3.27, 3.29, 3.31 and 3.33 (corresponding to the appropriate model selected), at time t_j and size coordinate y_k, while the distribution $\psi_{exp}(y_k,t_j)$ is the experimental observation of the CSD evaluated at the size coordinate y_k at time t_i.
The point estimation values for the model parameters, together with the related Mean Square Errors s^2 are reported in Table 5.1.

	Feed Flow	r	K	log(D)	s^2
$\alpha=0$	LFR	$7.46\ 10^{-2}$	7.200	1.169	$5.9\ 10^{-2}$
	MFR	$3.56\ 10^{-2}$	7.993	1.134	$2.5\ 10^{-2}$
	HFR	$6.42\ 10^{-2}$	8.530	1.328	$5.3\ 10^{-2}$
$\alpha=0.5$	LFR	0.914	4.863	0.952	$4.0\ 10^{-3}$
	MFR	1.038	4.691	1.025	$2.5\ 10^{-3}$
	HFR	1.241	4.661	1.026	$4.8\ 10^{-3}$
$\alpha=1$	LFR	1.254	4.840	-0.952	$3.9\ 10^{-3}$
	MFR	1.354	4.683	-0.859	$2.5\ 10^{-3}$
	HFR	1.902	4.635	-0.749	$4.4\ 10^{-3}$
$\alpha=1.5$	LFR	1.845	4.821	-2.840	$9.5\ 10^{-3}$
	MFR	1.765	4.679	-2.756	$6.6\ 10^{-3}$
	HFR	1.725	4.652	-2.777	$1.0\ 10^{-2}$

Table 5.1: Point estimation of the parameters for the different operating conditions for the four models investigated.

The performance of the model calibration is carried out by evaluating the Mean Square Error s^2 here defined as:

$$s^2 = \frac{\sum_{j=1}^{m}\sum_{k=1}^{n}\left(\psi_{\mathrm{mod}}\left(y_k, t_j; \hat{\theta}\right) - \psi_{\exp}\left(y_k, t_j\right)\right)^2}{m \cdot n} = \frac{\Phi\left(\hat{\theta}\right)}{m \cdot n} \tag{5.2}$$

In Equation 5.2, $\hat{\theta}$ is the vector of parameter values that minimize the objective function.

From the analysis of the results reported in Table 5.1, it is possible to notice that the s^2 values related to the models with $\alpha = 1$ and $\alpha = 0.5$ are lower than the ones observed with the other two models and this feature is observed for each run. This indicates that a diffusion term that depends on y for the stochastic component of the model provides the best fit to the experimental data. Furthermore, indicates that the GBM assumption is better suited to represent the crystal growth process, thus confirming the results previously obtained in the literature for different experimental fixtures and data acquisition procedures [Grosso et al, 2010]. In addition, the parameter values for the LBM are very different, depending on the diffusive term: the pseudo-diffusivity value D, and the K asymptotic equilibrium value are much higher in the LBM model. This result was unexpected since the diffusive term is supposed to mainly affect the shape of the probability distribution while the deterministic part should be less influenced. It was instead found that a significant dependence of the parameter estimation on the diffusive term is appreciable. The parameter inference is further analyzed by exploiting typical tools of the statistical inference. In more detail, the parameter confidence intervals, the asymptotic correlation matrix for the parameters and the parameter joint confidence regions has been addressed. Mathematical details for their determination can be found elsewhere [Fa, 2005; Tsoularis and Wallace, 2002]. For sake of space the statistical analysis is reported only for $\alpha = 1$. Table 5.2 reports the asymptotic correlation matrix estimated for the three experimental runs. The parameters are not significantly correlated, thus revealing that ill-conditioning in the parameter inference is prevented, at least for the current experiments. As a further remark, the correlation among the parameter pairs is qualitatively the same, especially for the LFR and MFR runs.

		log(*D*)	*r*	*K*
LFR	log(*D*)	1	0.5980	0.3384
	r		1	0.6619
	K			1
MFR	log(*D*)	1	0.5818	0.3250
	r		1	0.6541
	K			1
HFR	log(*D*)	1	0.4911	0.2429
	r		1	0.6158
	K			1

Table 5.2: Asymptotic correlation matrix of the parameters for the FPE-GBM model.

The linear approximations of the confidence intervals are reported in Table 5.3, whereas the joint confidence regions in the parameter space are shown in Figure 5.2. As it regards the latter analysis, since we have three parameters to be estimated, the confidence regions will lie in a 3D parameter space and they will be defined by three different confidence ellipsoids (for the three different runs). As a first comment, it should be noted that both of the confidence intervals and regions are relatively small, meaning that the parameters are estimated with a small uncertainty. In addition, they do not assume negative values, thus meaning that all of them are statistically significant in the model. In addition, the confidence regions for the three different runs are clearly distinct, thus suggesting that the influence of the feeding rate on the parameters variation is significant also from a statistical point of view.

Feed Flow	*r*	*K*	log(*D*)
LFR	1.221÷1.287	4.793÷4.887	-0.975÷-0.930
MFR	1.327÷1.380	4.648÷4.719	-0.877÷-0.840
HFR	1.860÷1.944	4.587÷4.684	-0.774÷-0.723

Table 5.3: Parameters confidence interval for the FPE-GBM model.

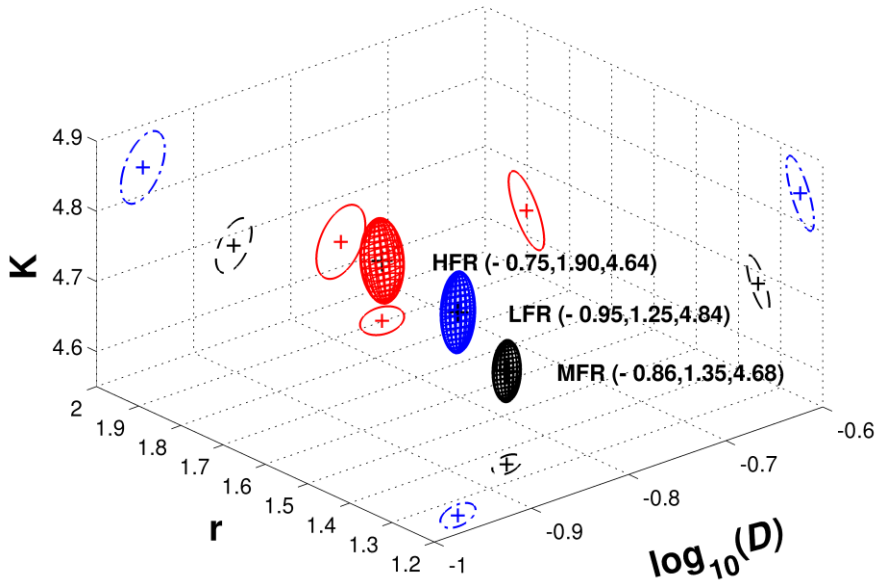

Figure 5.2: Confidence ellipsoids for the parameter estimation for the different feed conditions (blue: LFR; black: MFR; red: HFR) and their projections on the three different planes. LFR: solid line; MFR: dashed-dotted line; HFR: dashed line.

Model Comparison: Figures 5.3 and 5.4 illustrate (respectively in the logarithmic and linear scale) the comparison between the predicted particle size distribution using the alternative models for the end of the batch and for MFR.

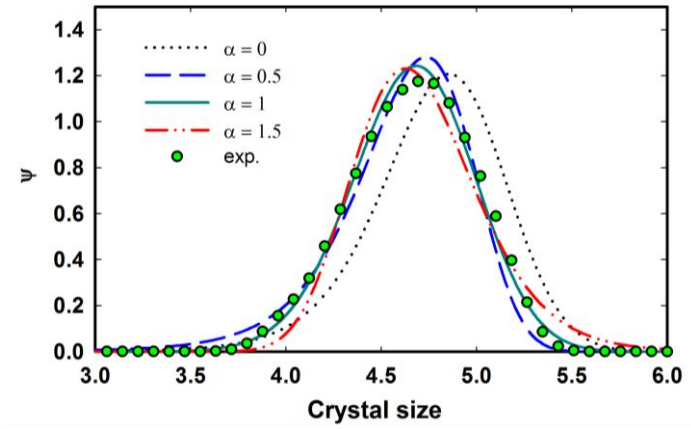

Figure 5.3: Comparison between experimental probability density functions (green points) and model predictions (black dotted line: $\alpha = 0$; blue dashed line: $\alpha = 0.5$; green solid line: $\alpha = 1$; red dash-dotted line: $\alpha = 1.5$) for MFR (logarithmic scale).

In order to compare the CSD predicted by FPE with the one resulting from PBE, they should be evaluated with the same scale. One should be reminded that the nonlinear transformation adopted in the FPE approach is $L = g(y) = \exp(y)$, and one can recover the probability density function in the linear scale by applying the proper inverse nonlinear transformation. From basic definitions of probability theory, one can easily demonstrate that Equation 5.3 eventually gives the CSD, in the linear scale:

$$\Psi_L(L,t) = \frac{1}{\left.\frac{dg}{dy}\right|_{y=g^{-1}(L)}} \Psi_y\left(y = g^{-1}(L), t\right) = \frac{1}{L}\Psi_y\left(\ln(L), t\right) \tag{5.3}$$

where the transformation $y = g^{-1}(L) = \ln L$ has been considered for the case at hand.

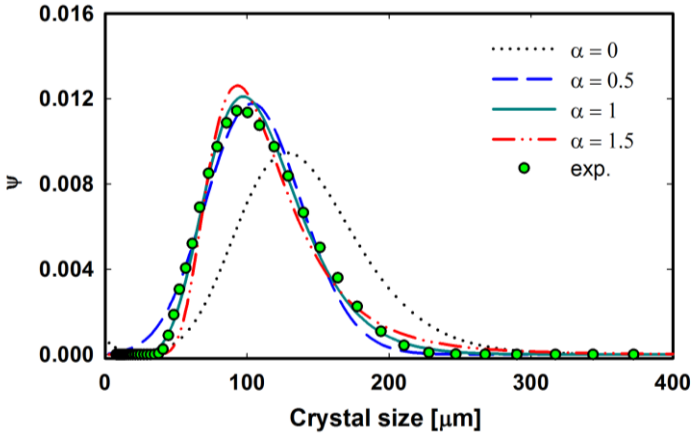

Figure 5.4: Comparison between experimental probability density functions (green points) and model predictions (black dotted line: α = 0; blue dashed line: α = 0.5; green solid line: α = 1; red dash-dotted line: α = 1.5) for MFR (linear scale).

It is clear from the figures that the use of α = 1 (GBM) in the stochastic component is more appropriate to describe the CSD of the crystallization process. The differences on the predictive features of the models are even more evident in the normal scale. More insight into the descriptive characteristics of the alternative models can be obtained by analyzing the time evolution of the experimental observations and the corresponding model prediction for first moments of the distribution, i.e., the mean, μ and the variance σ^2, evaluated in the linear scale:

$$\mu_L(t) = \int_{-\infty}^{+\infty} L\,\psi(L,t)dL = \exp\left(\mu_y(t) + \frac{\sigma_y^2(t)}{2}\right) \tag{5.4a}$$

$$\sigma_L^2(t) = \int_{-\infty}^{+\infty} (L-\mu_L(t))^2\,\psi(L,t)dL = \exp\left(2\mu_y(t)+\sigma_y^2(t)\right)\left(e^{\sigma_y^2(t)}-1\right) \tag{5.4b}$$

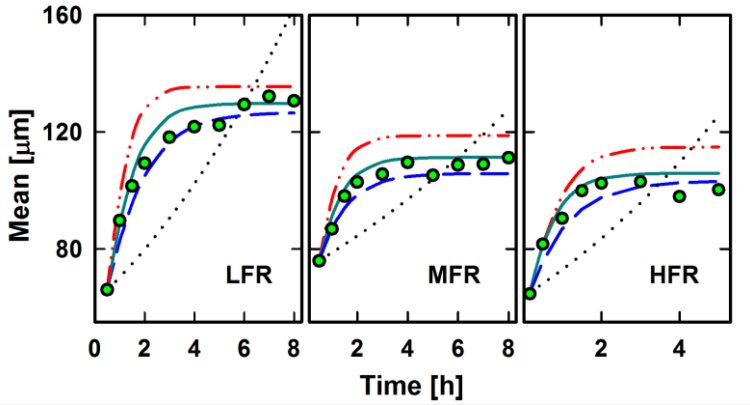

Figure 5.5: Mean of the Crystal Size Distributions for the three feeding rates and for the different models (black dotted line: $\alpha = 0$; blue dashed line: $\alpha = 0.5$; green solid line: $\alpha = 1$; red dash-dotted line: $\alpha = 1.5$). Green points are the experimental observations (linear scale).

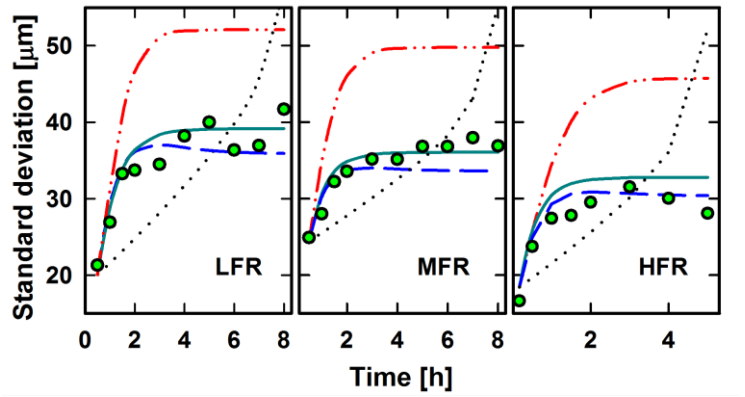

Figure 5.6: Standard deviation of the Crystal Size Distributions for the three feeding rates and for the different models (black dotted line: $\alpha = 0$; blue dashed line: $\alpha = 0.5$; green solid line: $\alpha = 1$; red dash-dotted line: $\alpha = 1.5$). Green points are the experimental observations (linear scale).

Figures 5.5 and 5.6 show, respectively, the mean and variance experimentally observed (circle points) compared with the theoretical predictions (dotted line $\alpha = 0$, dashed line $\alpha = 0.5$; solid line $\alpha = 1$ and dotted-dashed line $\alpha = 1.5$) for the three runs and for

the four models as a function of time. The agreement again is excellent at each time using $\alpha = 1$ in the stochastic component and the FPE model, driven by its deterministic part (the logistic growth term), correctly describes the increasing trend of the average crystal growth. On the other hand, the performance of the model deteriorates when using the alternative models both in terms of the mean and variance predictions. It is remarkable that the dynamic behavior of the LBM model is quite different: while GBM and intermediate case models almost reach the asymptotic equilibrium value at the final time of the experimental run, conversely, the LBM model seems to be far from the equilibrium solution, and this feature is clearly in contrast with the experimental evidence and the physical situation. This is also in agreement with the findings reported by [Bates and Watts, 2006], in terms that the lognormal CSDs can be generated mathematically by the Law of Proportionate Effect (LPE) which states that the rate of growth is proportional to linear size times a random number, thereby making growth rate size-dependent.

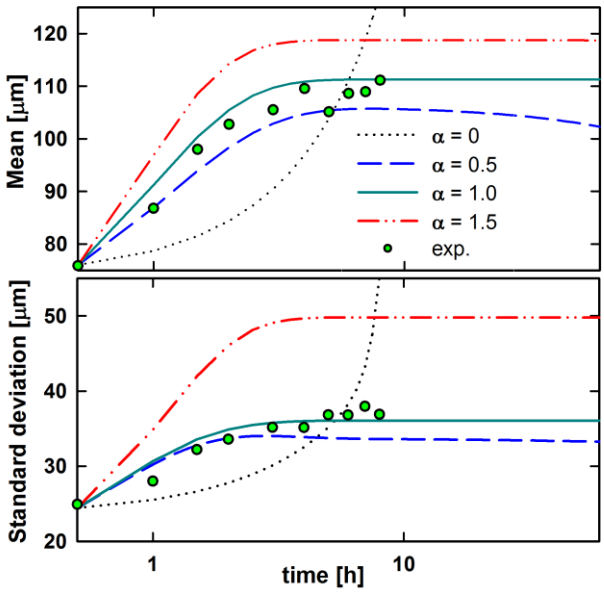

Figure 5.7: Long time behavior: mean and standard deviation behavior comparison among the models for MFR.

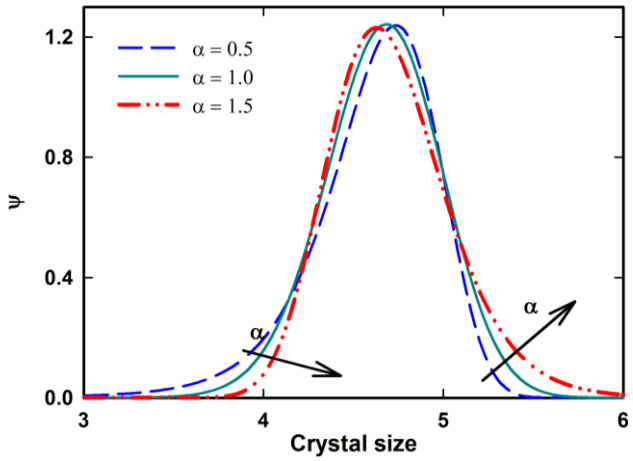

Figure 5.8: Steady state CSD computed for α = 0.5 (blue dashed line), 1 (green solid line) and 1.5 (red dashed-dotted line) for MFR (linear scale).

As a further analysis for the model comparison, the time evolution of the mean and the variance of the crystal size distributions are reported for the four models, in Figure 5.7, over a time window much larger than the one used for the experiments. The purpose of the analysis is to appreciate the long-time dynamics and check their extrapolation capabilities to reasonably describe the asymptotic behavior. The four models are integrated at the parameter values inferred by the parameter estimation at MFR. For sake of completeness, also the experimental values are reported. Keeping in mind that the r parameter gives a measurement of the characteristic process time, it is clear that the transient time in the LBM model (the order of magnitude is $\tau = 1/r \sim 25\ h$) is clearly overestimated with respect to the one obtained with the GBM model (where $\tau = 1/r \sim 1.0\ h$). The latter characteristic time is more likely to depict the experimental evidence of the process under consideration. As a final remark, for these parameter conditions, the steady state regime is experimentally reached after a rather short transient ($\sim 4\ h$).
It could be also observed that in the case of α equal to 0.5 the mean shows an implausible decrease for high time values thus confirming that the GBM ($\alpha = 1$) is the more appropriate model to describe the crystal growth. It is worth stressing out that by considering different

noise models it is possible to shape the computed CSD, compare Figure 5.8, where the steady state solution of the models for MFR and α equal to 0.5, 1 and 1.5 are reported, with Figure 5.1 (and 3.1). The curve for α equal to 0 was not reported since not steady state solution was obtained after 60 hours of simulation. One should remark that, on the contrary of the purely stochastic cases Equation 3.30, a not trivial asymptotic solution is eventually reached. This feature follows from the competition between two different effects: the stochastic term, which tends to indefinitely spread the CSD, and the deterministic attractive contribution which drives the random variable towards the deterministic equilibrium value *K*. This interplay between the two terms produces some distortion as could be evidenced by computing the skewness of the CSDs (here evaluated in the logarithmic scale) for the different cases as reported in Table 5.4. When $\alpha = 1$, it is found that the skewness assumes the value of $\gamma = -0.15$ very close to the experimental one, equal to -0.20.

	α = 0.5	**α = 1.0**	**α = 1.5**	**Exp.**
γ_y	+0.245	-0.147	+0.637	-0.200

Table 5.4: Skewness evaluations, for the asymptotic CSD predicted by models 3.29, 3.31 and 3.33 for MFR, compared with the experimental value evaluated at the final time.

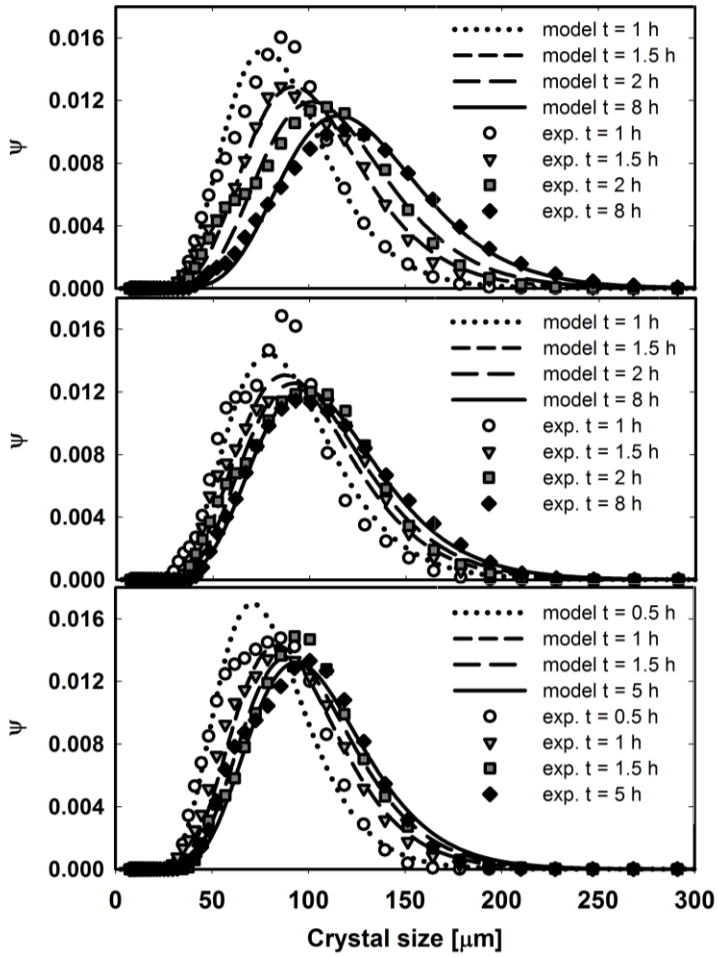

Figure 5.9: Comparison between model (α = 1) and the experimental Particle size distributions at different times for the three antisolvent feed-rates. Operating conditions: (a) LFR; (b) MFR: (c) HFR.

Finally, Figure 5.9 reports the comparison (in terms of time evolution) of the CSD experimentally observed and the model prediction (using the FPE-GBM model) for the experiment at low, medium and high feed rates, at the first and final acquisition time. It is evident that there is an excellent quantitative agreement between experiments and the predictions from the phenomenological model. In particular, the model is able to correctly capture the long-tailed

asymmetric shape of the experimental CSD as well as follow the dynamic of the crystal growth for a range of operating conditions.

5.2 Maximum Likelihood Optimization and Analytical Solution of the FPE

Following the procedure previously outlined, the calibration of the proposed models is again carried out separately for every run. The set of parameters $\theta = [log_{10}(D), r, K]$ is inferred this time using the Maximum Likelihood Estimation Method (ML). In the Least Squares (LS) approach, the model parameters are estimated searching the minimum of the objective function given by the distance between the theoretical CSD $\Psi(y,t,;\theta)$ carried out from numerical integration of the model and the experimental CSDs processed through a kernel basis function (4.3).
Conversely, the Maximum Likelihood (ML) estimation approach, aims to determine the θ values that maximize the probability (likelihood) directly from the sample data measurements. Therefore, the parameters are inferred by searching the maximum of the log-likelihood function:

$$\log L\left(y_i,t_j;\theta\right) = \sum_{j=1}^{m}\sum_{i=1}^{n_j} \log\left(\Psi\left(y_i,t_j;\theta\right)\right) \tag{5.5}$$

The Maximum Likelihood estimation through equation 5.5 is possible only if the crystal observations can be assumed to be independent, that seems a reasonable hypothesis. The ML has been already used to infer the parameters related to the process steady state [Tronci et al, 2011] and it is demonstrated to give more efficient parameter estimation, that is, a minor number of experimental data are required to carry out an effective evaluation of the parameters, at least compared with the LS method. Indeed, since it achieves the Cramér-Rao lower bound, no asymptotically unbiased estimator has lower asymptotic mean squared error than the ML [Papoulis, 1991]. In addition, the introduction of possible

errors in the evaluation of the experimental distribution (based on Equation 4.3) is in this way circumvented. Thus, the onerous step in the experimental activity represented by the data acquisition through visual inspection can be eventually reduced.

Another factor that has been considered is the nonlinearity of the linear FPE coefficients. In order to obtain a simplified model, able to lead an analytical solution, the deterministic term has been reformulated as a Gompertz model 3.36.

LG-LS	Logistic model with parameters estimated through Least Square Method
LG-ML	Logistic model with parameters estimated through Maximum Likelihood Estimation
GZ-ML	Gompertz model with parameters estimated through Maximum Likelihood Estimation

Table 5.11: Acronyms of different models and parameter estimation methods used

In order to address a methodical analysis, the LG model will be calibrated and compared via both LS and ML algorithms. Table 5.11 summarizes the acronyms hereafter used to refer to the model and the model calibration procedure.

	LG-LS		
	LFR	**MFR**	**HFR**
r	1.254	1.354	1.902
K	4.840	4.683	4.635
D	0.112	0.138	0.178

	LG-ML		
	LFR	**MFR**	**HFR**
r	1.474	1.755	1.922
K	4.786	4.635	4.607
D	0.125	0.176	0.147

	GZ-ML		
	LFR	**MFR**	**HFR**
v	4.720	5.180	8.659
K	4.795	4.631	4.585
D	0.088	0.106	0.156

Table 5.12: Inferred model parameters.

Table 5.12 reports the results obtained for LG-LS previously discussed, together with the LG-ML and the GZ-ML, for the different antisolvent feedrate values. It should be noted that the data estimation, using both methodologies, leads to slight differences among parameter values. In particular, small difference could be observed for the growth rate parameter *r* and for the pseudo-diffusivity coefficient *D*. The slight discrepancies can be also due to the introduction of the kernel basis function approximation in the LG-LS. On the other hand, the *K* parameter, representing the asymptotic value of the mean size of crystals in logarithmic scale, appears more robust to the approximation. The parameters show small difference between the GZ-ML and the LG-ML, except for the growth rate parameters *r* and *v*. This disagreement can be explained by observing that the growth rate for the GZ model is related defined as: $v = rln(L_0) = rln(K)$.

	LFR	**MFR**	**HFR**
LG-ML	620.28	959.20	266.64
GZ-ML	674.27	1081.08	298.86

Table 5.13: AIC (Akaike's Information Criterion) for LG-ML and GZ-ML models.

Table 5.13 reports the Akaike Information Criterion (AIC) for both models studied, which gives a measure of the relative goodness of fit of a statistical model [Akaike, 1974]. It is apparent that the differences in terms of AIC criterion are relatively small, although the GZ-ML model is limited to describe only symmetric distributions. This result is encouraging for the development and the application of the GZ-ML model in the case of the optimization and the control of the crystallization system.

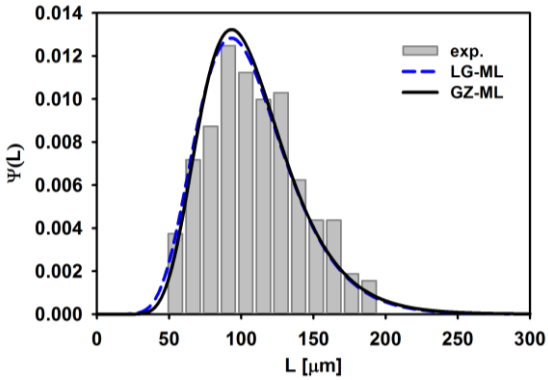

Figure 5.10: CSD comparison, in linear scale, for the MFR at the end of the experimental run: LG-ML model (dashed blue line); GZ-ML model (solid black line) and experimental CSD (vertical bars).

Figure 5.10 shows the obtained CSD, at the final time (end of the run) and at the medium feedrate (MFR) condition, for both LG-ML and GZ-ML. It is possible noticing that both models rather well describe the experimental distribution but with small difference mainly observed in edges of the distributions.

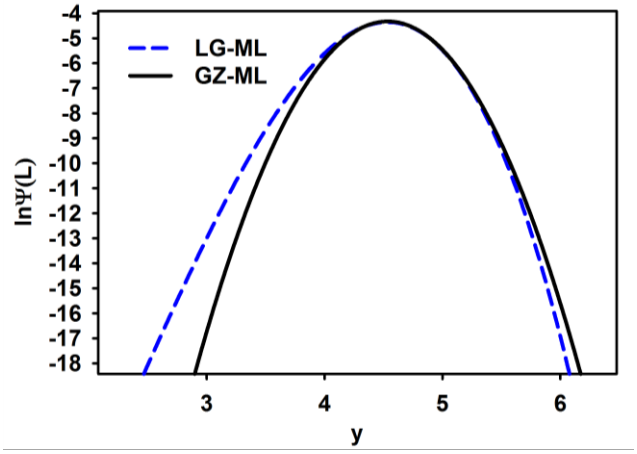

Figure 5.11: CSD comparison, in log-log scale: LG-ML (dashed blue line); GZ-ML (solid black line).

To better represent this aspect, the same distributions are represented in a log-log scale in Figure 5.11, where it is possible to appreciate the differences between the two distributions.
A further comparison between the two models can be accomplished by evaluating the distribution skewness for the predicted CSD, at the final time for all the operating conditions, whose values are reported in Table 5.14.

	Experimental	**LG-LS**	**GZ-LS**
LFR	-0.299	-0.128	0
MFR	-0.200	-0.147	0
HFR	-0.403	-0.139	0

Table 5.14: Skewness of the CSD in logarithmic scale at the end of run for the three operability conditions.

The skewness values for the GZ-ML are obviously equal to zero, since FPE with linear drift term preserves the Gaussianity introduced with the initial CSD. On the other hand, experimental observations (when regarded in the logarithmic scale) seem to suggest that some negative skewness in the data sample is always present, and this feature is correctly captured by LG-ML. Nevertheless, the quantitative agreement between GZ-LM model and experiments is excellent.
A further test to appreciate the effectiveness of the GZ-ML approach is the comparison between the predicted CSD, by LG and GZ models (for both models the parameters were estimated through ML and they are given in Table 5.14, and the experimental histogram at four different sampling times for the MFR case, showed in Figure 5.12.

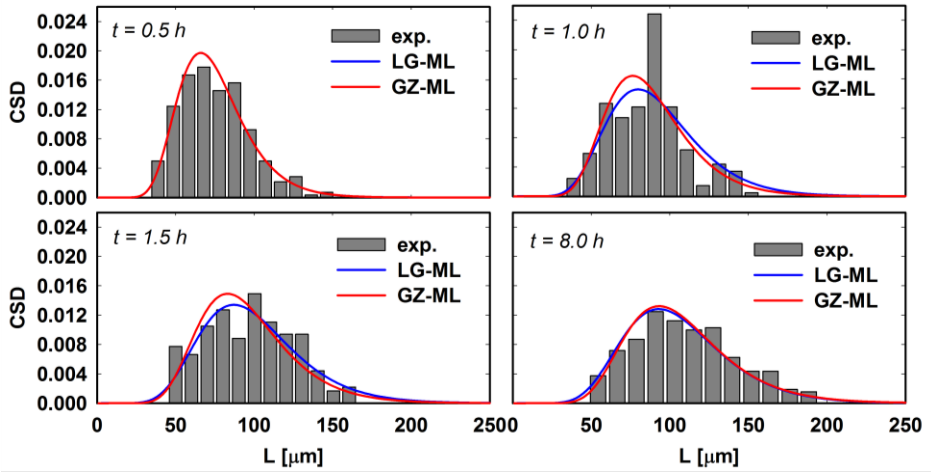

Figure 5.12: Transitory CSD comparison, in linear scale, for the MFR at different times {0.5 h, 1.0 h, 1.5 h, 8.0 h}: LG-ML (dashed blue line); GZ-ML (solid black line) and represent the experimental CSD (vertical bars).

The agreement between the experimental and the predicted CSDs are rather good with both models, the little difference is due by a zero value of the skewness parameter, that suggests the occurrence of some asymmetry in the CSD, but in the case studied this difference is imperceptible.

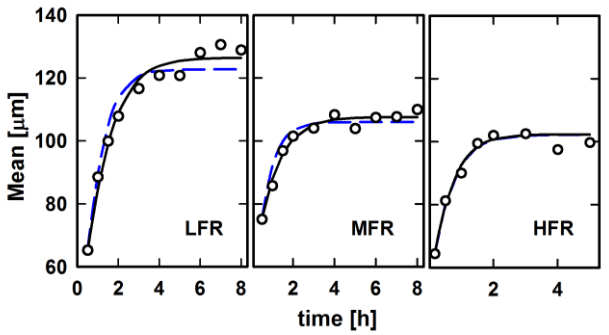

Figure 5.13: Linear mean size for LFR (a), MFR (b) and HFR (c): LG-ML (dashed blue line); GZ-ML (solid black line) and experimental values (white dots).

Figure 5.13 shows the mean size of crystals evaluated with the LG and GZ models together with the experimental observations. The capability of the two models in describing the mean size of crystals in time, for the each operating condition, is rather excellent; confirming that the proposed model is a valid alternative to the linear model with nonlinear coefficients.

5.3 Non Isothermal Global Model and Operating Maps

So far it has been discussed the modeling of the FPE equation considering three variables, not directly modeled as a function of the antisolvent feedrate. In this paragraph will be discussed the parameters of both models, FPE with nonlinear and linear coefficients, respectively called, from now, Model 1 and Model 2 and for the sake of simplicity, it has been considering three different isothermal conditions, using the three antisolvent feedrates used before for the isothermal case. First the parameters will be discussed without a direct functionality of both operating condition, and later will be discussed an empirical algebraic correlation, in order to formulate a global model, in order to be compared with the more used Population Balances PBM.

Parameters estimation for the FPEs describing the crystal growth for both nonlinear and linear models (Table 5.15) has been first carried out separately for every operating condition and then considering all the nine runs, in order to optimize the coefficients of the three algebraic relationships of temperature and antisolvent feedrate, for the three FPE parameters. The method used is the maximum likelihood method, introduced in the previous paragraph.
Table 5.15 reports the point estimations for the model parameters for both Model 1 and Model 2. The following behavior can be appreciated, which sounds from a physical point of view: (I) r_i increases with antisolvent feedrate and decreases with temperature; (II) K_i decreases with antisolvent feedrate and increases with

temperature and (III) D_i increases with antisolvent feedrate and decreases with temperature.

	Model 1			Model 2		
r	**10°C**	**20°C**	**30°C**	**10°C**	**20°C**	**30°C**
0.7 ml/min	1.0646	1.5700	0.7312	4.278	6.938	2.992
1.5 ml/min	1.9343	1.4029	1.1030	8.837	6.117	5.294
3.0 ml/min	3.2860	3.4428	1.9420	13.757	14.122	8.629
K	**10°C**	**20°C**	**30°C**	**10°C**	**20°C**	**30°C**
0.7 ml/min	4.9303	4.9501	5.0713	4.899	4.897	5.046
1.5 ml/min	4.8583	4.9298	5.0489	4.816	4.900	5.011
3.0 ml/min	4.7095	4.7656	4.8659	4.661	4.725	4.835
D	**10°C**	**20°C**	**30°C**	**10°C**	**20°C**	**30°C**
0.7 ml/min	0.1957	0.3992	0.1270	0.181	0.399	0.112
1.5 ml/min	0.3732	0.2163	0.1713	0.371	0.208	0.179
3.0 ml/min	0.7186	0.6735	0.2912	0.699	0.626	0.281

Table 5.15: Model parameters calculated at different operating conditions for logistic (Model 1) and linear (Model 2) crystal growth law.

In fact, increasing antisolvent feedrate leads to higher nucleation rates (*r* increases), but reduces the average asymptotic crystal size (*K* decreases). Temperature has an opposite effect as already discussed (Widenski et. al., 2012) in the non-isothermal antisolvent crystallization of sodium chloride (NaCl). Higher values of temperature, decreases *r* and reduces the driven force for nucleation and favors crystal growth (*K* increases). The operating conditions that favor nucleation determine a higher dispersion of the CSD, and this aspect has been correctly reconstructed by the behavior of coefficient *D*.

5.3.1 Stochastic Global Model

As previously discussed in the beginning of this paragraph, the proposed crystallization models based on FPE do not have an explicit dependency from operating conditions. Although effective results were obtained, the use of linear interpolation can be difficult

to use when a continuous input-output relationship is required, as in case of model-based control algorithms.
In this stage, the FPE is generalized in order to take into account an explicit dependence of the stochastic model parameters on input variables $m = (q, T)$

$$\frac{\partial \psi(y,t)}{\partial t} = D_i(m)\frac{\partial^2 \psi(y,t)}{\partial y^2} - \frac{\partial}{\partial y}\psi(y,t)\, g\left(y;\theta_i(m)\right) \qquad i = 1,2 \qquad (5.6)$$

The main goal is to find simple and parsimonious models that can describe the variation of the vector parameter θ_i with q and T, coherently with the behavior obtained for the point estimation reported in the previous section. From the inspection of the results in Table 2 and considering the experimental error, it is possible to hypothesize that the model parameters can have a nonlinear or weak nonlinear dependence on inputs. For the above considerations, the proposed input-parameter models are required satisfy the following conditions: (I) simple linear or quadratic dependences have been preferred to describe the input-parameter relationships and (II) the cross term dependence on T and q should be avoided. In spite of these simplifications, each parameter may depend on several combinations of T and q. thus leading to a number of alternative models. In this work, the following general expressions for the parameter dependencies have been considered:

$$\begin{aligned} r_i(q,T) &= \gamma_{i,0r} + \gamma_{i,1r} q^a + \gamma_{i,2r} T^b \\ K_i(q,T) &= \gamma_{i,0K} + \gamma_{i,1K} q^a + \gamma_{i,2K} T^b \qquad i = 1,2 \\ D_i(q,T) &= \gamma_{i,0D} + \gamma_{i,1D} q^a + \gamma_{i,2D} T^b \end{aligned} \qquad (5.7)$$

Where a and b can be equal to 1 or 2. In this way, the functions obtained to correlate the vectors θ_i with the manipulated variables q and T have nine parameters. The Γ vector of $\gamma_{i,uv}$ parameters (where u = 0, 1, 2 and $v = r, K, D$) have been again obtained by means of the a maximum likelihood estimation approach (cf. Eq. 5.5).
All the models have been considered with a linear or a quadratic dependency of the manipulated variables for simplicity, accordingly

to the sets of parameters obtained from the FPE fitting, from each experimental run (Figure 5.14). We have considered only the asymptotic dimension of crystals *K* with a quadratic behavior for both manipulated variable suggested by the parameters behavior shown in Figure 5.14.

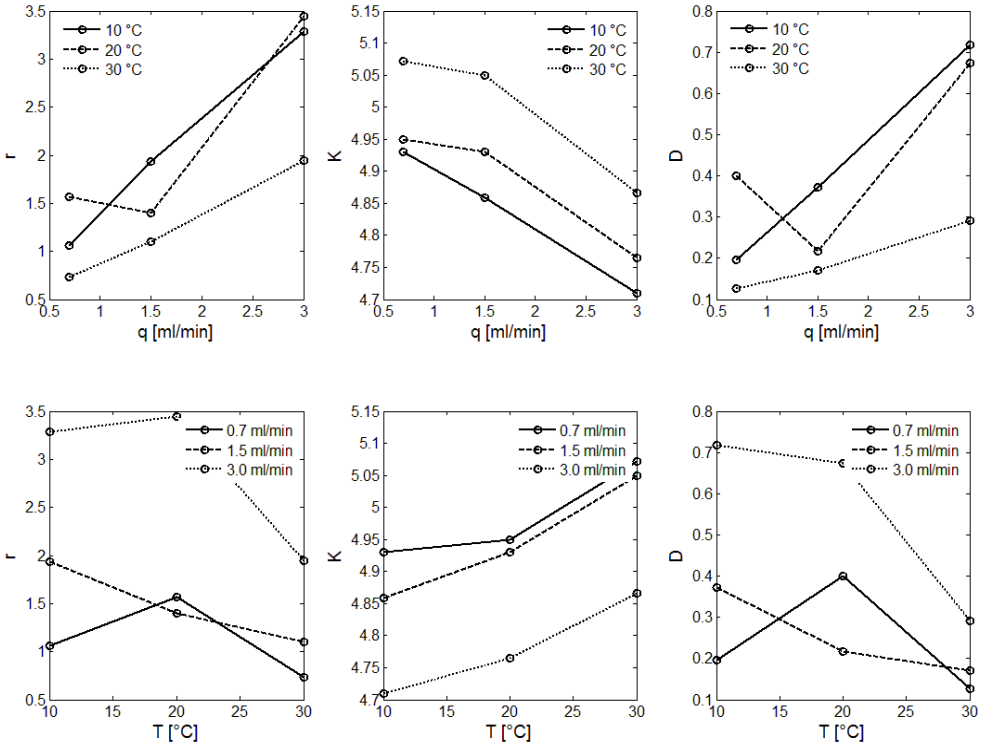

Figure 5.14: FPE parameters estimated from the single experimental runs at different temperatures and antisolvent feedrates. On the first row we have the iso-thermal curves and on the second row we have the data keeping constant the antisolvent feedrate.

Considering the three FPE parameters, *r*, *K* and *D*, all of them dependent from the two manipulated variables, and considering that the parameter *K* has been assumed with a quadratic dependency for both variables, we have a total combination of possible models equal to 16.

In order to choose which one is the best model we have considered the Akaike index AIC, for a quantitative evaluation of the maximum

likelihood fitting of each model and each set of exponents, and a qualitative, criterion based on the ability of the model to show a multiplicity of the asymptotic conditions, since not all the parameters follow the same functionality behavior with the two manipulated variables, allowing more than one solution for a specified operating condition.

Table 5.17 summarizes all the results obtained for each of the possible global model, in particular, we have included the AIC index for Model 1 and 2 with a side column in which is specified if the multiplicity of the asymptotic behavior is shown or not.

Test	**r**		**K**		**D**		**AIC**		
	q	***T***	***q***	***T***	***q***	***T***	**Model 1**	**Model 2**	***Multipl.***
1	1	1	2	2	2	2	10222.9	10422.1	No
2	1	2	2	2	2	2	10202.0	10427.6	No
3	**1**	**1**	**2**	**2**	**2**	**1**	**10213.4**	**10430.0**	**Yes**
4	1	2	2	2	2	1	10220.4	10439.7	Yes
5	1	1	2	2	1	2	10219.6	10440.8	Yes
6	1	2	2	2	1	2	10216.0	10446.0	No
7	1	1	2	2	1	1	10249.0	10448.5	No
8	2	1	2	2	2	2	10231.3	10450.8	Yes
9	2	2	2	2	2	2	10230.7	10455.2	No
10	2	1	2	2	2	1	10236.5	10457.9	No
11	1	2	2	2	1	1	10229.8	10461.2	No
12	2	1	2	2	1	2	10232.0	10468.4	Yes
13	2	2	2	2	2	1	10234.0	10469.1	No
14	2	2	2	2	1	2	10253.0	10471.1	No
15	2	1	2	2	1	1	10261.2	10473.5	No
16	2	2	2	2	1	1	10251.4	10483.5	No

Table 5.17: AIC for the considered models.

The model chosen with the minimum AIC value for both Model 1 and Model 2 is given by the following set of expressions:

$$
\begin{aligned}
r_i(q,T) &= \gamma_{i,0r} + \gamma_{i,1r} q + \gamma_{i,2r} T \\
K_i(q,T) &= \gamma_{i,0K} + \gamma_{i,1K} q^2 + \gamma_{i,2K} T^2 \qquad i = 1,2 \\
D_i(q,T) &= \gamma_{i,0D} + \gamma_{i,1D} q^2 + \gamma_{i,2D} T
\end{aligned}
\tag{5.8}
$$

The coefficients of expressions 5.8 are reported in Table 5.16, where it is possible to verify that the behavior shown by the parameter obtained performing the estimation for every operating condition are maintained by the proposed models. For example, the negative sign of $\gamma_{i,1K}$ is explainable with the fact that increasing antisolvent feedrate makes the asymptotic crystal size to decrease (high q values favor nucleation with respect to crystal growth). The same unfavorable effect of temperature on crystal growth rate (r_i) and dispersion (D_i) is correctly described being $\gamma_{i,2r}$ and $\gamma_{i,2D}$ negative.

Coefficient	Model 1	Model 2
$\gamma_{i,0r}$	0.5264	5.7639
$\gamma_{i,1r}$	0.5983	2.8342
$\gamma_{i,2r}$	$-6.4588\ 10^{-4}$	-0.1584
$\gamma_{i,0K}$	4.9176	4.8593
$\gamma_{i,1K}$	-0.0238	-0.0244
$\gamma_{i,2K}$	$1.7139\ 10^{-4}$	$2.0\ 10^{-4}$
$\gamma_{i,0D}$	0.2134	0.3864
$\gamma_{i,1D}$	0.0277	0.0287
$\gamma_{i,2D}$	-0.0019	-0.0094

Table 5.16: Values of the model parameters describing the dependence of (r, K, D) on antisolvent feedrate and temperature.

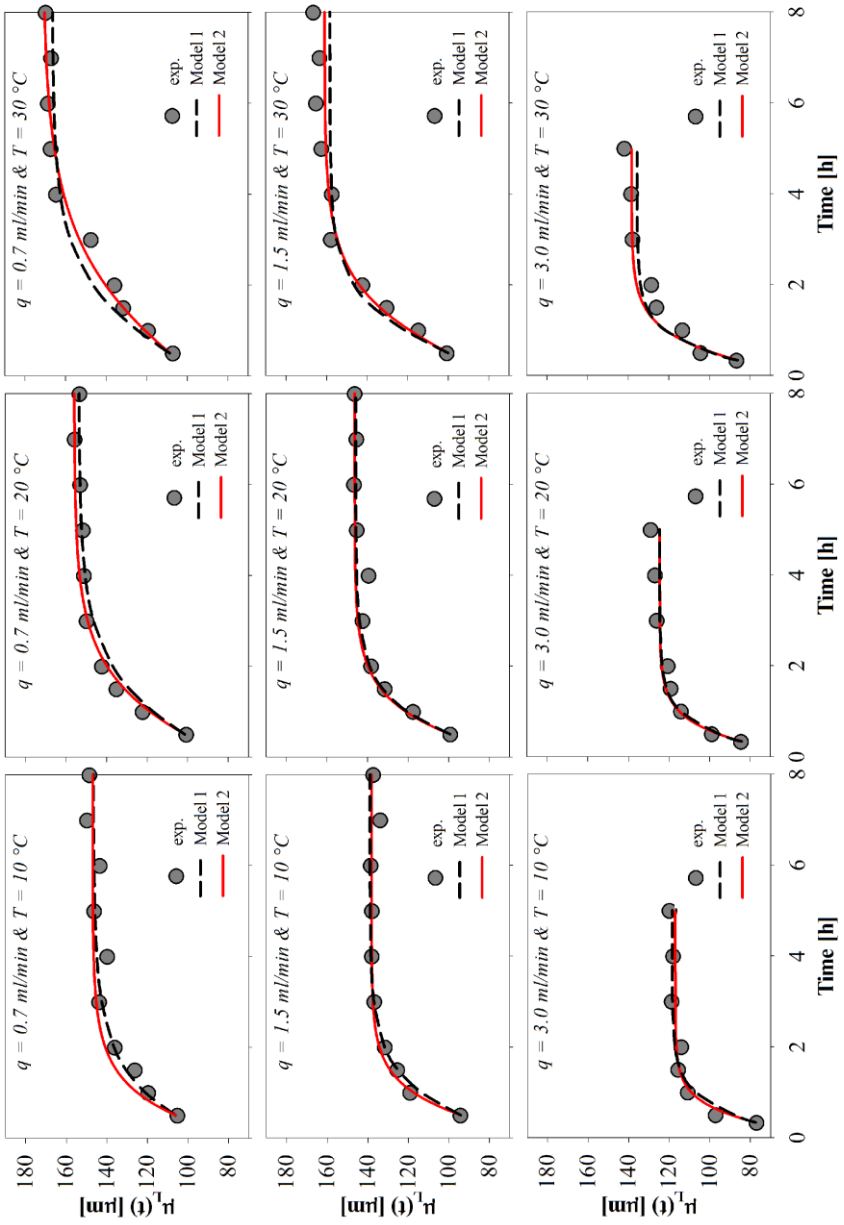

Figure 5.15: Mean size evolution of the nine experimental runs considered. The solid black line represents the Linear FPE, the dotted black line the non-linear FPE and the grey dots the experimental values.

The capability of the proposed global model to properly describe the crystallization system is shown in Figure 5.15, which reports the experimental mean crystal size behavior collected during the nine runs and the value calculated numerically using Model 1 (dotted line) and analytically for Model 2 (solid line). The match between calculated $\mu_L(t)$ and experimental values is excellent for both models, indicating that Equations 5.8 correctly approximate the input-parameter relationships.
The obtained global models have been also validated considering the antisolvent feedrate and temperature trajectory reported in Figure 5.16.

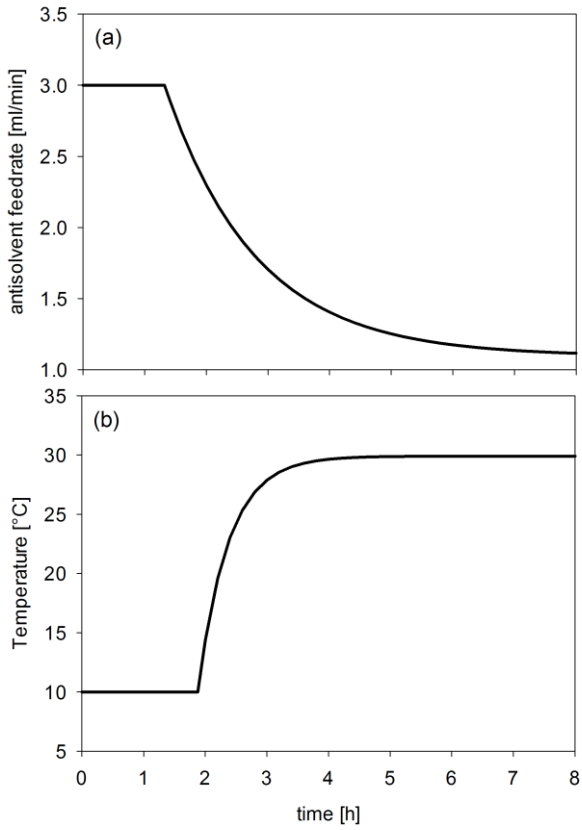

Figure 5.16: Antisolvent feedrate and temperature trajectory used for the validation run.

The results reported in Figure 5.17, indicates that the models again has excellent prediction capabilities, either with logistic (dotted line) or linear growth rate (solid line) during the nonisothermal operation of the system. The obtained models are again excellent predictors of the crystal size distribution as shown in Figure 5.17.

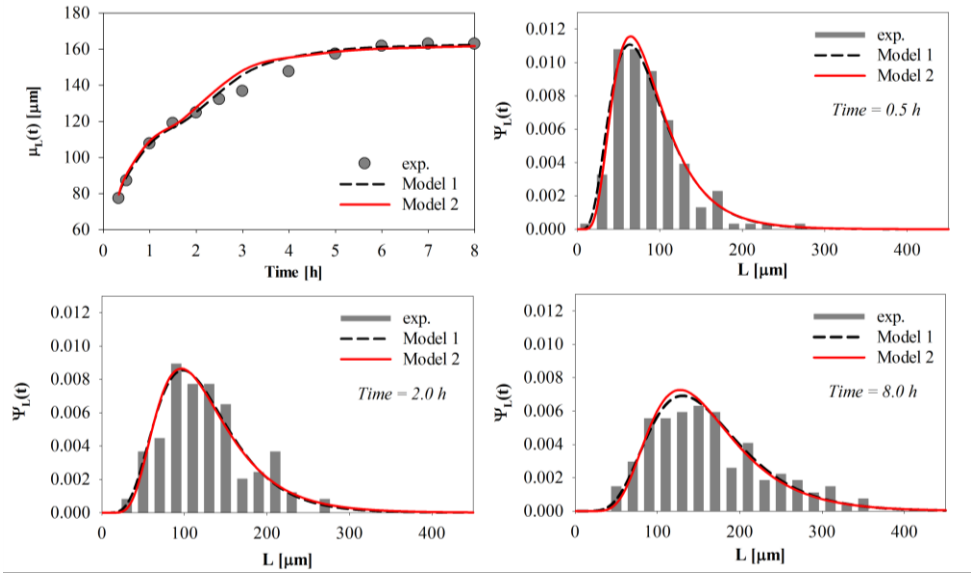

Figure 5.17: Validation results obtained in terms of mean sizes (top diagram) and CSDs (plots at the bottom). The results report the Model 1 and 2 compared with the experimental data.

It is worth noticing that the results obtained with linear and nonlinear growth rate are very close both considering the mean crystal size behavior and the CSD. This implies that assumption of linearity allows to a very good description of the considered system and could offer a more practical tool with respect to the nonlinear model, when model-based optimal controller wants to be developed.

5.3.2 PBM comparison

This section compares the global FPE obtained in the rigorous way with the more common Population Balances, in which the formulation is obtained from kinetic and thermodynamic

considerations. The paragraph introduces also the method used to obtain a numerical solution of the Population Balance Model, PBM.

Kinetic Parameter Estimation. The kinetic parameters were estimated using a maximum likelihood estimation procedure implemented with the gPROMS entity gEST. The nine experiments were combined for a single parameter estimation step. The crystallization size data samples can be reasonably approximated as coming from a log-normal distribution:

$$n(L,t) - \frac{n_0(t)}{\sqrt{2\pi}\sigma(t)L}\exp\left(-\frac{1}{2}\frac{(\ln L - \mu(t))^2}{\sigma(t)^2}\right) \tag{5.9}$$

In Equation (5.9) $\mu(t)$ is the log-normal mean and $\sigma(t)$ is the log-normal standard deviation, that are used to represent the crystal size distribution of the data. The Sauter mean size (D_{32}) was used as the representative mean size for the population balance approach:

$$D_{32}(t) = \frac{\mu_3}{\mu_2} = \frac{\int_0^\infty L^3 n(L,t)dL}{\int_0^\infty L^2 n(L,t)dL} \tag{5.10}$$

where $\mu_k(t) = \int_0^\infty L^k n(L,t)dL$ is, in general, the k-th moment of the CSD. The coefficient of variance (COV) was also used:

$$COV = \sqrt{\frac{\mu_4\mu_2}{\mu_3^2} - 1} \tag{5.11}$$

where μ_4, μ_3, and μ_2 are, respectively, the fourth, third, and second order moments of the crystal distribution. When dealing with log-normal distributions, the coefficient of variation can be straightforwardly related to the log-normal variance in the following way:

$$COV = \sqrt{\exp \sigma^2 - 1} \tag{5.12}$$

This allows for the comparison between the experimental data and the model-generated data for the parameter estimator solver. The generated optimum set of parameters is listed in the table:

b_0	$8.58 \cdot 10^{8}$	[#/m^4/s/°C]
b_1	$6.25 \cdot 10^{-3}$	[-]
g_0	$5.56 \cdot 10^{-4}$	[m/s]
g_1	$2.44 \cdot 10^{-4}$	[-]
g_2	12.33	[-]
g_3	$1.18 \cdot 10^{4}$	[J/mol]
g_4	0.374	[-]
g_5	1.053	[-]
g_6	1.733	[-]

Table 5.5: Birth and growth parameter of the PBE model estimated.

Table 5.5 lists the mean absolute deviation (MAD) of the mean size experimentally observed from the model prediction for each temperature and feed rate combination, where:

$$MAD = \frac{1}{N} \sum_{i=1}^{N} \left| x_{i,model} - x_{i,data} \right| \tag{5.13}$$

MAD			
	LT	***MT***	***HT***
LFR	8.23	8.89	15.94
MFR	6.27	4.19	7.46
HFR	12.37	3.67	7.78

Table 5.6: Mean absolute deviation of mean size.

Population Balance modeling by first principle assumption represents a rigorous way to describe the crystal growth dynamics and assess its definite relationships with the operating conditions. However, PBE modeling requires a clear connection of the

nucleation and growth phenomena from the driving force of the process that is the system supersaturation. Thus, a great deal of knowledge on the complex thermodynamics associated with the solute and solvent properties is needed.

Numerical Comparisons. Figure 5.18 reports (in linear scale) the comparison of the computed CSD with the two models and the available experimental data at different time for three of the nine temperature-antisolvent feedrate combinations: high temperature- and high feedrate; medium temperature-medium feedrate and low temperature-low feedrate. It is worth saying that analogous behaviour is observed for the other operating conditions. For sake of comparison the CSD evaluated through the PBE, Equation 3.1, has been normalized ($\psi(L,t)=n(L,t)/\mu_0$). The agreement between models and observations is rather remarkable, demonstrating that both the proposed models are able to quantitatively capture the shape of the CSD. This is further confirmed by the small values observed for the mean square error, MSE, for all the experimental conditions and for both the models, as reported in Table 5.6.

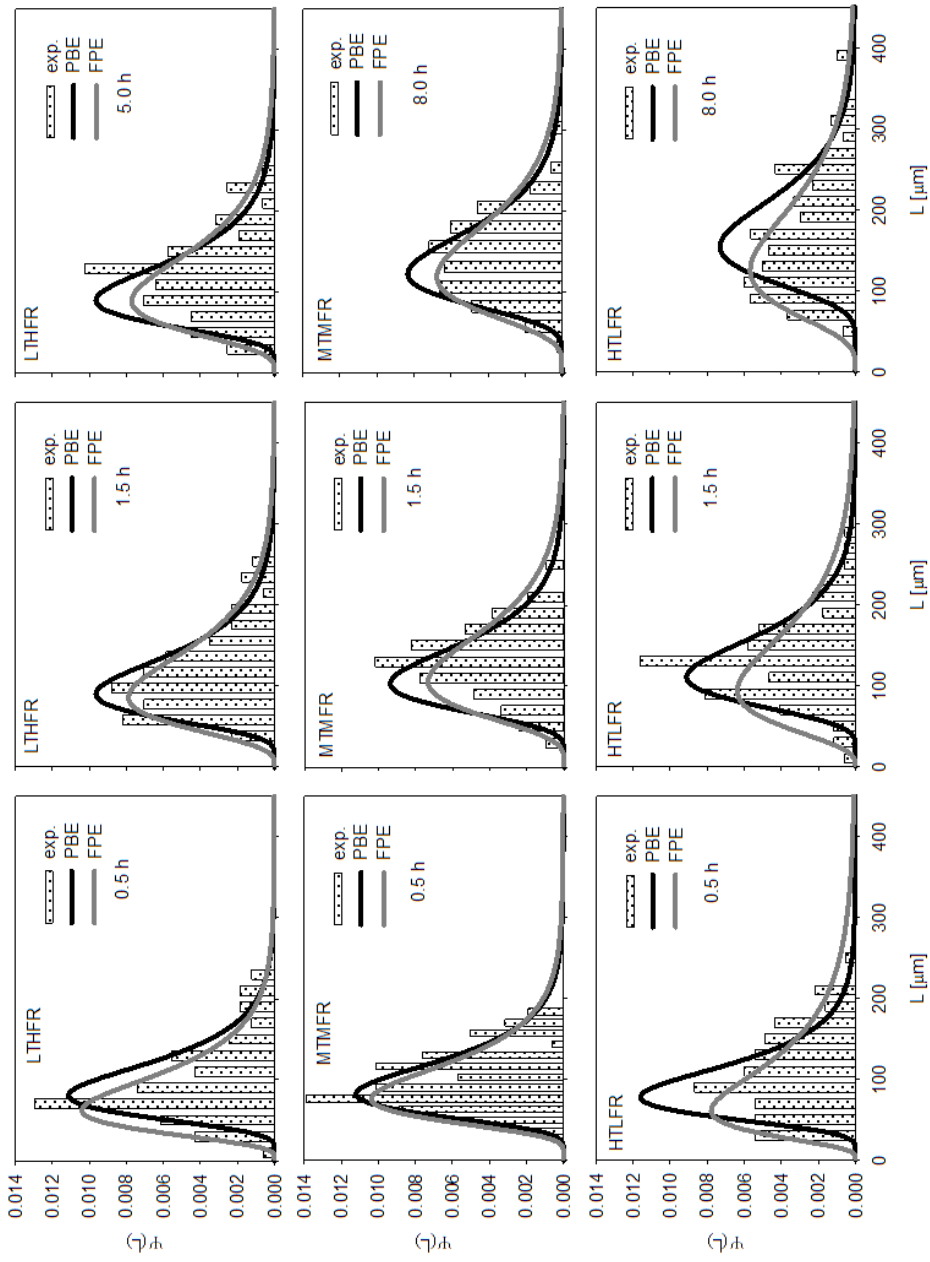

Figure 5.18: Model comparison for experimental runs. The solid grey line represents the FPE, the solid black line represents the PBM and the grey vertical bars represent the experimental distributions in linear scale.

The comparison between experiments and model is also carried out by reporting, in Figure 5.19, the time evolution of the mean crystal size computed, for the PBE using Equation 3.1 and for the FPE using Model 1.
The agreement is rather good for any condition and both the PBE and the FPE models correctly describe the increasing trend of the average crystal growth even if the mean crystal size predicted by the PBE does not reach an asymptotic value, at least in the experimental time window, at the lowest feedrate.

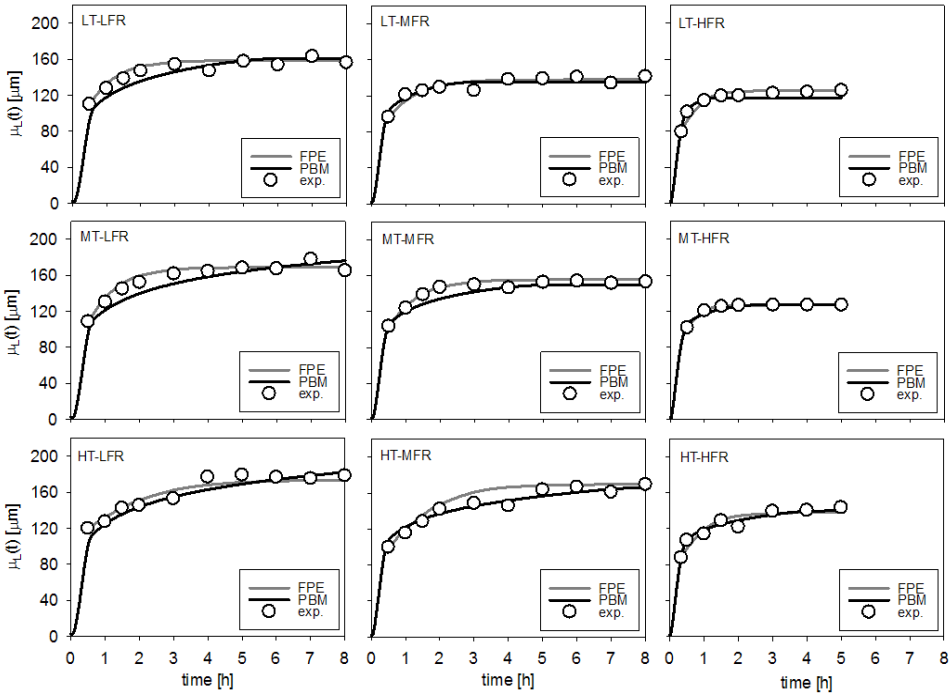

Figure 5.19: Mean crystal size experimentally observed, compared (white dots) with the theoretical predictions obtained with both approaches (solid grey line FPE and solid black line PBM), for the nine runs as a function of time.

In order to validate both models a validation run has been performed. In particular, the change in time of the antisolvent feedrate and temperature has been changed as shown before in Figure 5.16.

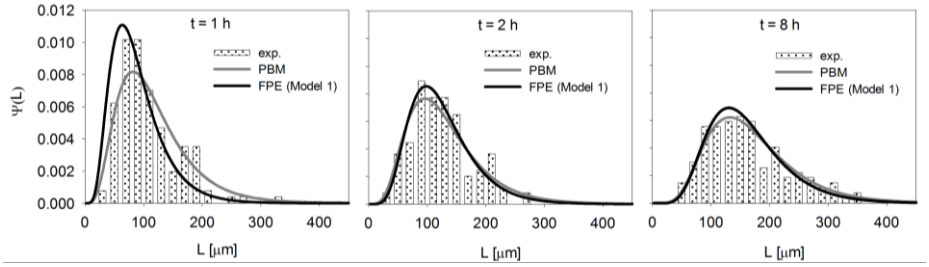

Figure 5.20: Model comparison for the validation run. The black solid line represents the FPE, the dashed black line represents the PBM and the grey vertical bars represent the experimental distributions.

In Figure 5.20, the crystal size distributions for both models for the validation experiment are shown at one, two, and seven hours. Again both models match the experimental data CSD very well.

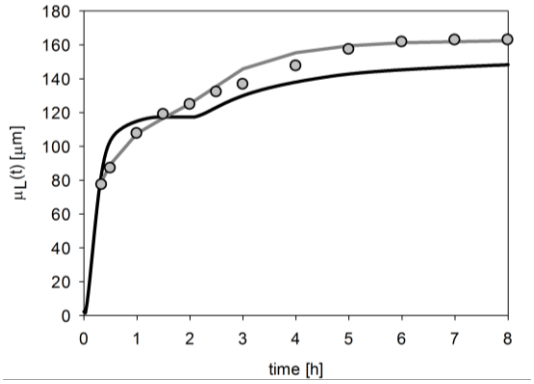

Figure 5.21: Mean size of crystals obtained from the validation operating conditions. The solid grey line represents the time evolution of the mean size, using the FPE, the solid black line represents the time evolution of the mean size, obtained by integration of the PBM using the validation operating conditions and the grey dots represent the experimental points obtained using the validation operating conditions.

5.3.3 Operational Map

The obtained global models can be used to define the operating conditions of the crystallization process, leading to the desired mean and variance of the crystal size distribution. In order to have a

functioning tool for designing the proper crystallization runs, a map can be constructed where asymptotic iso-mean and iso-variance curves are reported in an antisolvent feedrate – temperature plane. In this case, the asymptotic CSD for the map construction can be analytically obtained also for Model 1, using the approach reported in Tronci et al. (2011), which leads to the following expression for the stationary solution of Model 1:

$$\psi(y) = N_S e^{\int g(y;\theta_1)dy} \qquad N_S = \frac{1}{\int_{-\infty}^{+\infty} e^{\int g(y;\theta_1)dy}} \tag{5.14}$$

In particular, the stationary solution for Model 1 is

$$\psi_1(y) = N_{S1} e^{\frac{r_1}{D_1}\left(\frac{y^2}{2} - \frac{y^3}{3K_1}\right)} \quad N_{S1} = \frac{1}{\int_{-\infty}^{+\infty} e^{\frac{r_1}{D_1}\left(\frac{y^2}{2} - \frac{y^3}{3K_1}\right)}} \tag{5.15}$$

The stationary CSD for Model 2 is easily obtained from a Gaussian distribution with mean equal to K_2 and variance equal to K_2D_2/r_2 (c.f., Eqs 3.44, 3.46)

$$\psi_2(y) = \frac{1}{\sqrt{2\pi K_2 D_2 / r_2}} e^{-\frac{1}{2}\frac{(x-K_2)^2}{K_2 D_2 / r_2}} \tag{5.16}$$

For sake of brevity, only the map for Model 2 (linear growth rate) has been reported at different operating conditions. As demonstrated in the previous section, the behavior of the two models are almost overlapping, therefore the results reported in Figure 5.22 are representative of both linear and nonlinear case.

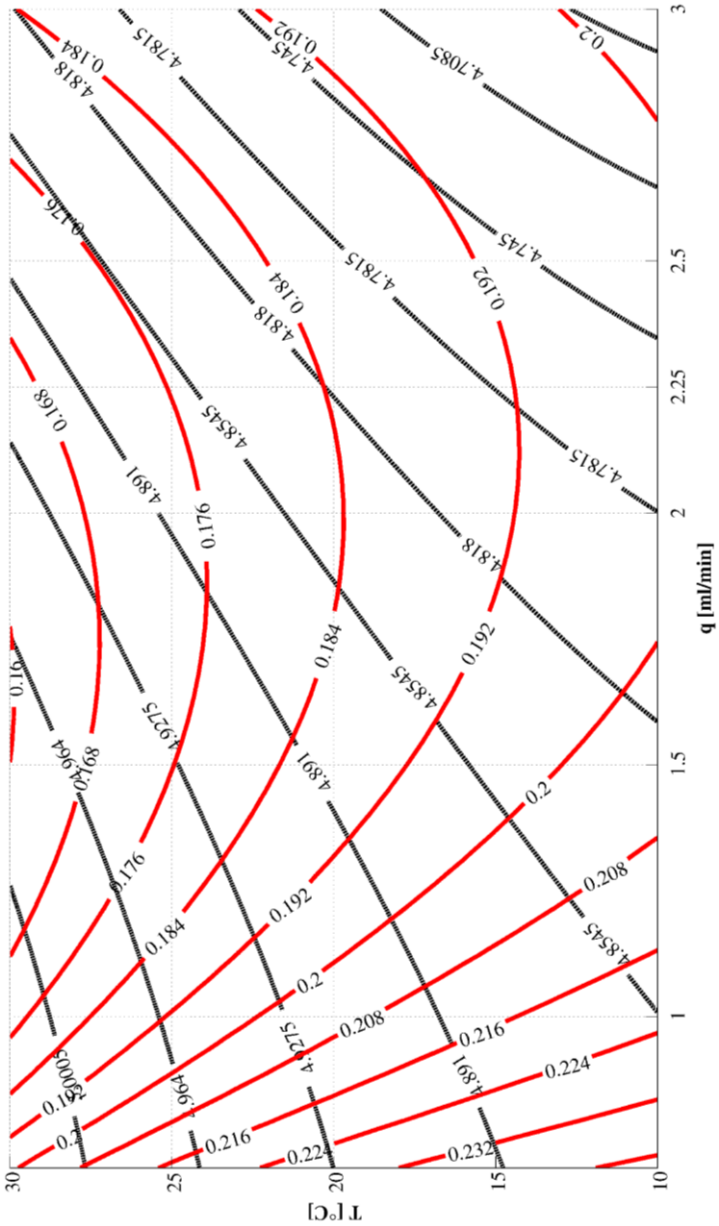

Figure 5.22: Iso-means - iso-variances map, reported in function of T and q, for the model 2 in logarithmic scale.

By inspection of Figure 5.22 it is interesting to note that iso-variance curves may intersect iso-mean curves in two points, therefore the same distribution in terms of the first two moments can be obtained at different operating conditions. Considering Figure 5.22, a CSD with mean crystal size (logarithmic scale) equal to 4.818 and variance equal to 0.184 is attained at (q, T) = (2.25, ~21.0) and (q, T) = (3.0, 30.). This result implies some kind of input multiplicity of the system, which is coherent with the opposite effects that antisolvent feedrate and temperature have on the crystallization process: high asymptotic crystal size can be reached with low q and high T, but the same result can be obtained increasing q and, at the same time, decreasing T. Figure 5.22 has been also represented in linear scale in Figure 5.23, accordingly to the non-linear transformation previously explained [Equations 5.4a and 5.4b].
To corroborate these findings, an additional experiment was conducted at q = 2.25 ml/min and T = 20 ºC (indicated with a circle in Figure 5.23). The multiplicity of the considered crystallization system with respect to inputs can now be verified by considering the time evolution of the experimental mean crystal size at (q, T) = (3.0 ml/min, 30ºC) and (q, T) = (2.25 ml/min, 20ºC) and that predicted by the nonlinear (dotted line) and linear model (solid line), and results are reported in Figure 5.24.

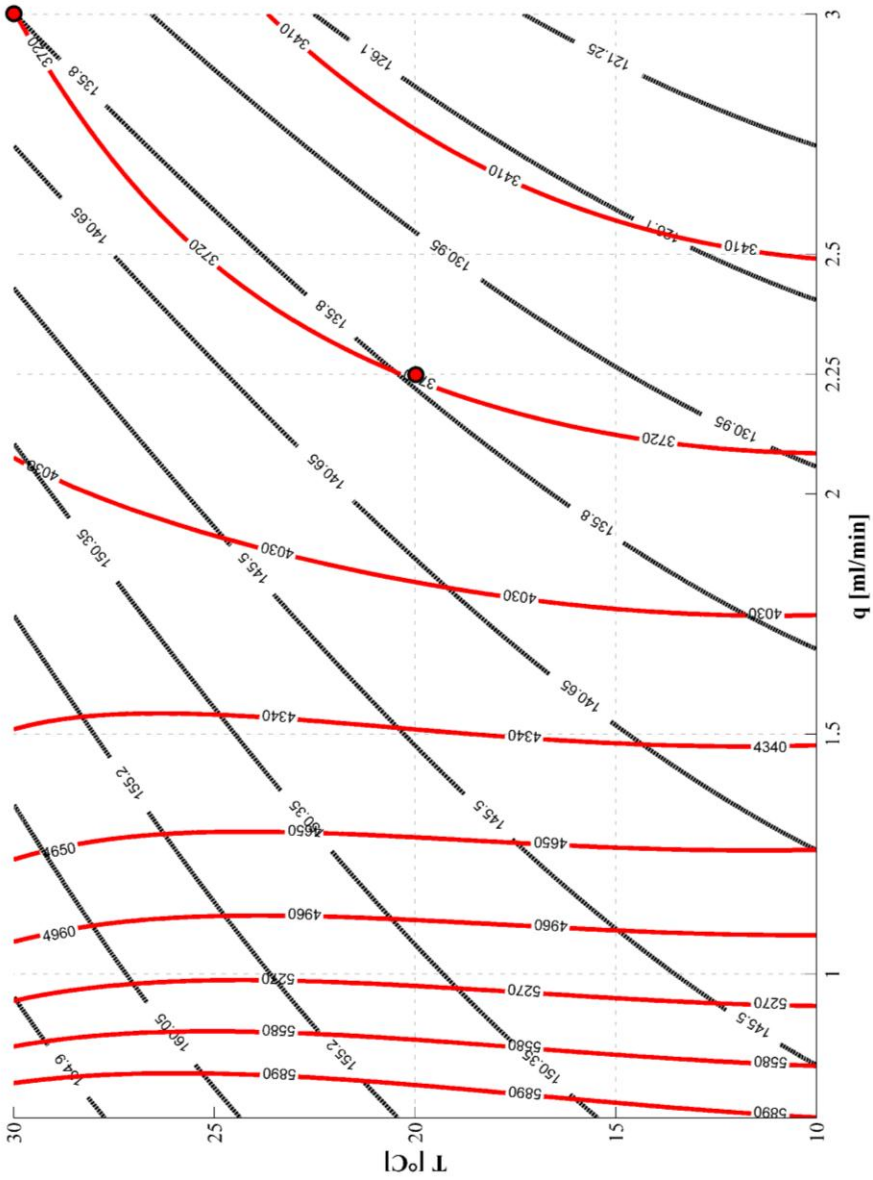

Figure 5.23: Iso-means - iso-variances map using model 2, in which the experimental runs are reported highlighted with circles. The mean sizes are represented with a solid black line and the variances with a dotted black line.

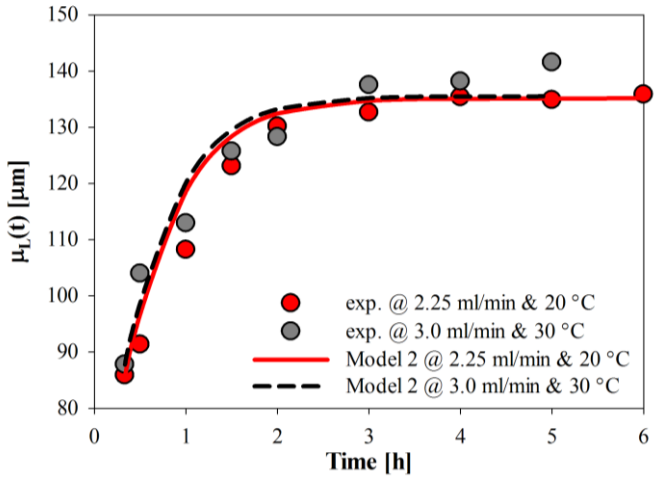

Figure 5.24: Comparison of both, model and the experimental values, in the multiplicity points. Black lines and values are referred to the run at 30 °C and 3.0 ml/min and the grey lines and values are referred to the run at 20 °C and 2.25 ml/min. With solid lines are represent the trajectory obtained using the model 2 and the dotted lines are referred to the model 1. Dots represent the experimental data, all in linear scale.

As can be seen in Figure 5.24, each mean size profile takes a slightly different path to reach the same final value (within the tolerance error associated with the crystal size measurement). At the beginning of the process, higher temperature and antisolvent feedrate speed up the crystallization process (white circles), therefore the mean crystal size is higher with respect to the values obtained at lower *q* and *T*. This behavior is also represented by the models, which have different initial conditions. As time elapses, the values predicted by the two models at different operating conditions converge, as well as the experimental mean crystals size values, as expected considering the iso-mean and iso-variance map.
The input multiplicity can be also verified by looking at the experimental and calculated CSD at different sampling time (Figure 5.25). Again, there is a slight mismatch at the beginning sampling times, but the asymptotic values predicted by the map are confirmed at the end of batch (time = 5-6 h), where there is a significant overlapping between the histograms of the crystal size obtained at

(q, T) = (2.25 ml/min, 20ºC) and at (q, T) = (3.0 ml/min, 30ºC). There is also a perfect match between the two models, evidencing that linear assumption does not worsen the description of the considered system. This fact is important because a linear convective term in the FPE allows solving analytically the Fokker-Planck equation, giving an effective tool for on-line optimization and model-based control of the process.

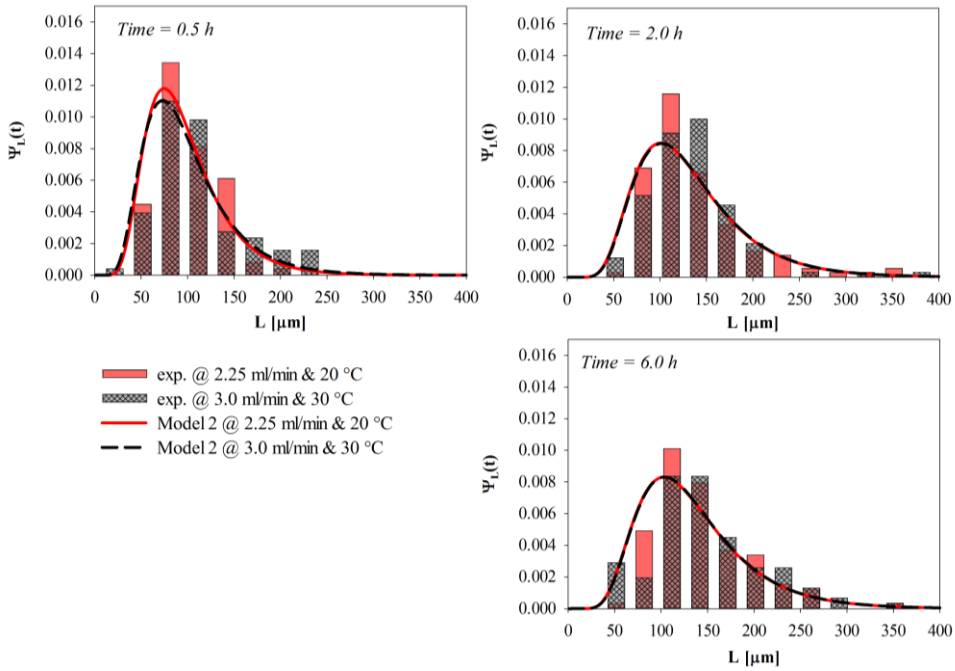

Figure 5.25: CSDs at the multiplicity points. The dark grey lines and bars represent the data at 20 °C and 2.25 ml/min, the light gray lines and bars represent the data at 30 °C and 3.0 ml/min. The solid lines are the model 2 and the dotted lines are the model 1.

5.4 Solvent-Antisolvent Interactions and Hydrogen Bonding

In order to characterize quantitatively the behavior of the systems using different antisolvents with different polarities and/or temperature, the linear FPE with nonlinear coefficients has been used, Equation 3.35.
As hypothesized, it is expected that the hydrogen bonds influence the supersaturation of the solution; in particular, as hydrogen bonds become stronger (using an antisolvent with high PI) the supersaturation becomes higher as well, thus decreasing the solubility and obtaining crystals with a smaller mean size and a narrower CSD.

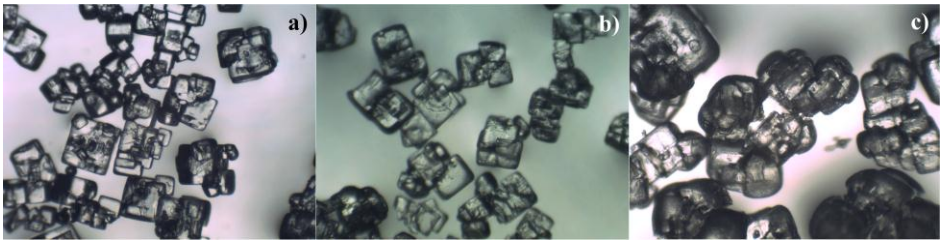

Figure 5.26: Asymptotic images taken at the end of the experimental runs using three different antisolvents: a) acetic acid, b) ethanol and c) iso-propanol.

Considering the first set of experimental runs using different antisolvents with different polarities, where all the runs were conducted at 1.5 ml/min and 20 °C, we can observe from Figure 5.26 the behavior of the crystals at the end of the run after 8 h, considering the same image format and the same magnification factor for the microscope analysis. We can notice, from the right to the left that as the antisolvent PI increases, the crystals, at asymptotic conditions, become smaller as we expected. The higher polarity of the antisolvent used inducted stronger hydrogen bonds and consequently a higher supersaturation, favoring the nucleation of crystals and reducing their asymptotic dimension. To describe quantitatively the influence of the different antisolvents on the

dynamic and the asymptotic behavior of the crystal size distribution (CSD), the parameters of the FPE have been estimated using the Maximum Likelihood method as described in the previous paragraph. The estimated FPE parameters and the PI of the antisolvents used are summarized in Table 5.17.

T = 20 °C and q = 1.5 ml/min			
Antisolvent	*Acetic Acid*	*Ethanol*	*Iso-propanol*
Polarity Index (PI)	4.8	4.3	3.9
r (growth velocity)	1.421	1.403	0.429
K (asymptotic dimension)	4.895	4.930	5.429
D (diffusivity)	0.326	0.216	0.090

Table 5.17: The table above represents the polarity index (PI) for each antisolvent used, related to the FPE parameters for first set of experimental runs.

The FPE parameters on Table 5.17 represent respectively the growth velocity (r), the asymptotic mean size in logarithmic scale (K) and the diffusivity of the FPE (D), proportional to the CSD dispersion. Observing the overall behavior of the parameters, they follow the trend expected according to the polarity index and hypothesized on Table 2.1. The greater the PI, the smaller is the asymptotic mean size of crystals (smaller K), reaching quickly the asymptotic conditions (higher r).

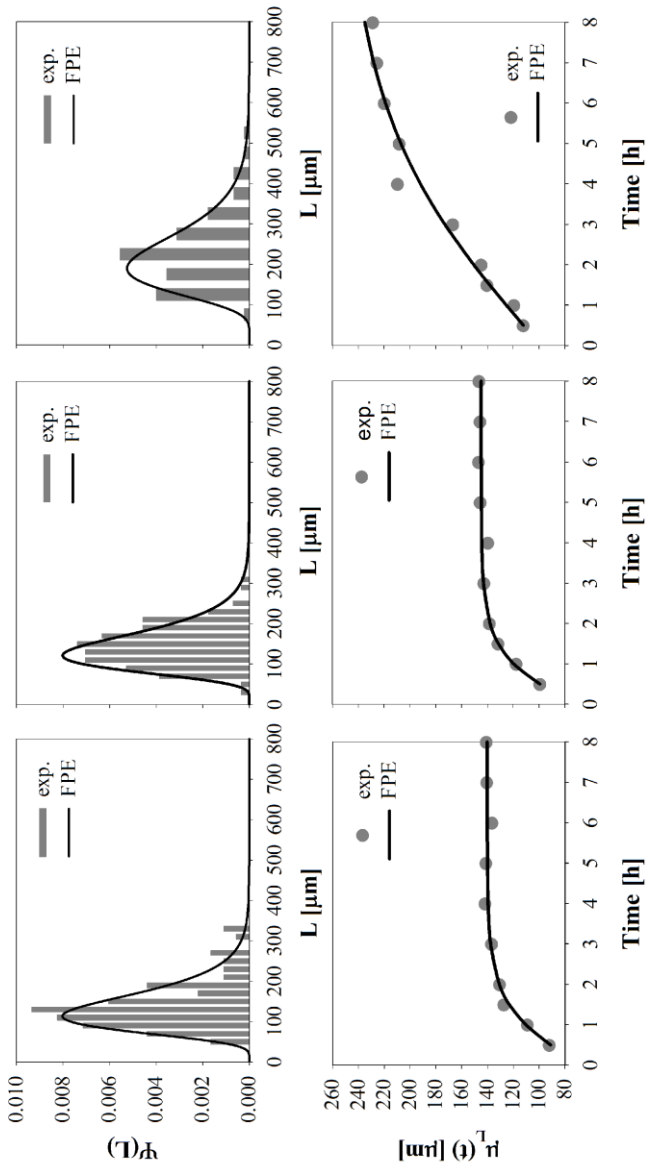

Figure 5.27: Experimental results fitted with the FPE for the runs using a) acetic acid, b) ethanol and c) iso-propanol, in isothermal conditions and keeping constant the antisolvent feed-rate. The results represent both, the asymptotic conditions and the dynamic behavior of the system.

Furthermore, in order to appreciate these effects, we have plotted the CSDs (asymptotic conditions) and the mean size time evolutions obtained using the three different antisolvents with different polarities together with the FPE model predictions, Figure 5.27. We can observe that the mean size of crystals, when an asymptotic behavior is reached, is inversely proportional to the polarity index of the antisolvent used. The same trend can be also observed for the dispersion of the CSDs, becoming wider (considering the asymptotic conditions) as polarity increases (FPE diffusion D). The growth velocity, *r*, has a proportional effect on the dynamic of the system, since the most polar antisolvent speeds up the dynamic of the mean size evolution according with the effects we have expected and reported in Table 2.1.
Considering the temperature effect, a similar behavior was observed during the second set of experimental runs. In this case, ethanol was used as the antisolvent at different temperatures, keeping constant the antisolvent feedrate.

P.I. = 4.3 and q = 1.5 ml/min			
Antisolvent	*Ethanol*		
Temperature	10 °C	20 °C	30 °C
r (growth velocity)	1.934	1.403	1.103
K (asymptotic dimension)	4.858	4.930	5.049
D (diffusivity)	0.373	0.216	0.171

Table 5.18: The table above represents the temperature effects related to the FPE parameters for the three antisolvents considered.

Observing the values of the FPE parameters reported in Table 5.18, we can notice the analogy, in terms of temperature changes, with the data observed in the previous set of parameters obtained using different antisolvents with different polarities. The growth velocity decreases as the temperature increases, the same for the diffusivity, where the opposite trend has been obtained for the asymptotic mean size of crystals.

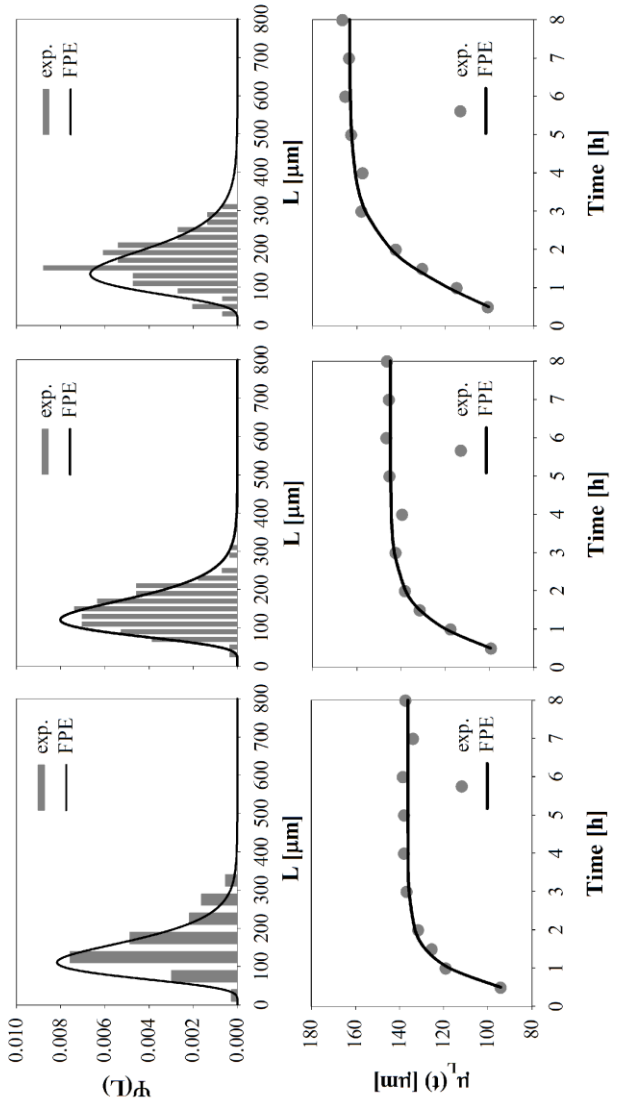

Figure 5.28: Experimental results fitted with the FPE for the runs using ethanol, keeping constant the antisolvent feed-rate and varying the temperature from 10 to 30 °C. The results represent both, the asymptotic conditions and the dynamic behavior of the system.

This behavior can be explained in terms of the hydrogen bond strength, which is a function of the temperature. Indeed, when increasing the temperature we have weaker hydrogen bonds, similar to when using a lower polarity antisolvent, and consequently generating a lower supersaturation rate. The low values of diffusivity at higher temperatures can be explained by the dissolution of crystals and thus generating narrower CSDs. These last results are also reported in terms of CSDs and mean sizes, in order to highlight the asymptotic and the dynamic behavior of the system under temperature changes using a constant antisolvent feedrate with a medium polarity index. This behavior observed is analogous to that observed in Figure 5.27, confirming that as the temperature increases the supersaturation and then the nucleation decreases as well (Figure 2.3), allowing the crystals to grow indefinitely according to the mass of solute introduced on the initial solution. Similar behaviors with the temperature have been obtained for different systems, using polar solvents [Widenski et al, 2012; Galan et al, 2010; Grosso et al, 2010; Grosso et al, 2011; Cogoni et al 2012; Park and Yeo, 2012; Tronci et al, 2011]. Again we can see that both, temperature and polarity play an important role in antisolvent crystallization processes due to the hydrogen bond influence (see Table 2.1). Indeed, in using an antisolvent with a higher polarity index and keeping constant the antisolvent feedrate and temperature, we are favoring, from a statistical point of view, the number of hydrogen bonds in the system. On the other hand, considering only one antisolvent and keeping a constant antisolvent feedrate while adjusting the temperature, we have a similar effect since at lower temperatures we are increasing the strength of hydrogen bonds, thus increasing the number of hydrogen bonds in the solution, and consequently increasing the supersaturation of the solution.

To emphasize the temperature, the feedrate and the polarity effects and their influence on the supersaturation of the system, we have considered a third set of experimental runs composed of two runs in extreme conditions. In first one, using iso-propanol at high temperature (30 °C) and low antisolvent feedrate (0.7 ml/min), we were expecting, according to Table 2.1, the biggest crystals among

all the experimental runs. We have performed the second experiment using acetic acid at low temperature (10 °C) and with a high antisolvent feedrate (3.0 ml/min) to obtain the maximum supersaturation possible within the range of temperature and antisolvent feedrate considered.

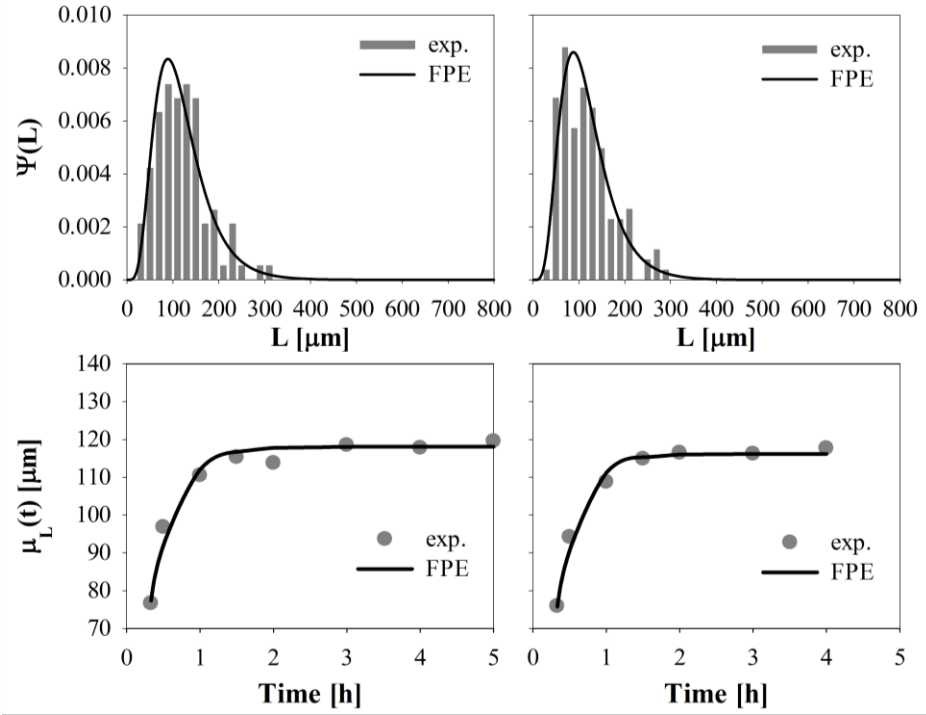

Figure 5.29: Experimental results fitted with the FPE for the runs using ethanol and acetic in the upper extreme condition, when temperature is kept constant to 10 °C and the antisolvent feed-rate at 3.0 ml/min.

The results are shown and compared with the data collected using ethanol at the same operating conditions in Figure 5.29. In the case of the acetic acid (the most polar antisolvent), when compared with the results obtained using ethanol at the same operating conditions, we can see a slight difference in terms of the asymptotic CSDs and mean size of crystals, with a smaller mean size for the acetic acid according to Table 2.1. The same small differences have been obtained for the dispersion and the growth rate of the system. This

fact can be explained by the high supersaturation of the system, which has likely reached a saturation point due to the high hydrogen bond strength and prevalence. This result is characterized by an explosive nucleation of crystals in the early stages of the run, in which the crystals grow slightly, limited by the amount of solute introduced at the beginning of the experimental run, and ultimately obtaining similar CSDs at the end of the run using both antisolvents.

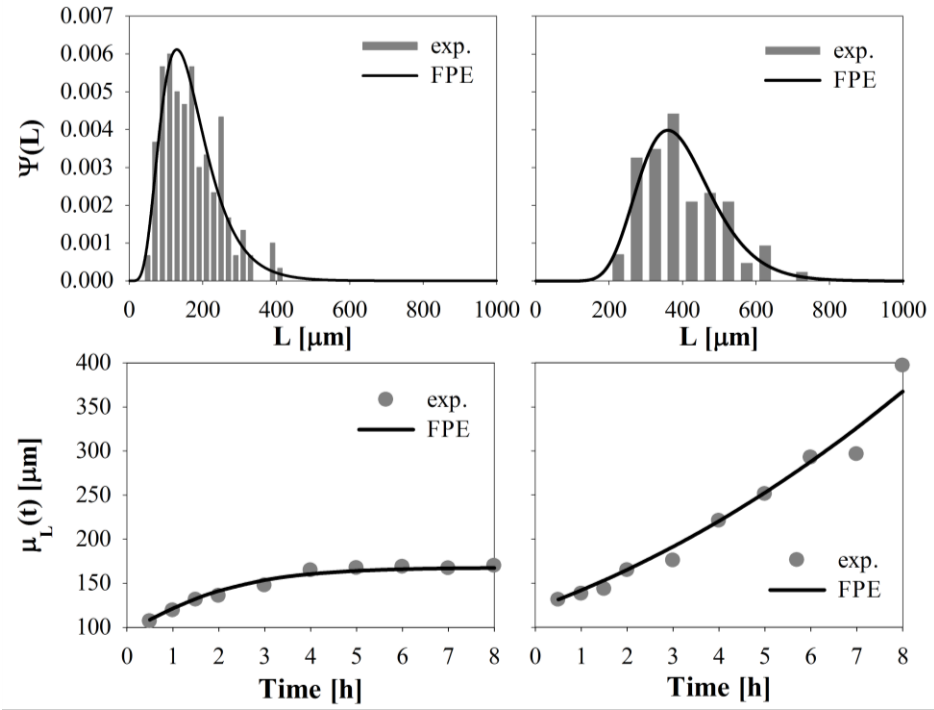

Figure 5.30: Experimental results fitted with the FPE for the runs using ethanol and iso-propanol in lower extreme conditions, when temperature is kept constant to 30 °C and the antisolvent feed-rate at 0.7 ml/min.

In the second experiment, at lower extreme supersaturation conditions (Figure 5.30), we can see that the asymptotic CSDs are extremely different between mean sizes for both antisolvents. This effect is explained by the very small nucleation rate, so that growth rate is dominant, resulting in a limited amount of nuclei in the first stage of the experimental run and allowing the crystals to grow

bigger. Specifically when using iso-propanol as the antisolvent, with its low polarity index, the hydrogen bond effect is really weak, generating a small supersaturation, and inhibiting even more the nucleation of the crystals. Consequently the CSD has not reached an asymptotic behavior, growing indefinitely (limited by the amount of solute mass in the system) after 8 hours of run, using all the antisolvent available for the experiment.

Summarizing, the overall behavior shows that the crystal size increases by increasing the temperature or decreasing the antisolvent feedrate or using an antisolvent with a low polarity index. Temperature and polarity index are correlated to the hydrogen bond strength by physical aspects, thus decreasing the temperature causes the hydrogen bonds to become stronger [Czeslik and Jonas, 1999; Dougherty, 1998]. This in turn increases the supersaturation, enhancing the nucleation rate despite the growth rate, and obtaining at the end smaller crystals. The same effect can be obtained keeping a constant temperature, using an antisolvent with a higher polarity index or using a high antisolvent feedrate since this statistically increases the number of hydrogen bonds in the solution. From a physical point of view, we have first hypothesized and then confirmed there exists a correlation between the hydrogen bond strength and the supersaturation of the solution, thus influencing nucleation and growth rate. Although hydrogen bond is weaker than ion-dipole interactions, it is able to reduce the number of water molecules (or in general solvent/antisolvent molecules) that surround the solute ions, favoring the crystallization of the solute. The hydrogen bond strength is directly proportional to the polarity of the solvent/antisolvent considered and also depends on pressure and temperature [Czeslik and Jonas, 1999].

We have to remark that the results were obtained for a system whose solubility is weakly dependent on temperature. Using different antisolvents with different polarities, we can obtain different results influencing the supersaturation and, as a consequence, obtaining different asymptotic and dynamic behaviors of the CSD.

Chapter 6

Conclusions and future research

6.1 Conclusions

The development of effective mathematical models describing the crystal growth dynamics is a crucial issue towards finding the optimal process performance and to control the crystal size and distribution. The goal of this Thesis was to find an alternative way to describe the crystallization processes, circumventing the more common Population Balances (PBM). The model had to be simpler, considering the mathematical development, but also maintaining a good description of the system, allowing also to optimize and control the Crystal Size Distribution (CSD) even considering a possible online application, avoiding to use excessive computational resources.

In the developed model, the crystal size is considered as a random variable, whose probability density evolution in time is described in terms of a Fokker-Planck Equation (FPE). It is shown and corroborated via experimentation that the best stochastic model is given using a Geometric Brownian Motion (GBM) for the stochastic term, and a logistic model for the deterministic term of the FPE. Excellent quantitative agreement between experiments and the predictions from the FPE model are obtained for a wide range of conditions, allowing to capture quantitatively the long-tailed

asymmetric shape of the experimental Crystal Size Distribution, CSD.

Keeping the same stochastic component (GBM noise intensity), the deterministic growth term is expressed as a Gompertz model, obtaining a Fokker-Planck equation with linear coefficients allowing to an analytical solution. The analytical solution of the model represents an encouraging way to implement a control system, based on the process model. The slight differences obtained in term of skewness compared to the FPE based on the logistic model are negligible, appearing the FPE with linear coefficients a valuable choice when dealing with applications requiring fast calculations, as in the case of on-line control schemes.

The dependencies on the antisolvent feedrate and temperature of the model parameters have been obtained in an explicit way, guaranteeing simplicity of the global model, while preserving the physical consistency of the results. It has been demonstrated that excellent results can be obtained for both models, with nonlinear and linear coefficients. The obtained global model has been then compared with the more common Population Balances (PBM), showing that the FPE modeling is a good challenger for the representation of the CSD in time, using a parsimonious number of parameters and with a phenomenological knowledge of the system, despite the more complex PBM that, nonetheless, can describe the nucleation of crystals and quantify the obtained product with the zero-th order moment. The obtained global model also allowed to generate operational maps, representing asymptotically the iso-mean and the iso-variance curves with respect to antisolvent feedrate and temperature. This representation allows to find multiple asymptotic conditions with the same CSD, in terms of mean and variance, using different input values.

There is no clear explanation, in literature and in previous works, about the influence of the operating conditions on the antisolvent process, in particular when the solute solubility is slight dependent on the temperature. It has been found that exist a direct correlation between hydrogen bond strength and supersaturation. The results obtained are congruent with the hypothesis made, showing that the asymptotic mean size of crystals is inversely proportional to the hydrogen bond strength, while, controversially, the growth velocity

and the dispersion of the CSD are directly proportional. This clearly represents an important goal that can be extended in future in order to optimize the process, including the optimization and the control of the mean size of crystals and/or the CSD dispersion, and also finding the best antisolvent to use for the desired product to obtain, including economic and energetic aspects.
Concluding, the FPE represents a valid alternative for the description of the CSD, asymptotically and dynamically, allowing to a simpler model formulation, requiring a limited number of parameters to estimate.

6.2 Future research

According to the results obtained, a possible future research can be focused on the development of an internal model-based controller. Knowing the exact transfer function of both, mean size of crystals and CSD variance, as a function of the antisolvent feedrate and temperature, it is possible define a control model to achieve the desired CSD characteristics. Moreover, the feasibility of the CSD to achieve can be selected using the asymptotic maps.
Knowing an asymptotic map of all the possible mean sizes and variances achievable, it is also possible to optimize the antisolvent and the energy consumptions, in case a multiple asymptotic condition is present.
The development of an online method of data sampling can be further developed in order to implement a soft-sensor using also an image analysis method along the experimental run, in real time. Furthermore using a model based control, it is possible to implement a feedback control system.
The last research proposal can be focused on a deep and more accurate study of the hydrogen bond interactions in the non-isothermal antisolvent crystallization systems. The choice of the antisolvent can be obtained regarding its properties, such as the reaction with other compounds, the safety usage and the separation methods. In this way the antisolvent crystallization processes can be optimized beyond the operability conditions, considering also the

reuse and manage of the proper antisolvent to use for the specific solute to crystallize.

Appendix A

Nomenclature

Latin

A	Coefficient of the state variable for the Riccati's equation, defined as $A = -r'/K'$.
b	Ratio used to define the geometric series for the discretization length, defined as $b = (L_{max}/L_0)^{1/\zeta}$.
b_0	Pre-exponential nucleation parameter [-].
b_1	Exponential parameter on the nucleation term for the population balance [-].
B	Nucleation rate expressed on the population balance model [# of particles/s/m^4].
c_1	First coefficient of the equilibrium concentration function.
c_2	Second coefficient of the equilibrium concentration function.
c_3	Third coefficient of the equilibrium concentration function.
C	Solution concentration [Kg NaCl/Kg solvents].
C^*	Equilibrium concentration of the solution [Kg NaCl/Kg solvents].
D	Fokker-Planck Equation Diffusivity.
D'	Fokker-Planck Equation Diffusivity for the FPE-OUP.
D''	Fokker-Planck Equation Diffusivity for the independent variable z, used to obtain the analytical solution of the FPE-OUP ($D'' = D'/K'^2$).

Dt	Dimensionless FPE diffusivity.
g_0	Default growth rate [-].
g_1	Reduction in growth rate due to antisolvent [-].
g_2	Exponent of the reduction in growth rate due to antisolvent [-].
g_3	Activation energy for the growth rate [-].
g_4	Exponent of the temperature dependent term of the growth rate [-].
g_5	First supersaturation exponent of the growth rate [-].
g_6	Second supersaturation exponent of the growth rate [-].
G	Growth rate expressed on the population balance model [m/s].
$h(y)$	Deterministic model in logarithmic scale.
k	Projection of the variable z into the Fourier domain.
k_v	Volumetric shape factor of crystals (equal to 1).
K	Asymptotic dimension of crystals in logarithmic scale for the logistic model.
K'	Asymptotic dimension of crystals in logarithmic scale for the logistic model ($K' = lnL_0$).
i	Imaginary unit where $i^2 = -1$ or i=th element.
L	Characteristic length of crystals in microns [μm], for the PBM is in meters.
L_0	Initial characteristic length of crystals in microns [μm] , for the PBM is in meters.
m_S	Mass of the solvent.
n_i	Discretized crystal density of the PBM [# particles/m^4].
$n(L,t)$	Crystal density of the PBM [# particles/m^4].
r	Growth velocity for the logistic model in logarithmic scale.
r'	Growth velocity for the Gompertz model in logarithmic scale ($r' = \alpha lnL_0$).
r''	Growth velocity for the Gompertz model in logarithmic scale for the random variable z ($r'' = r'/K'$).
R	Ideal gas constant.
S	Relative supersaturation [-].

t	Integration time [h].
t_0	Initial integration time [h].
T	Temperature [K].
V	Reaction volume [m^3].
w	Solute free mass percent of ethanol in the solution [Kg antisolvent/Kg solution].
y	logarithm of the characteristic length of crystals, $y = ln(L)$.
y_0	Logarithm of the initial characteristic length of crystals, $y = ln(L)$.
z	Generic random variable.

Greek

α	Flexibility degree of the white noise intensity (used as exponent).
α	Growth velocity for the Gompertz model in linear scale (used as a variable).
γ	PDF skewness.
γ_z	PDF skewness for the generic random variable z.
γ_L	PDF skewness for the characteristic length of crystals L.
Γ	Noise intensity for the Riccati's equation $\Gamma^2 = 2D'$.
δ_i	Length of each discretization interval used for the PBM, given by $\delta_i = L_i - L_{i-1}$.
$\delta(L-L_0)$	Initial condition for a purely random variable.
$\eta(t)$	White noise.
θ	Vector of the FPE parameters.
μ_z	Mean size of the generic random variable z.
μ_{y0}	Initial mean size of crystals in logarithmic scale ($t = t_0$).
μ_{z0}	Initial mean size of crystals in logarithmic scale for the variable z ($t = t_0$), defined as $\mu_{z0} = \mu_{y0}/K'$.
$\mu_0(t)$	Zero order moment for the PBM [# particles/m^3].
$\mu_y(t)$	Dynamic mean size of crystals in logarithmic scale for the FPE-GM.

ρ_C	Crystal density of sodium chloride [Kg/m^3].
ρ_S	Solution density [Kg/m^3].
σ_{z0}	Initial standard deviation of crystals in logarithmic scale for the variable z ($t = t_0$), defined as $\sigma_{z0} = \sigma_{y0}/K'$.
σ^2_{y0}	Initial variance of crystals in logarithmic scale ($t = t_0$).
σ^2_{z0}	Initial variance of crystals in logarithmic scale for the variable z ($t = t_0$), defined as $\sigma^2_{z0} = \sigma^2_{y0}/K'^2$.
$\sigma_y(t)$	Dynamic standard deviation of crystals in logarithmic scale for the FPE-GM.
$\sigma^2_y(t)$	Dynamic variance of crystals in logarithmic scale for the FPE-GM.
Ψ	Dependent variable of the FPE.
$\Psi(0)$	Initial PSD for a purely random process.
$\Psi_z(z)$	Dependent variable of the FPE along the generic random variable z.
$\Psi(L,t)$	Dependent variable of the FPE as a function of L and t.
$\Psi(y,t)$	Dependent variable of the FPE as a function of y and t.
$\Psi(0,t)$	Lower extreme of the FPE in linear scale.
$\Psi(-\infty,t)$	Lower extreme of the FPE in logarithmic scale.
$\Psi(+\infty,t)$	Upper extreme of the FPE in linear and logarithmic scale.
$\tilde{\Psi}(k,t)$	Dependent variable of the FPE represented on the Fourier domain.
$\tilde{\Psi}(k,t_0)$	Initial condition for the dependent variable of the FPE represented on the Fourier domain.
Ω	Domain for the generic random variable z.

Other

ΔC	Absolute supersaturation [Kg NaCl/Kg solvents].
ΔL	Increment of size of crystals used for the PBM [m].

Subindices

0	Initial conditions.
C	Crystal (for crystal density).
L	Linear scale.
max	Used to define the maximum crystal size used in the discretization for the PBM.
S	Solution density.
v	Volumetric.
y	Logarithmic scale.
ζ	Number of the discretization intervals used for the PBM.
z	Random variable or transformed variable for the OUP.

Accents

~	Fourier domain PDF.
*	Equilibrium concentration.

Acronyms

AIC	Akaike Index Criterion.
CSD	Crystal Size Distribution.
FPE	Fokker-Planck Equation.
GBM	Geometric Brownian Motion.
GZ-ML	Gompertz Model – Maximum Likelihood.
HFR	High Feed Rate.
HT	High Temperature
LBM	Linear Brownian Motion.
LE	Langevin Equation.
LFR	Low Feed Rate.
LG-LS	Logistic Model – Least Square,
LG-ML	Logistic Model – Maximum Likelihood.
LT	Low Temperature-
MAD	Mean Absolute Deviation.
MFR	Medium Feed Rate.

MOC	Method Of Characteristics.
MT	Medium Temperature.
ODE	Ordinary Differential Equation.
OUP	Ornstein Uhlenbeck Process.
PBM	Population Balance Model.
PDF	Probabilistic Density Function.
PI	Polarity Index.

Components

AcOH	Acetic Acid or Ethanoic Acid (C2H4O2).
Cl^-	Chlorine ion.
EtOH	Ethanol or Ethyl Alcohol (C2H6O).
H_2O	Water.
Na^+	Sodium ion.
NaCl	Sodium Chloride.
IsopOH	Isopropanol or 2-Propanol (C3H8O).

Structures

$E[\eta(t)]$	Mean value of the white noise.
$E[\eta(t)\,\eta(t')]$	Autocorrelation of the white noise.
$f(L,t;\theta)$	Deterministic model as a function of the independent variable L, the time variable t and the vector of parameters θ.
$g(L)$	Noise intensity of the Langevin equation.
$g(L)\delta(t-t')$	Value of the autocorrelation of the white noise.
$h(y,t;\theta)$	Deterministic model as a function of the independent variable y, the time variable t and the vector of parameters θ.
$n(L_i,t=0)$	Initial condition for the discretized PBM, equal to zero.
$n(L_1,t)$	Lower boundary condition for the discretized PBM, equal to zero.
$n(L_\zeta,t)$	Upper boundary condition for the discretized PBM, equal to zero.

$n(L,t)\Delta L$	Number of particles in a unit of volume having size between L and $L+\Delta L$.
$N(\mu_y(t),\sigma^2_y(t))$	Dynamic normal distribution in logarithmic scale.
$N(\mu_{y0},\sigma^2_{y0})$	Normal distribution used as initial condition for the FPE in logarithmic scale.
$\tilde{\Psi}(k(s),t(s))$	Dependent variable of the FPE in the Fourier domain, projected onto the s variable in order to apply the MOC.

Bibliography

Abbas, A. and J. A. Romagnoli (2006). DCS implementation of optimal operational policies: a crystallisation case study, *Int. J. of Comp. Appl. in Tech.*, **25** (4), 198-208.

Abbas, A. and J. A. Romagnoli (2007). Multiscale modeling, simulation and validation of batch cooling crystallization, *Original Research Article Separation and Purification Technology*, **53** (2), 153-163.

Abu Bakar, M. R., Z. K. Nagy, A. N. Saleemi and C. D. Rielly (2009), The impact of direct nucleation control on crystal size distribution in pharmaceutical crystallization processes, *Crystal Growth & Design*, **9**, 1378-1384.

Cogoni G., M. Grosso, R. Baratti and J. A. Romagnoli (2012), Time evolution of the PSD in crystallization operations: An analytical solution based on Ornstein-Uhlenbeck process, *AIChE Journal*, doi:10.1002/aic.13760.

Cogoni G., M. Grosso, R. Baratti and J. A. Romagnoli (2011), Dynamic evolution of PSD modeled using an Ornstein-Uhlenbeck Process approach, *18th IFAC World Congress, Milan*.

Crowley T. J., E. S. Meadows, E. Kostoulas and J. Doyle III (2000), Control of particle size distribution described by a population

balance model of semibatch emulsion polymerization, *Journal of Process Control*, **10** (5), 419-432.

Czeslik, C. and J. Jonas (1999), Pressure and Temperature Dependence of Hydrogen-Bond Strength in Methanol Clusters, *Chemical Physics Letters*, **302**, 633-638.

Di Martino P., R. Censi, L. Malaj, D Capsoni, V. Massarotti and S. Martelli (2007), Influence of Solvent and Crystallization Method on the Crystal Habit of Metronidazole, *Cryst. Res. Technol.*, **42** (8), 800-806.

Dougherty R. C. (1998), Temperature and pressure dependence of hydrogen bond strength: A perturbation molecular orbital approach, *Journal of chemical physics*, **109** (17), 7372-7378.

Fa, K. S. (2005), Exact solution of the Fokker-Planck equation for a broad class of diffusion coefficients, *Phys. Rev. E.*, **E 72**, 020101(R).

Feldman, S. R. (2005), *Sodium Chloride*. Kirk-Othmer Encyclopedia of Chemical Technology.

Fujiwara, M., P. S. Chow, D. L. Ma and R. D. Braatz (2002). Paracetamol Crystallization Using Laser Backscattering and ATR-FTIR Spectroscopy: Metastability, Agglomeration, *Crystal Growth and Design*, **2** (5) 363-370.

Galán, O., M. Grosso, R. Baratti and J. A. Romagnoli (2010), Stochastic approach for the calculation of antisolvent addition policies in crystallization operations: An application to a bench-scale semi-batch crystallizer, *Chem. Eng. Sci.*, **65**, 1797-1810.

Galleguillos, H. R., M. R. Taboada and T. A. Graber (2003), A. Compositions, Densities, and Refractive Indices of Potassium Chloride + Ethanol + Water and Sodium Chloride + Ethanol + Water Solutions at (298.15 and 313.15) K, *J. Chem. Eng. Data*, **48**, 405-410.

Grosso M., G. Cogoni, R. Baratti, J. A. Romagnoli (2011), Stochastic Approach for the Prediction of PSD in Crystallization Processes: Formulation and Comparative Assessment of Different Stochastic Models, *Ind. & Eng. Chem. Res.*, **50**, 2133-2143.

Grosso, M., O. Galán, R. Baratti and J. A. Romagnoli (2010), A stochastic formulation for the description of the crystal size distribution in antisolvent crystallization processes, *AIChE J.*, **56** (8), 2077-2087.

Jagadesh, D., N. Kubota, M. Yokota, N. Doki and A. Sato (1999), Seeding effect on batch crystallization of potassium sulfate under natural cooling mode and a simple design method of crystallizer, *J. Chem. Eng. Jpn.*, **32**, 514–520.

Jones, A. G. (2002), *Crystallization Process Systems*, London UK: Butterworth Hinemann.

Kee, N. C. S., R. B. H. Tan and R. D. Braatz (2009), Selective crystallization of the metastable α-form of L-glutamic acid using concentration feedback control, *Crystal Growth & Design*, **9**, 3044-3051.

Lindenberg, C., M. Krattli, J. Cornel, M. Mazzotti and J. Brozio (2009), Design and Optimization of a Combined

Cooling/Antisolvent Process, *Crystal Growth & Design*, **9**, 1124-1136.

Lopes, A. and F. Farelo (2006), Growth kinetics of potassium chloride II—Water–ethanol systems, *Journal of Crystal Growth*, **290**, 220-224.

Mastai Y. (2012), *Advances in Crystallization Processes*, INTECH, ISBN 9789535105817.

Miers H. A., and F. Isaac (1907), The Spontaneous Crystallization of Binary Mixtures, *Proceedings of Royal Society*, **A79**, 322-351.

Mirmeharabi, M. and R. Sohrab (2005), An Approach to Solvent Screening for Crystallization of Polymorphic Pharmaceuticals and Fine Chemicals, *Journal of Pharmaceutical Sciences*, **94** (7), 1560-1576.

Mullin J.W. (2001), *Crystallization*, 4th ed., Butterworth-Heinemann: Wouburn, MA.

Nagy, Z. K. (2009), Model based robust control approach for batch crystallization product design, *Computers and Chemical Engineering*, **33**, 1685-1691.

Nagy, Z. K., M. Fujiwara and R. D. Braatz (2008). Modelling and control of combined cooling and antisolvent crystallization processes, *J. Process Control*, **18**, 856–864.

Nowee, M., A. Abbas and J. A. Romagnoli (2007), Optimization in seeded cooling crystallization: A parameter estimation and

dynamic optimization study, *Chemical Engineering and Processing*, **46** (11), 1096–1106.

Nowee, S. M., A. Abbas and J. A. Romagnoli (2008), Antisolvent crystallization: Model identification, experimental validation and dynamic simulation, *Chemical Engineering Science*, **63**, 5457-5467.

Nowee, S. M., A. Abbas and J. A. Romagnoli (2008), Model-based Optimal Strategies for Controlling Particle Size in Anti-solvent Crystallization Operations, *Crystal Growth & Design*, **8**, 2698-2706.

Oosterhof, H., G-J Witkamp and G. M. Van Rosmalen (2001), Antisolvent Crystallization of Anhydrous Sodium Carbonate at Atmospherical Conditions, *AiChE Journal*, **47** (3), 602-608.

Ostwald W. (1887), Studien über de Bildung und Umwandlung Fester Körper, *Zietschrift für Physikalishe Chemie*, **22**, 289-330.

Park M.-W. and S. Yeo (2012), Antisolvent crystallization of carbamazepine from organic solutions, *Chem. Eng. Res. and Design*, http://dx.doi.org/10.1016/j.cherd.2012.05.001.

Ramkrishna D. (2000), *Population Balances. Theory and Applications to Particulate Systems in Engineering*, San Diego: Academic Press.

Randolph A. and M. Larson (1988), *Theory of Particulate Processes*, 2nd ed., Academic Press: San Diego, CA.

Silverman B. W. (1986), *Density Estimation for Statistics and Data Analysis*, London: Chapman & Hall.

Tadayon, A., S. Rohani and M. K. Bennett (2002), Estimation of Nucleation and Growth Kinetics of Ammonium Sulfate from Transients of a Cooling Batch Seeded Crystallizer, *Ind. Eng. Chem. Res.*, **41**, 6181-6193.

Thompson R. W., and J. D. Stevens (1977), A population balance approach to modeling of continuous emulsion polymerization, *Chemical Engineering Science*, **32** (3), 311-322.

Trifkovic, M., M. Sheikhzadeh and S. Rohani (2008), Kinetics Estimation and Single and Multi-Objective Optimization of Seeded, Antisolvent, Isothermal Batch Crystallizer, *Industrial & Engineering Chemistry Research*, **47**, 1586-1595.

Tsoularis, A. and J. Wallace (2002), Analysis of logistic growth models, *Math. Bioscience*, **179**, 21-55.

Widenski, D. J., A. Abbas and J. A. Romagnoli (2012), A modeling approach for the nonisothermal antisolvent crystallization of a solute with weak temperature dependent solubility, *Crystal Research Technology*, **47** (5), 491-504.

Woo, X. Y., Z. K. Nagy, R. B. H. Tan and R. D. Braatz (2009), Adaptive concentration control of cooling and antisolvent crystallization with laser backscattering measurement, *Crystal Growth & Design*, **9**, 182-191.

Worlitschek, J. and M. Mazzotti (2004), Model-based optimization of particle size distribution in batch-cooling crystallization of paracetamol, *Crystal Growth and Design*, **4** (5), 891-903.

Zhou, G. Z., M. Fujiwara, X. Y. Woo, E. Rusli, H. H. Tung, C. Starbuck, O. Davidson, Z. Ge and R. D. Braatz (2006), Direct Design of Pharmaceutical Antisolvent Crystallization Through Concentration Control, *Crystal Growth & Design*, **6**, 892-898.

Acknowledgements

First of all, I would like to thank my tutor, Prof. Roberto Baratti, for the possibility of undertaking this PhD, and for his support and advice during these three years at the Department of Mechanical, Chemical Engineering and Materials (DIMCM).

I would also like to thank my American tutor, Prof. José A. Romagnoli, for his help during my stay in Baton Rouge (LA) in United States, at the Cain Department of Chemical Engineering, and for his support.

I wish to thank Prof. Massimiliano Grosso and Prof. Stefania Tronci of DIMCM, for their support and advices for my research.

Last, I am greatful to my family, who has always believed in me, and this has permitted me to be what I am, and therefore to reach this important goal.